Validacija modela turbulencije pri tranziciji iz laminarnog u turbulentno strujanje

Kovačić, Luka

Master's thesis / Diplomski rad

2020

UNIVERSITY OF ZAGREB

FACULTY OF MECHANICAL ENGINEERING AND NAVAL ARCHITECTURE

MASTER'S THESIS

Luka Kovačić

Zagreb, 2020

UNIVERSITY OF ZAGREB

FACULTY OF MECHANICAL ENGINEERING AND NAVAL ARCHITECTURE

MASTER'S THESIS

VALIDATION OF LAMINAR-TO-TURBULENT TRANSITIONAL FLOW TURBULENCE MODELS

Supervisor:	Student:
Prof. dr. sc Hrvoje Jasak	Luka Kovačić

Zagreb, 2020

I would like to express my sincere gratitude to my supervisor Prof. Hrvoje Jasak for his excellent guidance, patience and generous sharing of his vast knowledge and expertise.

I would also like to thank colleagues from the 8th floor, especially Luka Balatinec, for their advices and always present help.

Finally, I would like to thank my family, friends and my girlfriend for the support and understanding they provided during the entirety of my studies and making of this thesis.

I hereby declare that this thesis is entirely the result of my own work except where otherwise indicated. I have fully cited all used sources and I have only used the ones given in the list of references.

SVEUČILIŠTE U ZAGREBU
FAKULTET STROJARSTVA I BRODOGRADNJE
Središnje povjerenstvo za završne i diplomske ispite
Povjerenstvo za diplomske ispite studija strojarstva za smjerove:
procesno-energetski, konstrukcijski, brodostrojarski i inženjersko modeliranje i računalne simulacije

Sveučilište u Zagrebu Fakultet strojarstva i brodogradnje	
Datum	Prilog
Klasa:	
Ur. broj:	

DIPLOMSKI ZADATAK

Student: **Luka Kovačić** Mat. br.: 0035200010

Naslov rada na hrvatskom jeziku: **Validacija modela turbulencije pri tranziciji iz laminarnog u turbulentno strujanje**

Naslov rada na engleskom jeziku: **Validation of Laminar-to-Turbulent Transitional Flow Turbulence Models**

Opis zadatka:

Transition from laminar to turbulent flow presents a complex problem for engineering turbulence models. A notable example of its importance is a wind turbine airfoil, where turbulence transition plays a critical role in performance. Recently, new eddy viscosity turbulence models claiming capability to predict transition have been developed, most notable the Langtry-Menter 4-equation model and the Walters-Cokljat 3-equation model. Both remain poorly understood in terms of acuracy, mesh resolution requirements, sensitivity to far field conditions and discretisation errors.
The objective of this study is to rigorously validate the performance of a transitional turbulence model with uncertainty assessment, in comparison with benchmark data.
The candidate shall perform the following tasks within this project:

- Perform a literature survey of eddy viscosity turbulence models and describe in detail a selected model, including the equation set and boundary conditions;
- Perform a numerical simulation assuming a steady fully turbulent incompressible flow using the k-omega SST model by Menter for 3 geometries: a 2-D flat plate (2 levels of inlet turbulence intensity), a 2-D EPPLER airfoil at two angles of attack and a 3-D 6:1 prolate spheroid;
- Perform a numerical simulation assuming steady transitional incompressible flow using a transitional turbulence model of choice for 3 geometries: a 2-D flat plate (2 levels of inlet turbulence intensity), a 2-D EPPLER airfoil at two angles of attack and a 3-D 6:1 prolate spheroid;
- Perform a parametric study of simulation results on a number of systematically refined meshes and evaluate mesh uncertainty using the procedure by Eca and Hoekstra;
- Present a comparison of numerical results of fully turbulent and transitional flow simulation against available experimental data or reference results obtained by simulation;
- Report on experiences with the required mesh size, model convergence and difficulties in simulations.

The Thesis shall list the bibliography and any assistance received during this study.

Zadatak zadan:	Datum predaje rada:	Predviđeni datum obrane:
16. siječnja 2020.	19. ožujka 2020.	23. – 27.3.2020.

Zadatak zadao:
Prof. dr. sc. Hrvoje Jasak

Predsjednica Povjerenstva:
Prof. dr. sc. Tanja Jurčević Lulić

Contents

List of Figures

List of Tables

Nomenclature

Abbreviations

AR	Cell aspect ratio
CFD	Computational Fluid Dynamics
DNS	Direct Numerical Simulations
CV	Control Volume
FVM	Finite Volume Method
LES	Large Eddy Simulations
RTT	Reynolds Transport Theorem

Greek Characters

α	[°]	Angle of attack
α_1	[-]	k-ω SST constant
α_2	[-]	k-ω SST constant
β	[-]	k-ω SST constant
$\beta*$	[-]	k-ω SST constant
δ	[m]	Boundary layer thickness
Δ_ϕ	[-]	Data range parameter
ε_ϕ	[-]	Error estimate
γ	[-]	Diffusivity; Intermittency
γ_{eff}	[-]	Effective intermittency
γ_{sep}	[-]	Separation intermittency
λ_θ	[-]	Pressure gradient parameter
μ	[Pa · s]	Dynamic viscosity
μ_{t}	[Pa · s]	Turbulent dynamic viscosity
ν	[m^2 / s]	Kinematic viscosity

ν_t	[m^2 / s]	Turbulent kinematic viscosity
$\boldsymbol{\Omega}$	[s^{-1}]	Vorticity tensor
ω	[s^{-1}]	Specific turbulent dissipation rate
ϕ	[s]	General property
ρ	[kg / m^3]	Density
σ_f	[-]	γ-Re_θ constant
σ_ω	[-]	k-ω SST constant
σ_k	[-]	k-ω SST constant
$\sigma_{\theta\mathrm{t}}$	[-]	*gamma*-Re_θ constant
$\boldsymbol{\tau}$	[N / m^2]	Viscous stress tensor
τ_w	[N / m^2]	Wall Shear Stress
θ	[m]	Boundary layer momentum thickness
$\boldsymbol{\varsigma}$	[N / m^2]	Cauchy stress tensor

Latin Characters

$\mathbf{A}$	[-]	Square matrix
$\mathbf{a}$	[-]	General vector property
a_1	[-]	k-ω SST constant
A_airfoil	[m^2]	Chord length
c	[m]	Chord length
c_a	[-]	γ-Re_θ constant
c_e	[-]	γ-Re_θ constant
C_f	[-]	Skin friction coefficient
C_D	[-]	Drag coefficient
C_L	[-]	Lift coefficient
C_p	[-]	Pressure coefficient
$c_{\theta\mathrm{t}}$	[-]	γ-Re_θ constant
C_{Df}	[-]	Friction drag coefficient

C_{Dp}	[-]	Pressure drag coefficient
$CD_{k\omega}$	[-]	k-ω SST function
$\mathbf{d}_\mathrm{f}$	[-]	Delta vector
$\mathbf{f}$	[N / m^2]	Body force tensor
F	[-]	Blending function
F_length	[-]	Function of the γ-Re_θ model
F_L	[N]	Lift force
F_{DL}	[N]	Friction drag force
F_{Dp}	[N]	Pressure drag force
$\mathbf{I}$	[-]	Identity tensor
k	[J / kg]	Turbulent kinetic energy
L	[m]	Length
$\mathbf{n}$	[-]	Surface normal vector
N_cells	[-]	Number of cells
N_foil	[-]	Number of faces on the airfoil
N_plate	[-]	Number of faces on the plate
$\widetilde{P_k}$	[kg / (m s^3)]	Turbulent kinetic energy production limiter
E_γ	[-]	Intermittency destruction
F_onset	[-]	Function of the γ-Re_θ model
p	[Pa]	Pressure
P_γ	[-]	Intermittency production
P_k	[kg / (m s^3)]	Turbulent kinetic energy production
$P_{\theta\mathrm{t}}$	[-]	Momentum thickness Reynolds number production
$\mathbf{q}_s$	[-]	Surface source
q_v	[-]	Volume source
$\widetilde{Re_{\theta\mathrm{t}}}$	[-]	Local transition onset momentum thickness Reynolds number
r	[-]	Grid refinement ratio

Re_{v}	[-]	Strain-rate Reynolds number
Re_{θ}	[-]	Momentum thickness Reynolds number
$Re_{\theta\mathrm{c}}$	[-]	Critical momentum thickness Reynolds number
$Re_{\theta\mathrm{t}}^{\mathrm{eq}}$	[-]	Equilibrium value of the Momentum thickness Reynolds number
Re	[-]	Reynolds number
$\mathbf{S}$	[s^{-1}]	Strain-rate tensor
S	[m^2]	Surface area
S_{m}	[m^2]	Surface area of V_m
t	[s]	Time
Tu	[%]	Turbulence intensity
$\mathbf{u}$	[m / s]	Velocity vector
U	[m / s]	Mean velocity
u^+	[-]	Dimensionless velocity
U_{ϕ}	[-]	Numerical uncertainty
u_{τ}	[m / s]	Friction velocity
V	[m^3]	Volume
V_{m}	[m^3]	Material volume
V_P	[m^3]	Volume of the cell
y	[m]	Wall distance
y^+	[-]	Dimensionless wall distance

Superscript

$'$	Fluctuation around the mean value
$-$	Mean value
T	Transpose

Subscript

b	Value at the boundary
f	Value at the cell face

$_\infty$	Free-stream value
$_N$	Value at the neighbouring cell

Abstract

Urgent generation of turbulence models for Computational Fluid Dynamics (CFD) enabled accurate simulation of fully turbulent flows in industry for decades, however, prediction accuracy for laminar-to-turbulent transitional flow lags significantly. Transitional turbulence models are still either in development or validation phase and not sufficiently mature for regular use in industrial computational fluid dynamics (CFD). In this Thesis validation of the Langtry-Menter k - ω SST [8], a transitional 4 equation turbulence model is presented. The Langtry-Menter k - ω SST, also known as the γ - Re_θ model, is a 4 equation correlation-based transition model built strictly on local variables. Transitional turbulence model γ - Re_θ is compared with the well known k - ω SST model by Menter [9]. The k - ω SST is a 2 equation eddy-viscosity model. 2D validation is carried out for a Flat Plate geometry and the Eppler 387 airfoil geometry. Systematic mesh refinement study is performed for every geometry, with 9 meshes of different resolution. Flow quantities selected for comparison with experimental data include mean horizontal velocity profile, at three locations and skin friction coefficient for the Flat Plate geometry and pressure coefficient for Eppler 387 airfoil geometry. Furthermore, numerical uncertainty of the results, with regard to mesh density, is evaluated in accordance with Eca and Hoekstra [10]. Simulation results for most of the 2D test cases show accurate transition behaviour and high correspondence with the experimental data.

Keywords: *CFD*, *OpenFOAM*, *foam-extend*, *turbulence modelling*, k - ω *SST*, γ - Re_θ, *turbulence transition*, *validation*

Sažetak

Računalna dinamika fluida (RDF) grana je dinamike fluide vezana uz analizu sustava koji uključuju strujanje fluida, prijenos topline i ostale srodne fenomene, putem računalnih simulacija. RDF se temelji na numeričkom rješavanju Navier-Stokes jednadžbi koje opisuju strujanje fluida. Modeliranje turbulencije smatra se jednim od ključnih aspekata RDF-a te se kao takav desetljećima usavršava. Iako je danas moguće precizno simulirati široki niz potpuno turbulentnih industrijskih strujanja, prihvaćeni modeli turbulencije još uvijek ne omogućavaju pouzdano simuliranje tranzicijskog strujanja u industrijskoj primjeni. Postojeći tranzicijski modeli turbulencije ograničeni su na teorijsku primjenu budući da se još uvijek nalaze u fazi validacije ili razvoja. Cilj ovog rada je, 2D simuliranjem strujanja fluida oko ravne ploče te aeroprofila Eppler 387, validirati tranzicijski model trubulencije γ - Re_θ usporedbom rezultata simulacija s onima dobro poznatog potpuno turbulentog k - ω SST modela turbulencije te s eksperimentalnim podacima. Također je procijenjena i numerička nesigurnost rezultata, u ovisnosti o gustoći mreža, u skladu s Eca i Hoekstra. Rezultati simulacija su u većini slučajeva pokazali dobro oponašanje tranzicijskih procesa te dobro slaganje s eksperimentalnim rezultatima.

Ključne riječi: *CFD*, *OpenFOAM*, *foam-extend*, *modeliranje turbulencije*, k - ω *SST*, γ - Re_θ, *tranzicija laminarnog u turbulentno strujanje*, *validacija*

Prošireni sažetak

Računalna dinamika fluida (RDF) grana je dinamike fluide vezana uz analizu sustava koji uključuju strujanje fluida, prijenos topline i ostale srodne fenomene, putem računalnih simulacija. Modeliranje turbulencije smatra se jednim od ključnih aspekata RDF-a te se kao takav desetljećima usavršava. Iako je danas moguće precizno simulirati široki niz potpuno turbulentnih industrijskih struanja poznati modeli turbulencije još uvijek ne omogućavaju pouzdano simuliranje tranzicijskog strujanja u industrijskoj primjeni. Cilj ovog rada je, 2D simuliranjem strujanja fluida oko ravne ploče te aeroprofila Eppler 387, validirati tranzicijski model trubulencije γ - Re_θ [8] usporedbom rezultata simulacija s onima dobro poznatog potpuno turbulentog k - ω SST modela turbulencije [9] te eksperimentalnim podacima.

Računalne simulacije prezentirane u ovom radu izvršene su u programskom paketu **OpenFOAM [11,12],** odnosno u njegovoj verziji **foam-extend-4.1 [12–14]**.

Matematički model

Početnom jednadžbom matematičkog modela prezentiranog u ovom radu smatra se opća skalarna transportna jednadžba:

$$\frac{\partial \phi}{\partial t} + \nabla \bullet (\phi \mathbf{u}) - \nabla \bullet (\gamma \nabla \phi) = q_v ,$$

gdje ϕ predstavlja opću skalarnu varijablu, t vrijeme, $\mathbf{u}$ vektorsko polje brzine, γ difuzijski koeficijent te q_v izvorski član. Iz opće skalarne transportne jednadžbe mogu se izvesti temeljne jednadžbe za opisivanje nestlačivog, izotermnog, izotropnog strujanja fluida bez utjecaja gravitacije. Navedene temeljne jednadžbe su jednadžba kontinuiteta:

$$\nabla \bullet \mathbf{u} = 0$$

te jednadžba očuvanja količine gibanja:

$$\frac{\partial \mathbf{u}}{\partial t} + \nabla \bullet (\mathbf{uu}) - \nabla \bullet (\nu \nabla \mathbf{u}) = -\frac{\nabla p}{\rho} ,$$

gdje ν predstavlja kinematičku viskoznost, p polje tlaka te ρ polje gustoće. Jednadžba kontinuiteta te jednadžba očuvanja količine gibanja zatim se vremenski usrednjavaju metodom Reynoldsovog usrednjavanja. Kao posljedica Reynoldsovog usrednjavanja u jednadžbi očuvanja količine gibanja javlja se tzv. Reynoldsov tenzor naprezanja $\overline{\mathbf{u}'\,\mathbf{u}'}$ koji se modelira putem Boussinesqove hipoteze [15]:

$$\overline{\mathbf{u}'\,\mathbf{u}'} = \nu_\mathrm{t}\left[\nabla\mathbf{u} + (\nabla\mathbf{u})^\mathrm{T}\right] - \frac{2}{3}k\mathbf{I}\,,$$

gdje ν_t predstavlja turbulentnu viskoznost, k turbulentnu kinetičku energiju te $\mathbf{I}$ jedinični tenzor. Utjecaj turbulencije opisan je skalarnim poljem turbulente viskoznosti ν_t do čije se vrijednosti dolazi rješavanjem dodatnih skalarnih transportnih jednadžbi, čiji broj ovisi o odabranom modelu turbulencije. Dodatne skalarne transportne jednadžbe odabranih modela turbulencije glase:

- **Potpuno turbulentni k - ω SST model turbulencije [9]:**

$$\frac{\partial(\rho k)}{\partial t} + \nabla \bullet (\rho\bar{\mathbf{u}}k) - \nabla \bullet [(\mu + \sigma_\mathrm{k}\mu_\mathrm{t})\nabla k] = \widetilde{P}_k - \beta^*\rho k\omega$$

$$\frac{\partial(\rho\omega)}{\partial t} + \nabla \bullet (\rho\bar{\mathbf{u}}\omega) - \nabla \bullet [(\mu + \sigma_\omega\mu_\mathrm{t})\nabla\omega] = \frac{\alpha}{\nu_\mathrm{t}}\widetilde{P}_k + 2(1 - F_1)\rho\sigma_{\omega 2}\frac{1}{\omega}\nabla k\nabla\omega$$

- **Tranzicijski γ - Re_θ model turbulencije [8]:**

$$\frac{\partial(\rho\gamma)}{\partial t} + \nabla \bullet (\rho\bar{\mathbf{u}}\gamma) - \nabla \bullet \left[\left(\mu + \frac{\mu_\mathrm{t}}{\sigma_\mathrm{f}}\right)\nabla\gamma\right] = P_\gamma - E_\gamma$$

$$\frac{\partial\left(\rho\widetilde{Re}_{\theta\mathrm{t}}\right)}{\partial t} + \nabla \bullet (\rho\bar{\mathbf{u}}\widetilde{Re}_{\theta\mathrm{t}}) - \nabla \bullet \left[\sigma_{\theta\mathrm{t}}(\mu + \mu_\mathrm{t})\nabla\widetilde{Re}_{\theta\mathrm{t}}\right] = P_{\theta\mathrm{t}}$$

$$\frac{\partial(\rho k)}{\partial t} + \nabla \bullet (\rho\bar{\mathbf{u}}k) - \nabla \bullet [(\mu + \sigma_\mathrm{k}\mu_\mathrm{t})\nabla k] = \hat{P}_k - \hat{D}_k$$

$$\frac{\partial(\rho\omega)}{\partial t} + \nabla \bullet (\rho\bar{\mathbf{u}}\omega) - \nabla \bullet [(\mu + \sigma_\omega\mu_\mathrm{t})\nabla\omega] = \frac{\alpha}{\nu_\mathrm{t}}\widetilde{P}_k + 2(1 - F_1)\rho\sigma_{\omega 2}\frac{1}{\omega}\nabla k\nabla\omega$$

Numerički model

Uvođenjem metode konačnih volumena (MKV) temeljne jednadžbe strujanja fluida se diskretiziraju. Budući da su provedene simulacije stacionarne u vremenu, vremenska domena se ne diskretizira, dok se prostorna domena diksretizira u proračunsku mrežu sastavljenu od konačnog broja ćelija (kontrolnih volumena). Time sustav temeljnih jednadžbi strujanja fluida poprima sljedeći matrični oblik koji vrijedi za svaki kontrolni volumen cijele proračunske domene:

$$\mathbf{A}\mathbf{x} = \mathbf{b}\ .$$

Prikazani matrični sustav, u sklopu ovog rada, se rješava iterativno pomoću implicitno spregnutog algoritma **pUCoupledFoam** [16].

Geometrija i proračunska domena

Geometrije korištene u 2D računalnim simulacijama su ravna ploča te aeroprofil Eppler 387. Za geometriju ravne ploče izrađena je jedna pravokutna proračunska domena koja je postavljena na gornju plohu ravne ploče. Iz tog razloga jedina potrebna dimenzija za definiranje geometrije je njena duljina $L = 1$m.

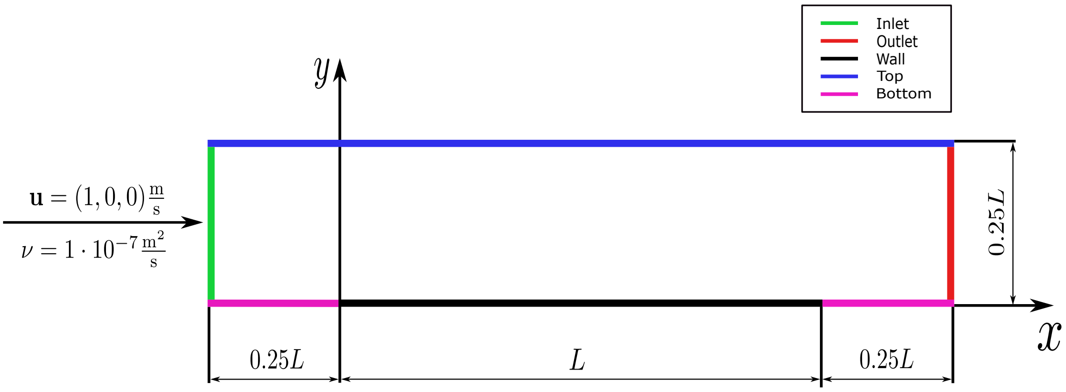

Slika 1: Računalna domena ravne ploče.

Za geometriju aeroprofila Eppler 387, duljine tetive $c = 1$m, izrađene su dvije pravokutne budući da se simulira opstrujavanje fluida oko geometrije pri napadnim kutevima $\alpha = 1^\circ$ te $\alpha = 7^\circ$.

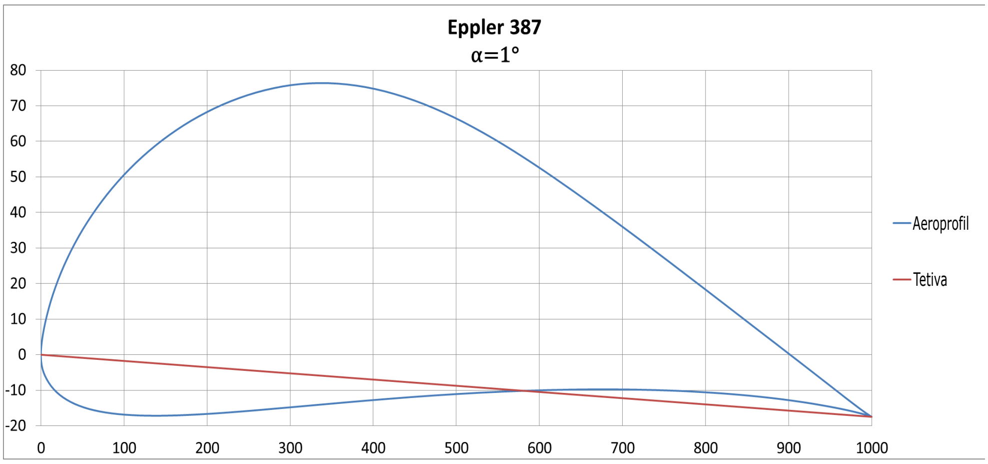

Slika 2: Aeroprofil Eppler 387 pri napadnom kutu $\alpha = 1^\circ$.

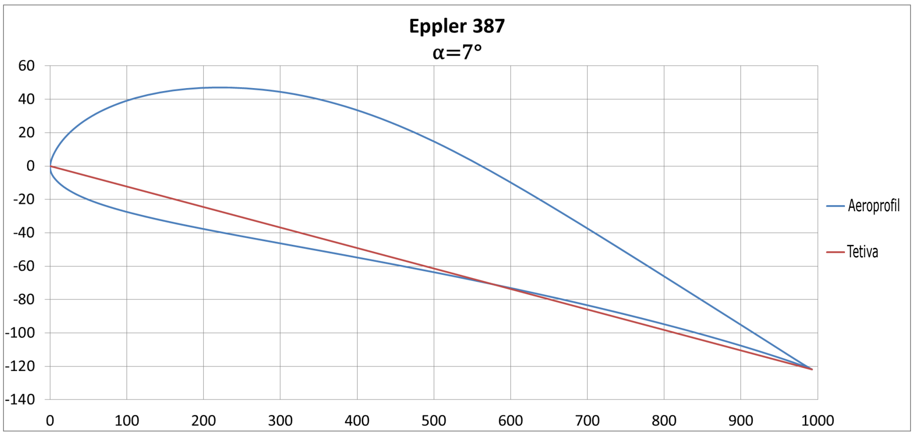

Slika 3: Aeroprofil Eppler 387 pri napadnom kutu $\alpha = 7°$.

Proračunske domene geometrije Eppler 387 jednakih su dimenzija te se izuzev napadnog kuta geometrije ne razlikuju.

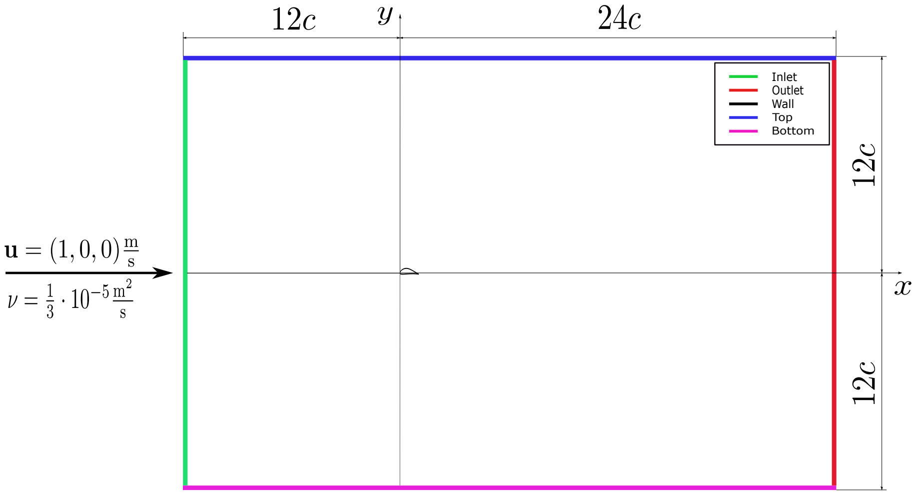

Slika 4: Primjer računalne domene aeroprofila Eppler 387.

Budući da je ovaj rad rađen u sklopu NATO Applied Vehicle Techonlogy (AVT) projekta, korištene su proračunske mreže koje su zadane unutar istog [17].

Validacija i analiza rezultata

Validacija tranzicijskog modela turbulencije γ - Re_θ provodi se usporedbom eksperimentalnih podataka s rezultatima numeričkih simulacija strujanja fluida preko ravne ploče te oko aeroprofila Eppler 387. Na računalnu domenu ravne ploče zadaju se dva skupa rubnih uvjeta. Prvi skup rubnih uvjeta, T3AM, predstavlja slučaj niskog intenziteta turbulencije, dok drugi skup rubnih uvjeta, T3A, predstavlja slučaj visokog intenziteta turbulencije. Na računalne domene aeroprofila Eppler 387 pod napadnim kutevima $\alpha = 1°$ te $\alpha = 7°$ zadaju se jednaki rubni uvjeti.

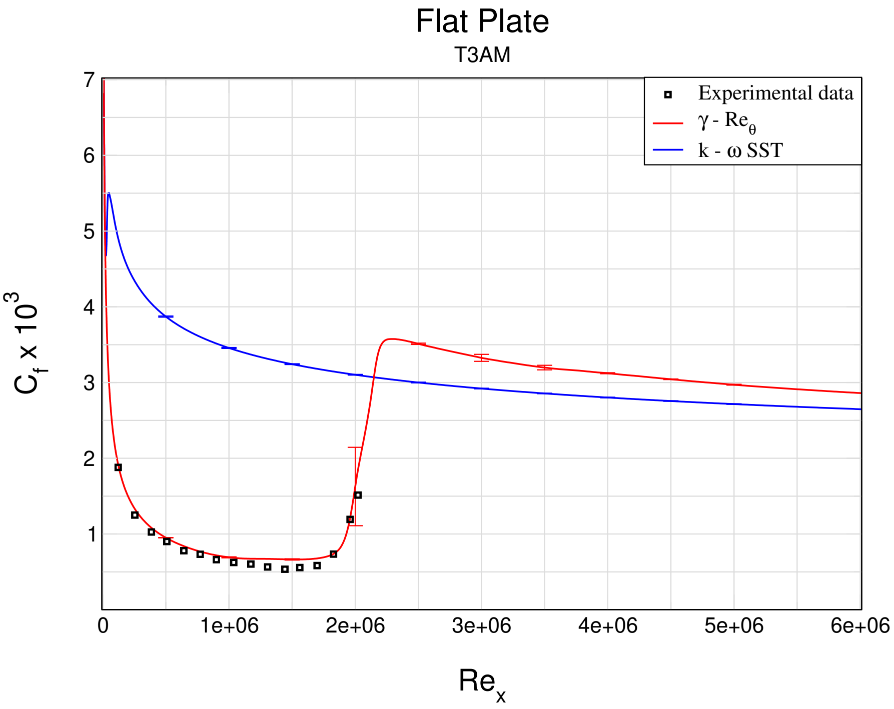

Slika 5: Usporedba raspodjele koeficijenta trenja duž ravne ploče (T3AM).

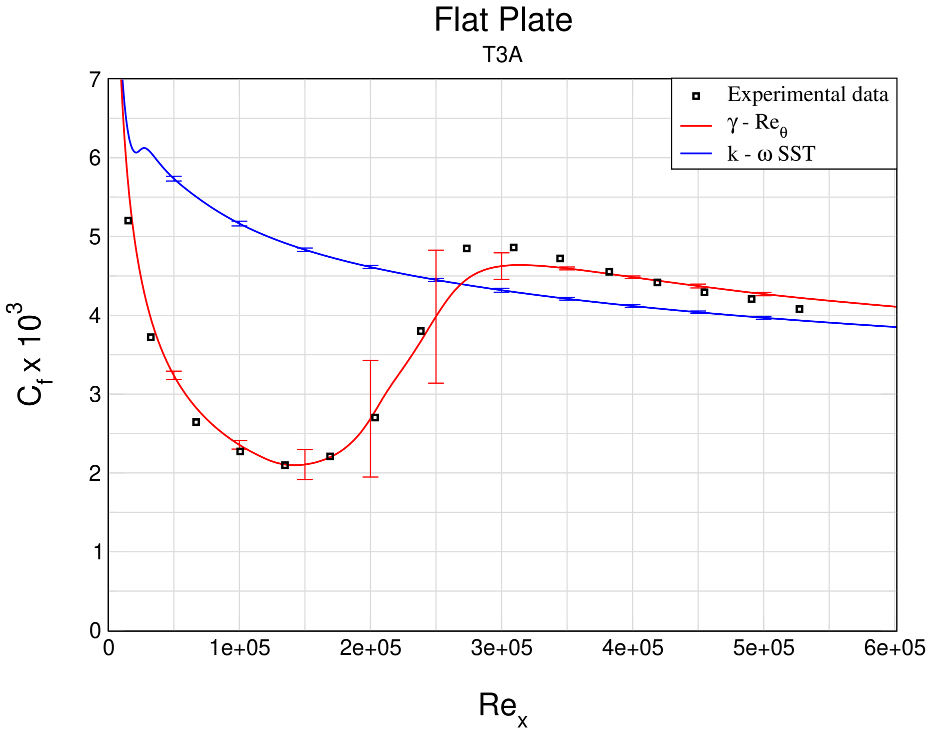

Slika 6: Usporedba raspodjele koeficijenta trenja duž ravne ploče (T3A).

Slika 5 i Slika 6 prikazuju usporedbu eksperimentalnih podataka te rezultata numeričkih simulacija raspodjele koeficijenta trenja duž ravne ploče. U oba slučaja je vidljivo da rezultati γ - Re_θ modela iskazuju bolje slaganje s eksperimentalnim podacima od k - ω SST modela. Tranzicijski model γ - Re_θ točno oponaša proces prirodne tranzicije, no može se primjetiti da numerička nesigurnost drastično raste u zoni tranzicije.

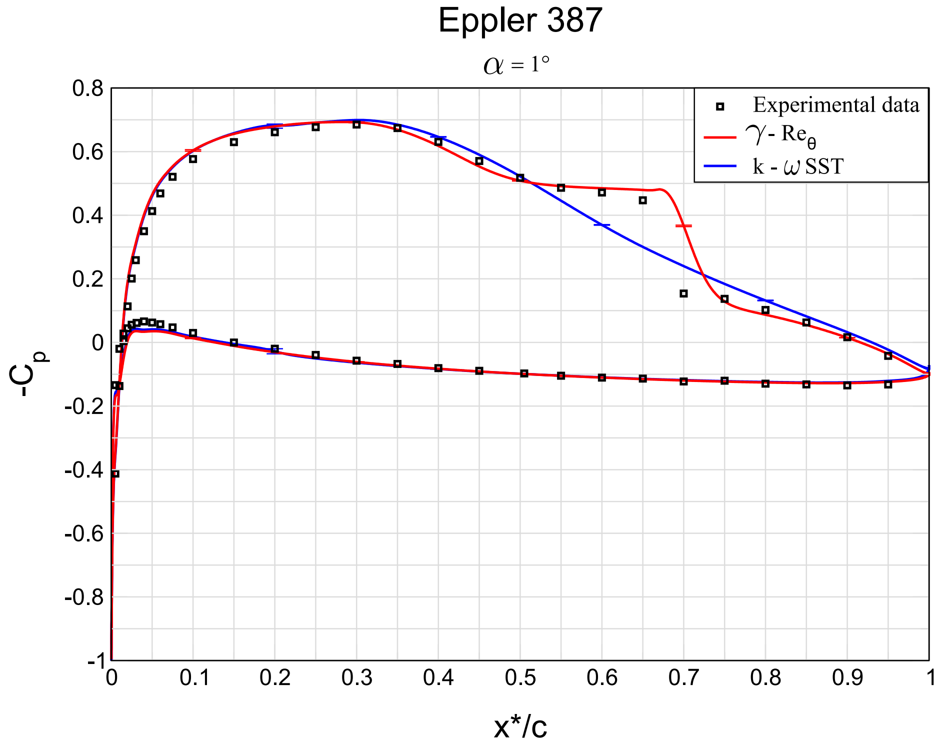

Slika 7: Usporedba raspodjele koeficijenta tlaka duž aeroprofila Eppler 387 pri kutu $\alpha = 1°$.

Slika 7 prikazuje usporedbu eksperimentalnih podataka i rezultata numeričkih simulacija raspodjele koeficijenta tlaka duž aeroprofila Eppler 387 pri napadnom kutu $\alpha = 1°$. Još jednom je vidljivo da rezultati γ - Re_θ modela iskazuju znatno bolje slaganje s eksperimentalnim podacima od k - ω SST modela. Tranzicijski model γ - Re_θ točno oponaša proces tranzicije uzrokovane odvajanjem strujanja, no može se primjetiti da točnost modela pada u području tranzicije.

	C_L	C_D	C_{Dp}	C_{Df}
Experimental data	0.465	$9.3 \cdot 10^{-3}$	–	–
k-ω SST	0.475	$13.223 \cdot 10^{-3}$	$2.475 \cdot 10^{-3}$	$10.748 \cdot 10^{-3}$
γ-Re_θ	0.487	$9.576 \cdot 10^{-3}$	$4.421 \cdot 10^{-3}$	$5.155 \cdot 10^{-3}$

Tablica 1: Usporedba koeficijenata uzgona i otpora aeroprofila Eppler pri kutu $\alpha = 1°$.

Tablica 1 prikazuje usporedbu eksperimentalnih podataka i rezultata numeričkih simulacija koeficijenata uzgona i otpora. Vidljivo je da za koeficijent uzgona k-ω SST iskazuje neznatno veće slaganje s eksperimentalnim podacima. Također je vidljivo da za koeficijent otpora γ-Re_θ iskazuje znatno veće slaganje s eksperimentalnim podacima, budući da k-ω SST značajno precjenjuje vrijednost koeficijenta otpora.

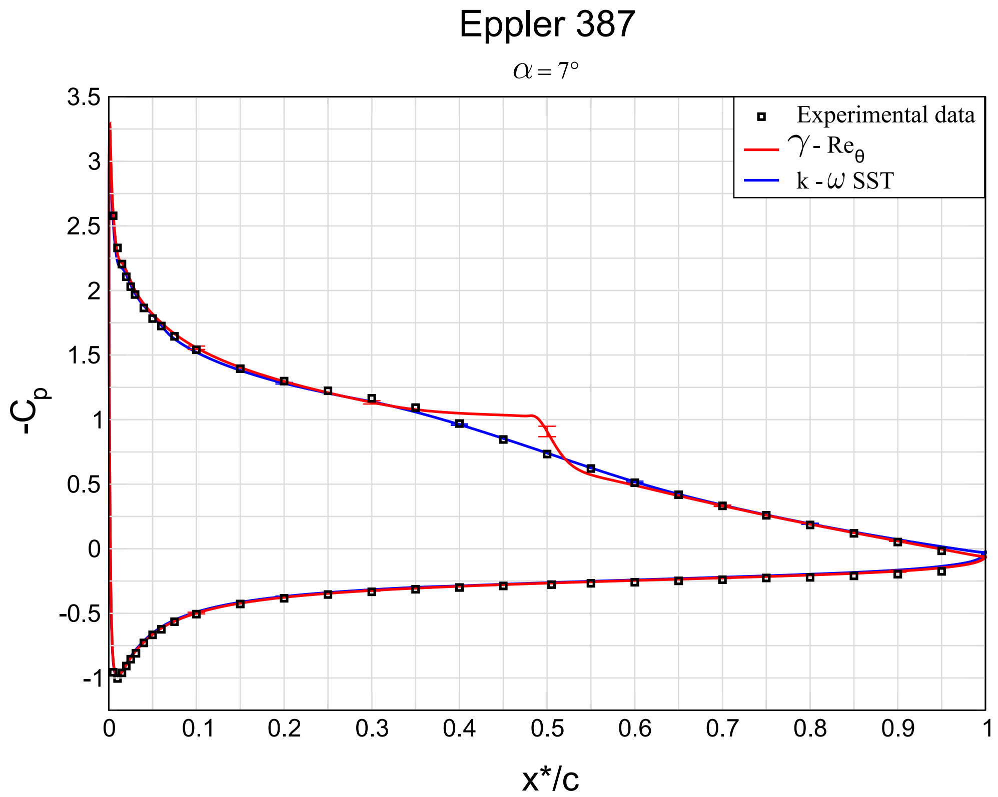

Slika 8: Usporedba raspodjele koeficijenta tlaka duž aeroprofila Eppler 387 pri kutu $\alpha = 7°$.

Slika 8 prikazuje usporedbu eksperimentalnih podataka i rezultata numeričkih simulacija raspodjele koeficijenta tlaka duž aeroprofila Eppler 387 pri napadnom kutu $\alpha = 1°$. Za razliku od prijašnjih slučajeva na Slici 8 je vidljivo da rezultati k - ω SST modela iskazuju bolje slaganje s eksperimentalnim podacima od γ - Re_θ modela. Tranzicijski model γ - Re_θ u ovom slučaju pogrešno oponaša proces tranzicije. Iako za promatrani slučaj prema eksperimentalnim podacima na aeroprofilu dolazi do prirodne tranzicije, γ - Re_θ pogrešno pretpostavlja tranziciju uzrokovanu odvajanjem strujanja što rezultira većim padom tlaka na podtlačnoj strani aeroprofila u odnosu na eksperimentalne podatke. Potrebno je provesti daljnja istraživanja kako bi se saznalo postoji li generalna greška u empirijskim korelacijama modela ili je ova pogreška iznimka.

	C_L	C_D	C_{Dp}	$C_{D\mathrm{f}}$
Experimental data	1.106	$12.9 \cdot 10^{-3}$	–	–
k-ω SST	1.09	$18.396 \cdot 10^{-3}$	$9.316 \cdot 10^{-3}$	$9.08 \cdot 10^{-3}$
γ-Re_θ	1.117	$14.029 \cdot 10^{-3}$	$9.62 \cdot 10^{-3}$	$4.409 \cdot 10^{-3}$

Tablica 2: Usporedba koeficijenata uzgona i otpora aeroprofila Eppler pri kutu $\alpha = 7°$.

Tablica 2 prikazuje usporedbu eksperimentalnih podataka i rezultata numeričkih simulacija koeficijenata uzgona i otpora. Vidljivo je da za koeficijent uzgona γ-Re_θ iskazuje neznatno veće slaganje s eksperimentalnim podacima. Također je vidljivo da za koeficijent otpora γ-Re_θ iskazuje znatno veće slaganje s eksperimentalnim podacima, budući da k-ω SST značajno precjenjuje vrijednost koeficijenta otpora.

Simulacije provedene pomoću k-ω SST modela turbulencije iskazale su veću stabilnost i kraće vrijeme konvergencije od simulacija provedenih pomoću γ - Re_θ model turbulencije.

Zaključak

Cilj ovog rada bio je, na temelju provedenih numeričkih simulacija, validirati tranzicijski model turbulencije γ - Re_θ. Rezultati 2D numeričkih simulacija strujanja fluida preko ravne ploče iskazali su odlično slaganje γ - Re_θ modela te eksperimentalnih podataka, za razliku od k - ω SST modela. γ - Re_θ model točno je predvidio te oponašao prirodnu tranziciju, no povećana numerička nesigurnost mogla se primjetiti u zoni tranzicije. Rezultati 2D numeričkih simulacija strujanja fluida oko aeroprofila Eppler 387 iskazali su odlično slaganje γ - Re_θ modela te eksperimentalnih podataka za strujanje oko aeroprofila pri napadnom kutu $\alpha = 1°$, no pri napadnom kutu $\alpha = 7°$ rezultati ne pokazuju jednako dobro slaganje s eksperimentalnim podacima. Pri napadnom kutu $\alpha = 1°$ γ - Re_θ model točno predviđa tranziciju uzrokovanu odvajanjem strujanja te su rezultati zadovoljavajući unatoč malom padu točnosti u zoni tranzicije. Pri napadnom kutu $\alpha = 7°$ γ - Re_θ model pogrešno predviđa tranziciju uzrokovanu odvajanjem strujanja umjesto prirodne tranzicije koja se javlja prema eksperimentalnim podacima. Razlog pogreške je nepoznat te je potrebno provestidaljnja istraživanja kako bi se saznalo postoji li generalna greška u empirijskim korelacijama modela ili je ova pogreška iznimka. Unatoč tome, pri napadnom kutu $\alpha = 7°$ rezultati koeficijenta uzgona i otpora γ - Re_θ modela iskazuju veće slaganje s eksperimentalnim podacima.

1 Introduction

1.1 Background

First description of laminar and turbulent flows was given by Osborne Reynolds in 1883. In his experiment Reynolds used three tubes of different diameters, fitted with trumpet mouthpieces. The tubes were immersed in a large gas tank filled with clear water and used to draw water out of the tank. He then injected dye in the tubes and observed that the dye, when the velocities were sufficiently low, extended through the tubes in a straight line, depicting laminar flow (Figure 1.1).

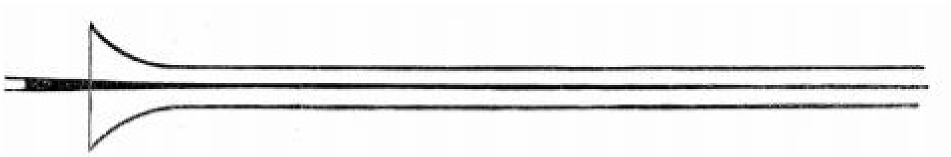

Figure 1.1: The Reynolds experiment, the dye extended in a straight line [1]

However, as he gradually increased velocity, Reynolds observed that at some point in the tube the dye mixes with the surrounding clear water filling the tube with a mass of coloured water, depicting turbulent flow (Figure 1.2).

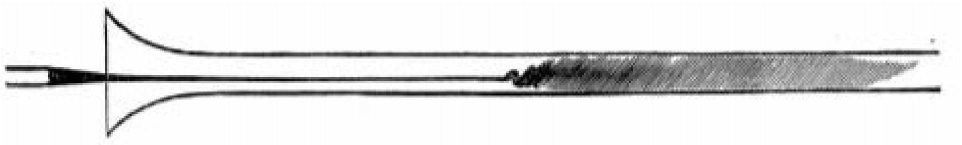

Figure 1.2: The Reynolds experiment, the tube filled with a mass of coloured water [1]

With further increase in velocity the point in which straight line transitions in a mass of coloured water moved closer to the trumpet mouthpiece, never reaching it. Furthermore when viewing the tubes by the light of an electric spark the mass of coloured water resolved itself into eddies (Figure 1.3) which are, along with intensive mixing, another key characteristic of turbulent flow [1].

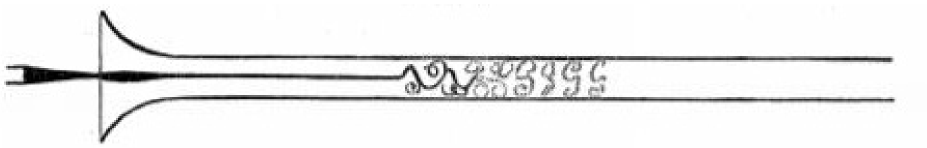

Figure 1.3: The Reynolds experiment, coloured water under the light of an electric spark [1].

In 1894 Reynolds established that these flow regimes are characterized by a dimensionless parameter today known as the Reynolds number [18]. The Reynolds number represents the ratio of fluids inertial to viscous forces and is defined as:

$$Re = \frac{\rho U L}{\mu} , \tag{1.1}$$

where ρ is the density of the fluid, U mean velocity, L characteristic linear dimension and μ dynamic viscosity of the fluid. Reynolds number representing the start of laminar-to-turbulent transition is called the critical Reynolds number.

Prandtl physically predicted and Tollmien mathematically proved that a laminar boundary layer can be destabilized by viscous instability waves, today known as Tollmien-Schlichting waves. At the critical Reynolds number, when the free-stream turbulence levels are lower than 1%, Tollmien-Schlichting (T-S) waves start to grow and laminar boundary layer becomes linearly unstable, marking the beginning of laminar-to-turbulent transition flow. Further downstream waves become nonlinear and three-dimensional (3D) disturbances are created. Finally, turbulent spots appear and they grow in the surrounding laminar layer until a fully turbulent boundary layer is created (Figure 1.4), thus completing the process known as natural transition.

For the case of swept wings with large sweep angles a 3D boundary layer with a significant velocity component in the sweep direction develops near the wall. This is referred to as cross-flow and can cause instability of the boundary layer which leads to the occurrence of the transition significantly earlier than pure T-S waves [2].

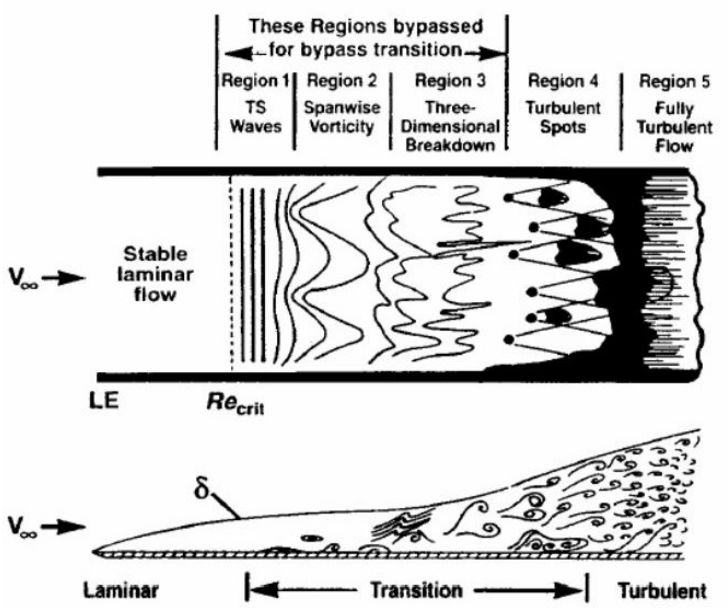

Figure 1.4: Sketch of the natural transition process (Schlichting, 1979) [2].

Other notable transition processes are bypass transition, wake-induced transition and separated flow transition. Bypass transition occurs when free-stream turbulence levels are higher than 1%. This can cause first and possibly second and third stages of the natural transition process to be bypassed so that turbulent spots are directly produced within the boundary layer by the influence of free-stream disturbances (Figure 1.4). It is important to note that bypass transition can also occur due to surface roughness or due to injection of turbulent flow directly into the boundary layer.

Wake induced transition is a special instance of bypass transition that occurs in turbomachinery flows as blade rows are subjected to periodically passing turbulent wakes. These turbulent wakes are disruptive to the laminar boundary layer and as a result they cause formation of turbulent spots at the point where the wake impinges on the surface. However, as the wake passes, the boundary layer will slowly revert to laminar flow.

Separated flow transition occurs as a result of flow separation due to strong adverse pressure gradient. When a laminar boundary layer separates, transition may occur in the shear layer of the separated flow. As a result, enhanced mixing caused by turbulence can lead to reattachment of the shear layer, forming a laminar-separation/turbulent-reattachment bubble on the surface of an airfoil. The transition process within the shear layer may involve all stages of the natural transition process (Figure 1.4) and it directly affects the bubble length. The bubbles are classified as long or short, based on their effect on the pressure distribution around an airfoil. While short bubbles have a local effect, long bubbles can completely change the pressure distribution around an airfoil (Figure 1.5) [2].

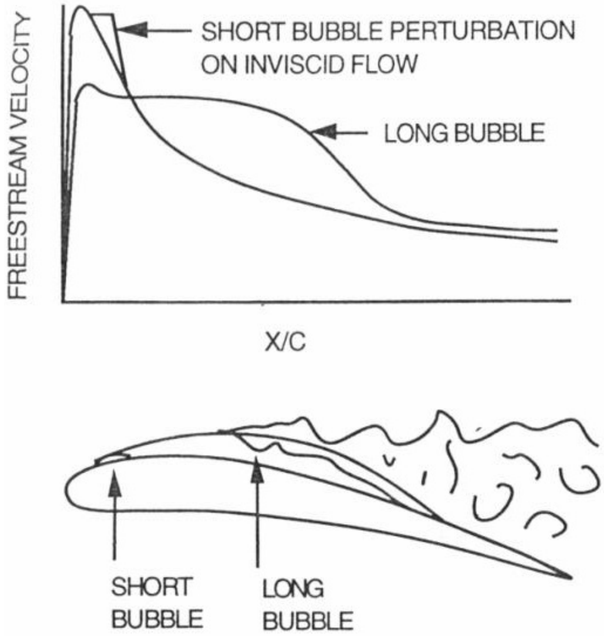

Figure 1.5: Effects of the separation bubble on suction side velocity distribution [2].

1.2 Laminar-to-Turbulent Transition in Computational Fluid Dynamics

Computational Fluid Dynamics (CFD) is a branch of fluid dynamics associated with the analysis of systems involving fluid flow, heat transfer and other related phenomena by means of computer-based simulation. Turbulence modelling is considered as one of the key aspects of CFD and in the past few decades it improved significantly. Rapid progress of CFD and turbulence modelling enabled engineers to accurately simulate wide range of fully turbulent engineering flows. However, turbulence models that include the effects of laminar-to-turbulent transition (transitional turbulence models) still aren't sufficiently mature for regular use in industrial CFD for several reasons.

The first reason is that, depending on the flow and geometry conditions, transition can occur through different mechanisms (e.g. natural transition, bypass transition and separated flow transition). It is also possible for a turbulent boundary layer to re-laminarize under the influence of a strong favourable pressure gradient. Combining these effects into a single reliable transitional turbulence model still represents a challenge to the engineers.

Furthermore, Reynolds averaged Navier-Stokes (RANS) procedures eliminate the effects of linear disturbance growth. Considering that both linear and non-linear effects are relevant for the description of transitional flows, this represents another serious complication. This issue can be circumvented by the use of methods based on stability equations such as the e^n method. However, even though useful, stability analysis involves non-local operations (e.g. tracking the disturbance growth along each streamline) and requires prior knowledge of geometry and mesh topology [4]. All this makes implementation of stability analysis into industrial CFD for day-to-day operations problematic, as tracking of individual disturbances in a complex geometry and under variable flow conditions is completely impractical for the current formulation discretisation practice of CFD tools.

In addition to stability analysis, engineers have also been developing low-Re models and correlation based models in an attempt to accurately predict transition. Low-Re models completely rely on the ability of the wall damping terms to capture the effects of transition. Their main problem is close interaction between transition and viscous sublayer modelling as this can prevent independent calibration of both. For this reason low-Re models can at best be expected to simulate bypass transition which is dominated by diffusion effects from the free-stream.

Correlation based models usually correlate the transition momentum-thickness Reynolds number (Re_θ) to local free-stream conditions such as the turbulence intensity (Tu) and pressure gradient. Empirical correlations are relatively easy to calibrate, can be developed for different transition mechanisms and are often sufficiently accurate to capture major effects of transition processes. However they typically require information on the integral thickness of the boundary layer and flow conditions outside of it. This non-local formulation represents main issue in the implementation of correlation based models into general-purpose CFD codes [2].

Other applicable tools used for transition prediction are Large Eddy Simulations (LES) and Direct Numerical Simulations (DNS). However, they are far too expensive for engineering applications and therefore won't be included in this thesis. A practical CFD model of turbulent transition needs to be based on local properties and transport equations: this is the main characteristic of the model considered in this Thesis.

1.3 Thesis Outline

This Thesis is organised in six Chapters. Chapter 1 served as introduction, offering a brief overview of laminar-to-turbulent transition processes and their modelling with CFD tools. Chapter 2 presents mathematical model, describing governing equation of fluid flow and used turbulence models. Chapter 3 presents numerical model, describing the Finite Volume Method (FVM) used for CFD simulations. Chapter 4 defines geometries, resulting computational domains and meshes used in the Thesis, while also listing the corresponding boundary conditions. Chapter 5 presents analysis and validation of results. Finally, Chapter 6 serves as the Conclusion of the Thesis, followed by an Appendix offering an overview of the simulation discretisation and solver settings.

2 | Mathematical Model

2.1 Introduction

The previous chapter served as an introduction, describing the types of fluid flow with regards to turbulence, focusing on laminar-to-turbulent transitional flow and its modelling in CFD. The following chapter shall serve as an overview of the theoretical background required to successfully understand the mathematical model validated in this thesis.

2.2 The Scalar Transport Equation

When observing a region of space, Reynolds Transport Theorem (RTT) can be used to describe the rate of change of a general property ϕ in the observed region (Control Volume). The Control Volume (CV) represents a closed system in which the rate of change of the general property ϕ is equal to the sum of the change of property inside of the CV and the net rate of outflow through the surface enclosing the CV (Figure 2.1).

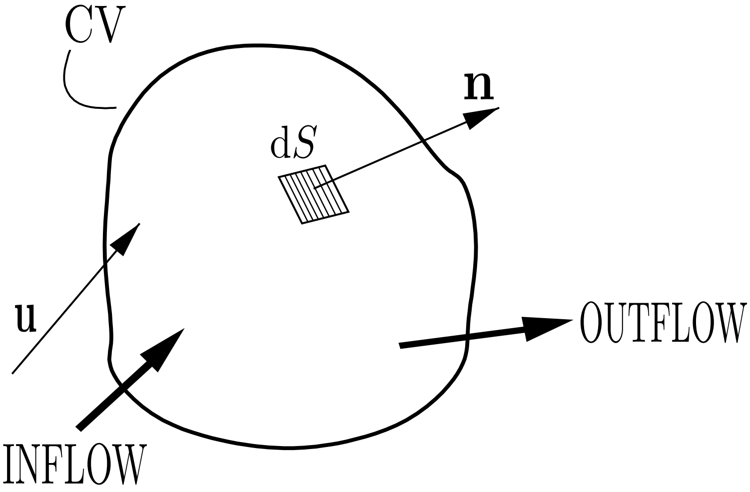

Figure 2.1: The Control Volume [3].

The RTT for the CV can be written as follows:

$$\frac{\mathrm{d}}{\mathrm{d}t}\int_{V_{\mathrm{m}}} \phi \,\mathrm{d}V = \int_{V_{\mathrm{m}}} \frac{\partial \phi}{\partial t}\,\mathrm{d}V + \oint_{S_{\mathrm{m}}} \phi(\mathbf{n}\bullet\mathbf{u})\,\mathrm{d}S\,. \tag{2.1}$$

In order to transform the surface integral in Eq. 2.1 the Gauss' Theorem must be introduced. The general form of the Gauss' Theorem is:

$$\int_{V_\mathrm{P}} \nabla \bullet \mathbf{a} \, \mathrm{d}V = \oint_{\partial V_\mathrm{P}} \mathrm{d}\mathbf{s} \bullet \mathbf{a} = \oint_{\partial V_\mathrm{P}} \mathrm{d}\mathbf{n} \bullet \mathbf{a} \, \mathrm{d}S \, . \tag{2.2}$$

Transforming the surface integral (Eq. 2.1) to a volume integral through the Gauss' Theorem (Eq. 2.2) the RTT for the CV takes the following form:

$$\frac{\mathrm{d}}{\mathrm{d}t} \int_V \phi \, \mathrm{d}V = \int_V \left[\frac{\partial \phi}{\partial t} + \nabla \bullet (\phi \mathbf{u}) \right] \mathrm{d}V \, . \tag{2.3}$$

Eq. 2.3 is used to model the convective transport of the general property ϕ facilitated by the convective velocity $\mathbf{u}$. The inflow of the general property ϕ is given by $(\mathbf{u} \cdot \mathbf{n}) < 0$ and the outflow by $(\mathbf{u} \cdot \mathbf{n} > 0)$, defining the convective flux. Beside the convective transport, surface and volume sources/sinks also contribute to the change of ϕ inside the CV.

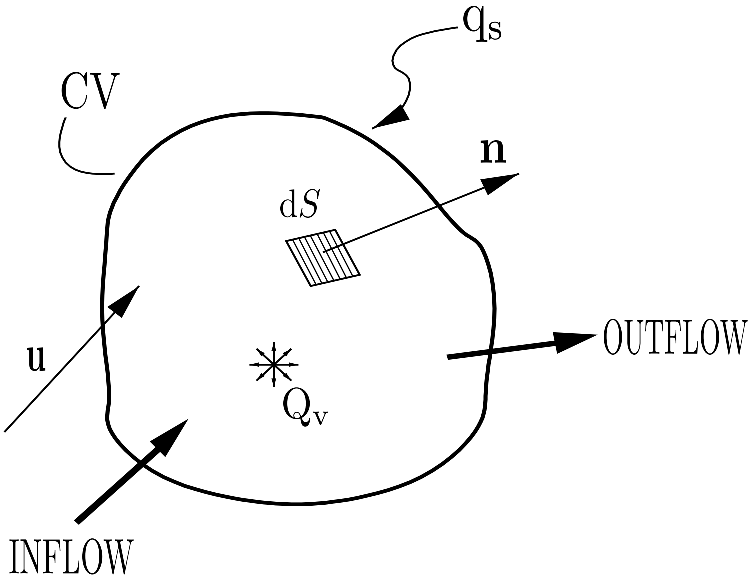

Figure 2.2: Surface and Volume sources of the CV [3].

Contribution of surface and volume sources can be described as:

$$\frac{\mathrm{d}}{\mathrm{d}t} \int_V \phi \, \mathrm{d}V = \int_V q_v \, \mathrm{d}V - \oint_S (\mathbf{n} \bullet \mathbf{q}_s) \, \mathrm{d}S \, . \tag{2.4}$$

As the left hand side of Eq. 2.4 is equal to that of Eq 2.3 it can be stated that:

$$\int_V \left[\frac{\partial \phi}{\partial t} + \nabla \bullet (\phi \mathbf{u}) \right] \mathrm{d}V = \int_V q_v \, \mathrm{d}V - \oint_S (\mathbf{n} \bullet \mathbf{q}_s) \, \mathrm{d}S \, . \tag{2.5}$$

By applying the Gauss' Theorem (2.2) to the source term in the previous equation (Eq. 2.5) and integrating over the volume of the CV, considering that $V = constant$, the following equation can be obtained:

$$\frac{\partial \phi}{\partial t} + \nabla \bullet (\phi \mathbf{u}) = q_v - \nabla \bullet \mathbf{q}_s \, . \tag{2.6}$$

Terms representing surface sources are modelled using the Diffusive Transport model, a gradient-based model. According to the Diffusive Transport model, if a general property ϕ is considered as a concentration of a scalar variable in a closed domain (CV) it will be transported from regions of high concentration to regions of low concentration until uniform concentration is reached [19]. Using this model, surface sources are modelled as:

$$\mathbf{q}_s = -\gamma \nabla \phi \, . \tag{2.7}$$

Gradient of a general property, $\nabla\phi$, points in the direction of greater concentration of ϕ . On the other hand, the diffusive transport, governed by the diffusivity γ, occurs in the opposite direction. By inserting Eq. 2.7 into Eq. 2.6 and rearranging variables, the General Scalar Transport Equation can be obtained:

$$\underbrace{\frac{\partial \phi}{\partial t}}_{\text{temporal derivative}} + \underbrace{\nabla \bullet (\phi \mathbf{u})}_{\text{convection term}} - \underbrace{\nabla \bullet (\gamma \nabla \phi)}_{\text{diffusion term}} = \underbrace{q_v}_{\text{source term}} \, . \tag{2.8}$$

The temporal derivative from the General Scalar Transport Equation (Eq. 2.8) represents the inertia of the system (CV). The convection term is a hyperbolic term that represents the amount of the general property ϕ transported in or out of the system by the velocity $\mathbf{u}$. The diffusion term is an elliptic term that represent gradient transport of ϕ. Lastly, the source (or sink) term accounts for non-transport effects, it defines local production of ϕ in case of a source and destruction in case of a sink [19].

2.3 Governing equations of fluid flow

Mathematical model used in this thesis disregards the influence of gravitational forces while describing incompressible, isothermal, isotropic flow of a Newtonian fluid. Laws that govern such fluid flow are conservation of mass and conservation of linear momentum, while conservation of energy is ignored considering that the fluid flow is isothermal. These laws are described by a set of Navier-Stokes equations.

2.3.1 Conservation of Mass

Conservation of mass is described by the continuity equation. Continuity equation can be derived from the General Scalar Transport Equation (Eq. 2.8) by substituting the general property ϕ with fluid density ρ and defining a zero value source term.

$$\frac{\partial \rho}{\partial t} + \nabla \bullet (\rho \mathbf{u}) = 0 \, . \tag{2.9}$$

However considering that the described fluid flow is incompressible the density of the fluid is constant, in which case the continuity equation (Eq.2.9) can be simplified to:

$$\nabla \bullet \mathbf{u} = 0 \, . \tag{2.10}$$

2.3.2 Conservation of Linear Momentum

Conservation of linear momentum is described by the Cauchy momentum equation.

$$\underbrace{\frac{\partial (\rho \mathbf{u})}{\partial t}}_{\text{temporal derivative}} + \underbrace{\nabla \bullet (\rho \mathbf{u}\mathbf{u})}_{\text{convection}} = \underbrace{\rho \mathbf{f}}_{\text{body forces}} + \underbrace{\nabla \bullet \boldsymbol{\varsigma}}_{\text{surface forces}} \, , \tag{2.11}$$

where $\mathbf{f}$ is the body force and ς is the Cauchy stress tensor. Body force term represents forces acting throughout the whole body of the control volume, e.q. gravitational or electromagnetic forces. Considering that the influence of such forces is disregarded in this thesis, it will be ignored when further discussing the equation. Surface force term represents forces acting on surfaces of the control volume. It can be divided into the pressure gradient term and viscous force term so that Eq. 2.11 takes the following form:

$$\underbrace{\frac{\partial (\rho \mathbf{u})}{\partial t}}_{\text{temporal derivative}} + \underbrace{\nabla \bullet (\rho \mathbf{u}\mathbf{u})}_{\text{convection}} = - \underbrace{\nabla p}_{\text{pressure gradient}} + \underbrace{\nabla \bullet \boldsymbol{\tau}}_{\text{viscous forces}} \, . \tag{2.12}$$

If Eq. 2.12 is rearranged and Newton's law of viscosity is implemented the following form of the equation can be obtained [15]:

$$\underbrace{\frac{\partial (\rho \mathbf{u})}{\partial t}}_{\text{temporal derivative}} + \underbrace{\nabla \bullet (\rho \mathbf{u}\mathbf{u})}_{\text{convection}} - \underbrace{\nabla \bullet (\mu \nabla \mathbf{u})}_{\text{diffusion}} = - \underbrace{\nabla p}_{\text{source term}} \, . \tag{2.13}$$

It can now be seen that, with the pressure gradient acting as the source, the momentum equation (Eq. 2.13) can be obtained from the General Scalar Transport Equation (Eq. 2.8) by replacing the general property ϕ with the linear momentum vector $\rho\mathbf{u}$. Finally, Eq. 2.13 can be further simplified by dividing it with pressure ρ:

$$\frac{\partial \mathbf{u}}{\partial t} + \nabla \bullet (\mathbf{u}\mathbf{u}) - \nabla \bullet (\nu \nabla \mathbf{u}) = -\frac{\nabla p}{\rho} \; . \tag{2.14}$$

2.4 Reynolds Averaged Navier-Stokes Equations

Since most flows of engineering significance are turbulent, turbulence is not just of theoretical interest. Turbulence is a chaotic and random state of motion in which the velocity and pressure continuously fluctuate, which makes it impossible to describe turbulence analytically. From the engineering standpoint it is usually unnecessary to resolve the details of the turbulent fluctuations. Therefore, for the majority of the engineering problems turbulence is resolved by procedures based on Reynolds Averaged Navier-Stokes (RANS) equations. The idea of RANS equations is to decompose observed variables $(\mathbf{u}, p)$ into their mean $(\overline{\mathbf{u}}, \overline{p})$ and fluctuating $(\mathbf{u}', p')$ values, this is known as the Reynolds decomposition [15].

$$\begin{aligned} \mathbf{u} &= \overline{\mathbf{u}} + \mathbf{u}' \; , \\ p &= \overline{p} + p' \; . \end{aligned} \tag{2.15}$$

By time-averaging Navier-Stokes equations (Eq. 2.10 and 2.14), in accordance with this procedure (Eq. 2.15), following expressions can be obtained for the continuity and linear momentum equations:

$$\nabla \bullet \overline{\mathbf{u}} = 0 \; , \tag{2.16}$$

$$\frac{\partial \overline{\mathbf{u}}}{\partial t} + \nabla \bullet (\overline{\mathbf{u}}\,\overline{\mathbf{u}}) - \nabla \bullet (\nu\; \nabla\, \overline{\mathbf{u}}) = -\frac{\nabla\, \overline{p}}{\rho} + \nabla \bullet (\overline{\mathbf{u}'\,\mathbf{u}'}) \; . \tag{2.17}$$

The term $\overline{\mathbf{u}'\,\mathbf{u}'}$ from Eq. 2.17 is a second rank symmetric tensor known as the Reynolds stress tensor. The Reynolds stress tensor has 6 unknown components which need to be modelled in order to close presented system of equations (Eq. 2.16 and 2.17). This is done in accordance with the Boussinesq hypothesis. Unknown components of the Reynolds stress tensor are modeled as one unknown scalar field of turbulent kinematic viscosity [19].

$$\overline{\mathbf{u}'\,\mathbf{u}'} = \nu_{\mathrm{t}} \left[\nabla \mathbf{u} + (\nabla \mathbf{u})^{\mathrm{T}} \right] - \frac{2}{3} k \mathbf{I} \; , \tag{2.18}$$

where ν_t is turbulent kinematic viscosity, k turbulent kinetic energy and $\mathbf{I}$ the identity tensor. Turbulent kinetic energy represents the energy of the fluctuating component of the velocity field and can be expressed as:

$$k = \frac{1}{2}\overline{\mathbf{u}'\,\mathbf{u}'}\ . \tag{2.19}$$

Turbulent kinematic viscosity field is solved by additional scalar transport equations in accordance with the chosen turbulence model.

2.5 k - ω Shear Stress Transport Turbulence Model

The k - ω Shear Stress Transport (SST) turbulence model was presented by F.R. Menter in 1993. It is a two equation turbulence model developed as a combination of the k - ε model [20] and Wilcox's original k - ω model [21]. In the inner 50% of the boundary layer k - ω SST is identical to the Wilcox's k - ω model and from there it gradually transforms into the k - ε model until it reaches free shear layers, where it is identical to the k - ε model. By doing so, Menter avoided main flaws of both models, primarily, numerical problems while solving viscous sublayer with the k - ε model and k - ω model's strong dependency on imposed free-stream values [9]. It is important to note that all three models are fully turbulent and are not capable of modelling transitional flow.

k - ω SST solves two additional scalar transport equations: one for the turbulent kinetic energy k and another for specific turbulent dissipation rate ω. These equations are based on the original k - ω and transformed k - ε scalar transport equations, with incorporated blending functions.

$$\frac{\partial(\rho k)}{\partial t} + \nabla \bullet (\rho\bar{\mathbf{u}}k) - \nabla \bullet [(\mu + \sigma_\mathrm{k}\mu_\mathrm{t})\nabla k] = \widetilde{P}_k - \beta^* \rho k \omega\ , \tag{2.20}$$

$$\frac{\partial(\rho \omega)}{\partial t} + \nabla \bullet (\rho\bar{\mathbf{u}}\omega) - \nabla \bullet [(\mu + \sigma_\omega\mu_\mathrm{t})\nabla \omega] = \frac{\alpha}{\nu_\mathrm{t}}\widetilde{P}_k + 2(1-F_1)\rho\sigma_{\omega 2}\frac{1}{\omega}\nabla k \nabla \omega\ , \tag{2.21}$$

where F_1 is the blending function and $\widetilde{P}_k$ production limiter, while variations of α, β and σ represent model constants [22].

β^*	α_1	β_1	$\sigma_{\mathrm{k}1}$	$\sigma_{\omega 1}$	α_2	β_2	$\sigma_{\mathrm{k}2}$	$\sigma_{\omega 2}$	a_1
0.09	5/9	3/40	0.85	0.5	0.44	0.0828	1	0.856	0.31

Table 2.1: Constants of k - ω SST turbulence model [7].

The blending function F_1 is equal to 0 away from the surface (k - ε model) and switches to 1 inside the boundary layer (k - ω model) [7]. It is defined by:

$$F_1 = \tanh\left\{\left\{\min\left[\max\left(\frac{\sqrt{k}}{\beta^*\omega y}, \frac{500\nu}{y^2\omega}\right), \frac{4\rho\sigma_{\omega 2}\, k}{CD_{k\omega}\, y^2}\right]\right\}^4\right\} , \tag{2.22}$$

where y is the distance to the nearest wall and $CD_{\mathrm{k}\omega}$ is:

$$CD_{\mathrm{k}\omega} = \max\left(2\rho\sigma_{\omega 2}\frac{1}{\omega}\nabla k\, \nabla\omega, 10^{-10}\right) . \tag{2.23}$$

Turbulent kinematic viscosity is defined as follows:

$$\nu_t = \frac{a_1 k}{\max(a_1\omega, SF_2F_3)} , \tag{2.24}$$

where S is the absolute value of the strain-rate tensor, while F_2 and F_3 are second and third blender functions. The absolute value of the strain-rate tensor S is defined by:

$$S = \sqrt{2\,\mathbf{S}\,\mathbf{S}} , \qquad \mathbf{S} = \frac{1}{2}\left(\nabla\overline{\mathbf{u}} + \nabla\overline{\mathbf{u}}^{\mathrm{T}}\right) . \tag{2.25}$$

Second blending function F_2 is defined by:

$$F_2 = \tanh\left\{\left[\max\left(\frac{2\sqrt{k}}{\beta^*\omega y}, \frac{500\nu}{y^2\omega}\right)\right]^2\right\} . \tag{2.26}$$

Third blending function F_3 is an extension to the original k - ω SST model developed by Hellsten in colaboration with Menter [23]. It is given by:

$$F_3 = 1 - \tanh\left[\left(\frac{150\nu}{\omega y^2}\right)^4\right] . \tag{2.27}$$

Lastly, the production limiter $\widetilde{P_k}$ is used to prevent the build-up of turbulence in stagnation regions and is defined as follows:

$$\widetilde{P_{\mathrm{k}}} = \min\left(P_{\mathrm{k}}, 10\cdot\beta^*\rho k\omega\right) , \tag{2.28}$$

where P_k is production defined by [7]:

$$P_k = \mu_\mathrm{T} \left(\nabla\overline{\mathbf{u}} + \nabla\overline{\mathbf{u}}^\mathrm{T}\right) \nabla\overline{\mathbf{u}} \; . \tag{2.29}$$

Recommended boundary conditions are

$$\frac{10^{-5}U_\infty}{Re_L} < k_\infty < \frac{0.1U_\infty}{Re_L} \; , \qquad \frac{U_\infty}{L} < \omega_\infty < 10\frac{U_\infty}{Re_L} \; , \tag{2.30}$$

at inlets and

$$k = 0 \; , \qquad \omega = 10\frac{6\nu}{\beta_1(\Delta y_1)^2} \; , \tag{2.31}$$

at a wall. Here, L is the approximate length of the computational domain and Δy_1 is distance from the wall to the center of the first cell from the wall.

2.6 γ - Re_θ Turbulence Model

γ - Re_θ is a correlation-based, transitional turbulence model developed by F. R. Menter and R. B. Langtry. It solves 4 scalar transport equations: turbulent kinetic energy k, specific turbulent dissipation rate ω, intermittency γ and the local transition onset momentum thickness Reynolds number $\widetilde{Re}_{\theta\mathrm{t}}$. Only local variables and gradients, as well as the wall distance, are used in the equations. In order to trigger the onset of transition the strain-rate Reynolds number Re_ν is used:

$$Re_\mathrm{v} = \frac{y^2 S}{\nu} \; , \tag{2.32}$$

where y is the distance from the nearest wall, ν fluid kinematic viscosity and S the absolute value of the strain rate tensor (Eq. 2.25):

$$S = \sqrt{2\,\mathbf{S}\,\mathbf{S}} \; , \qquad \mathbf{S} = \frac{1}{2}\left(\nabla\overline{\mathbf{u}} + \nabla\overline{\mathbf{u}}^\mathrm{T}\right) \; .$$

The strain-rate Reynolds number Re_v is then scaled so that it has a maximum at the value of 1 inside the boundary layer. This is done by dividing the strain-rate Reynolds number profile from the Blasius solution by the corresponding momentum thickness Reynolds number Re_θ and a constant of 2.193 (Figure 2.3). The momentum thickness Reynolds number is defined as:

$$Re_\theta = \frac{\theta U_\infty}{\nu} \; , \tag{2.33}$$

where θ is momentum thickness and U_∞ free-stream velocity.

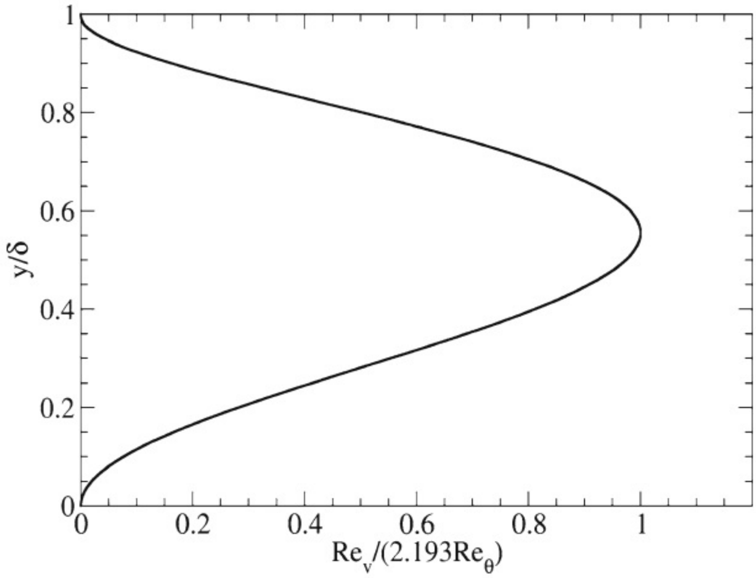

Figure 2.3: Scaled strain-rate Reynolds number profile in a Blasius boundary layer [4].

Consequently the maximum of the profile is proportional to the momentum thickness Reynolds number Re_θ and can be related to the transition correlations by the following expression:

$$Re_\theta = \frac{\max(Re_\mathrm{v})}{2.193} \tag{2.34}$$

γ - Re_θ model formulation allows the simulation of 3D flows originating from different walls. Previously, the correlation-based models were limited to 2D flows considering that they were largely using Re_θ to trigger the onset of transition and the definition of momentum thickness is strictly a 2D concept [4].

2.6.1 Intermittency Transport Equation

The intermittency γ equation is used to trigger the transition locally. It is also coupled with the k - ω SST model since the intermittency function is used to turn on the production term of the turbulent kinetic energy downstream of the transition point in the boundary layer, as can be seen in Eq. 2.64.

$$\frac{\partial(\rho\gamma)}{\partial t} + \nabla \bullet (\rho\bar{\mathbf{u}}\gamma) - \nabla \bullet \left[\left(\mu + \frac{\mu_\mathrm{t}}{\sigma_\mathrm{f}}\right)\nabla\gamma\right] = P_\gamma - E_\gamma\,, \tag{2.35}$$

where P_γ is the transition source term, E_γ is the transition destruction (or relaminarization) term and σ_f a model constant. The transition source term P_γ is designed to be equal to 0 in the laminar boundary layer, upstream of the transition onset location, and become active downstream of the transition onset location [8]. P_γ is defined as follows:

$$P_\gamma = F_{\mathrm{length}} c_{\mathrm{a1}} \rho S (\gamma F_{\mathrm{onset}})^{0.5} (1 - c_{\mathrm{e1}} \gamma) \ , \tag{2.36}$$

where F_{length} is a function which controls the length of the transition region, F_{onset} is a function which controls the transition onset location and S is the absolute value of the strain rate tensor (Eq. 2.25):

$$S = \sqrt{2\,\mathbf{S}\,\mathbf{S}} \,, \qquad \mathbf{S} = \frac{1}{2}\left(\nabla\overline{\mathbf{u}} + \nabla\overline{\mathbf{u}}^{\mathrm{T}}\right) \ ,$$

while c_{a1} and c_{e1} are model constants (Table 2.2). F_{length} is defined by:

$$F_{\mathrm{length}} = F_{\mathrm{length1}} \left(1 - F_{\mathrm{sublayer}}\right) + 40.0 \cdot F_{\mathrm{sublayer}} \ , \tag{2.37}$$

$$F_{\mathrm{sublayer}} = e^{-\left(\frac{R_\omega}{0.4}\right)^2} \ , \tag{2.38}$$

$$R_\omega = \frac{y^2 \omega}{500 \nu} \ , \tag{2.39}$$

where F_{length1} is determined from the following correlation:

$$F_{\mathrm{length1}} = \begin{cases} \left[39.8189 + \left(-119.270 \cdot 10^{-4}\right) \widetilde{Re}_{\theta\mathrm{t}} + \left(-132.567 \cdot 10^{-6}\right) \widetilde{Re}_{\theta\mathrm{t}}^2\right] & \Bigg| \quad \widetilde{Re}_{\theta\mathrm{t}} < 400, \\ \left[263.404 + (-123.939 \cdot 10^{-2}) \widetilde{Re}_{\theta\mathrm{t}} + (194.548 \cdot 10^{-5}) \widetilde{Re}_{\theta\mathrm{t}}^2 + (-101.695 \cdot 10^{-8}) \widetilde{Re}_{\theta\mathrm{t}}^3\right] & \Bigg| \quad 400 \leq \widetilde{Re}_{\theta\mathrm{t}} < 596, \\ \left[0.5 - (\widetilde{Re}_{\theta\mathrm{t}} - 596.0) \cdot 3.0 \cdot 10^{-4}\right] & \Bigg| \quad 596 \leq \widetilde{Re}_{\theta\mathrm{t}} < 1200, \\ [0.3188] & \Bigg| \quad 1200 \leq \widetilde{Re}_{\theta\mathrm{t}}. \end{cases} \tag{2.40}$$

Here $\widetilde{Re}_{\theta\mathrm{t}}$ represents the local transition onset momentum thickness Reynolds number that is obtained from its transport equation 2.48. This correlation is based on "*a significant amount of numerical experimentation whereby a series of flat plate experiments were reproduced and a curve fitting program was used to develop a correlation that resulted in the correct prediction of the transition length as compared to experimental data*" [2].

F_{onset} is used to activate the source term P_γ (Eq. 2.36) in order to trigger the production of intermittency. In the laminar boundary layer F_{onset} is equal to 0; however it switches rapidly to 1 downstream of the transition onset location. F_{onset} is defined as follows:

$$F_{\mathrm{onset}} = \max\left(F_{\mathrm{onset2}} - F_{\mathrm{onset3}}, 0\right) \ , \tag{2.41}$$

$$F_{\mathrm{onset3}} = \max\left[1 - \left(\frac{k}{2.5 \nu \omega}\right)^3, 0\right] \ , \tag{2.42}$$

$$F_{\mathrm{onset2}} = \min\left[\max\left(F_{\mathrm{onset1}}, F^4_{\mathrm{onset1}}\right), 2.0\right] \ , \tag{2.43}$$

$$F_{\mathrm{onset1}} = \frac{Re_{\mathrm{v}}}{2.193 \cdot Re_{\theta\mathrm{c}}} \ , \tag{2.44}$$

where Re_{v} is the strain-rate Reynolds number (Eq. 2.32) and $Re_{\theta\mathrm{c}}$ is the critical Reynolds number which represents the point where the intermittency first starts to increase in the boundary layer.

$Re_{\theta\mathrm{c}}$ is defined by the following correlation:

$$Re_{\theta\mathrm{c}} = \begin{cases} \Big[\widetilde{Re}_{\theta\mathrm{t}} - \Big(396.035 \cdot 10^{-2} + \left(-120.656 \cdot 10^{-4}\right) \widetilde{Re}_{\theta\mathrm{t}} + \left(868.230 \cdot 10^{-6}\right) \widetilde{Re}^{2}_{\theta\mathrm{t}} \\ \qquad + \left(-696.506 \cdot 10^{-9}\right) \widetilde{Re}^{3}_{\theta\mathrm{t}} + \left(174.105 \cdot 10^{-12}\right) \widetilde{Re}^{4}_{\theta\mathrm{t}}\Big)\Big] & \Big| \ \widetilde{Re}_{\theta\mathrm{t}} \leq 1870 \ , \\ \Big[\widetilde{Re}_{\theta\mathrm{t}} - \Big(593.11 + \Big(\widetilde{Re}_{\theta\mathrm{t}} - 1870.0\Big) \cdot 0.482\Big)\Big] & \Big| \ \widetilde{Re}_{\theta\mathrm{t}} > 1870 \ . \end{cases} \tag{2.45}$$

According to Langtry, "*this correlation is determined based on a series of numerical experiments on a flat plate where the critical Reynolds number was varied along with the freestream turbulence intensity and the subsequent transition Reynolds number was measured based on the most upstream location where the skin friction started to increase*" [2].

The destruction/relaminarization term E_γ acts like a sink term ensuring that the intermittency remains close to 0 in the laminar boundary layer, also it enables predicting relaminarisation as it can enable the intermittency to return to 0 [4]. E_γ is defined as follows:

$$E_\gamma = c_{\mathrm{a2}} \rho \Omega \gamma F_{\mathrm{turb}} \left(c_{\mathrm{e2}} \gamma - 1\right) \ , \tag{2.46}$$

where Ω is the absolute value of the vorticity tensor and F_{turb} is a function used to disable E_γ (Eq 2.46) in the fully turbulent regime, while c_{a2} and c_{a2} are model constants (Table 2.2). The absolute value of the vorticity tensor Ω is defined by:

$$\Omega = \sqrt{2 \, \mathbf{\Omega} \, \mathbf{\Omega}} \ , \qquad \mathbf{\Omega} = \frac{1}{2}\left(\nabla \bar{\mathbf{u}} - \nabla \bar{\mathbf{u}}^{\mathrm{T}}\right) \ , \tag{2.47}$$

and F_{turb} is defined by:

$$F_{\mathrm{turb}} = e^{-\left(\frac{k}{4\nu\omega}\right)^4} \ . \tag{2.48}$$

The boundary conditions for intermittency are $\gamma = 1$ at inlets and zero normal flux $\frac{\partial \gamma}{\partial n} = 0$ at a wall.

σ_f	c_a1	c_e1	c_a2	c_e2
1.0	2.0	1	0.06	50

Table 2.2: Constants of the γ transport equation, γ - Re_θ transition model [4]

2.6.2 Local Transition Onset Momentum Thickness Reynolds Number Transport Equation

The transport equation for local transition onset momentum thickness Reynolds number $\widetilde{Re}_{\theta\mathrm{t}}$ reads:

$$\frac{\partial\left(\rho\widetilde{Re}_{\theta\mathrm{t}}\right)}{\partial t}+\nabla\bullet(\rho\overline{\mathbf{u}}\widetilde{Re}_{\theta\mathrm{t}})-\nabla\left[\sigma_{\theta\mathrm{t}}(\mu+\mu_\mathrm{t})\nabla\bullet\widetilde{Re}_{\theta\mathrm{t}}\right]=P_{\theta\mathrm{t}}\ , \tag{2.49}$$

where $P_{\theta\mathrm{t}}$ is the source term and $\sigma_{\theta\mathrm{t}}$ is a model constant (Tab 2.3). $P_{\theta\mathrm{t}}$ is defined as follows:

$$P_{\theta\mathrm{t}}=c_{\theta\mathrm{t}}\frac{\rho}{t}\left(Re_{\theta\mathrm{t}}^{\mathrm{eq}}-\widetilde{Re}_{\theta\mathrm{t}}\right)(1.0-F_{\theta\mathrm{t}})\ , \tag{2.50}$$

$$t=\frac{500\nu}{U^2}\ , \tag{2.51}$$

where t is a time scale present for dimensional reasons, $Re_{\theta\mathrm{t}}^{\mathrm{eq}}$ is the equilibrium value of the transition onset momentum thickness Reynolds number and $F_{\theta\mathrm{t}}$ is a blending function. The source term (Eq 2.50) is designed so that, outside of the boundary layer, $Re_{\theta\mathrm{t}}$ is "attracted" to the value of $Re_{\theta\mathrm{t}}^{\mathrm{eq}}$. At the edge of the boundary layer $Re_{\theta\mathrm{t}}$ is physically accurate and from there it diffuses into the boundary layer where the aforementioned "attraction" is suppressed by the blending function $F_{\theta\mathrm{t}}$ [22]. $Re_{\theta\mathrm{t}}^{\mathrm{eq}}$ is determined from the following empirical correlations:

$$Re_{\theta\mathrm{t}}^{\mathrm{eq}}=\begin{cases}\left(1173.51-589.428Tu+\frac{0.2196}{Tu^2}\right)F(\lambda_\theta) & \Big|\ Tu\leq1.3\%,\\ 331.50\,(Tu-0.5658)^{-0.671}F(\lambda_\theta) & \Big|\ Tu>1.3\%,\end{cases} \tag{2.52}$$

$$F(\lambda_\theta)=\begin{cases}1+\left(12.986\lambda_\theta+123.66\lambda_\theta^2+405.689\lambda_\theta^3\right)e^{-\left(\frac{Tu}{1.5}\right)^{1.5}} & \Big|\ \lambda_\theta\leq0,\\ 1+0.275\left[1-e^{(-35\lambda_\theta)}\right]e^{-\frac{Tu}{0.5}} & \Big|\ \lambda_\theta>0,\end{cases} \tag{2.53}$$

where Tu is turbulence intensity:

$$Tu=100\frac{\sqrt{2k/3}}{U}\ , \tag{2.54}$$

and λ_θ is pressure gradient parameter:

$$\lambda_\theta = \frac{\theta_\mathrm{t}^2}{\nu}\frac{\mathrm{d}U}{\mathrm{d}s} \, , \tag{2.55}$$

where θ_t is transition momentum thickness and $\mathrm{d}U/\mathrm{d}s$ is the acceleration along the stream-wise flow direction. Derivative of velocity along the streamline $\mathrm{d}U/\mathrm{d}s$ can be computed as follows:

$$U = \sqrt{u^2 + v^2 + w^2} \, , \tag{2.56}$$

$$\frac{\mathrm{d}U}{\mathrm{d}s} = \left(\frac{u}{U}\frac{\mathrm{d}U}{\mathrm{d}x} + \frac{v}{U}\frac{\mathrm{d}U}{\mathrm{d}y} + \frac{w}{U}\frac{\mathrm{d}U}{\mathrm{d}z} \right) \, . \tag{2.57}$$

Moreover, $Re_{\theta\mathrm{t}}^{\mathrm{eq}}$ can also be expressed as a function of θ_t:

$$Re_{\theta\mathrm{t}}^{\mathrm{eq}} = \frac{U\theta_\mathrm{t}}{\nu} \, . \tag{2.58}$$

Transition momentum thickness θ_t appears on both sides of Eq 2.52, through $Re_{\theta\mathrm{t}}^{\mathrm{eq}}$ on the left hand side and through θ_t on the right hand side. Consequently, Eq. 2.52 is solved by iterating on the value of θ_t. For the purposes of numerical robustness the empirical correlation, turbulence intensity and acceleration parameters should be limited as follows [4]:

$$Re_{\theta\mathrm{t}}^{\mathrm{eq}} \geq 20, \qquad Tu \geq 0.027\%, \qquad -0.1 \leq \lambda_\theta \leq 0.1.$$

$F_{\theta\mathrm{t}}$ is the blending function that switches the source term (Eq. 2.50) off in the boundary layer and allows the transported scalar $\widetilde{Re}_{\theta\mathrm{t}}$ to diffuse in the boundary layer from the free - stream. In the free-stream $F_{\theta\mathrm{t}}$ is equal to 0 and in the boundary layer it is equal to 1. It is defined by:

$$F_{\theta\mathrm{t}} = \min\left\{ \max\left[F_{\mathrm{wake}} \cdot e^{-\left(\frac{y}{\delta}\right)^4} \, , \, 1.0 - \left(\frac{\gamma - \frac{1}{c_{\mathrm{e}2}}}{1.0 - \frac{1}{c_{\mathrm{e}2}}} \right)^2 \right] \, , \, 1.0 \right\} \, , \tag{2.59}$$

where δ is boundary layer thickness and F_{wake} is a function which ensures that the blending function $F_{\theta\mathrm{t}}$ is not active in the wake regions downstream of the airfoil . They are defined as follows:

$$\delta = \frac{375\,\Omega\,\nu\,\widetilde{Re}_{\theta\mathrm{t}}\,y}{U^2} \, , \tag{2.60}$$

$$F_{\text{wake}} = e^{-\left(Re_{\omega}\cdot 10^{-5}\right)^2} \ , \qquad Re_{\omega} = \frac{\omega y^2}{\nu} \ . \tag{2.61}$$

$\sigma_{\theta\text{t}}$	$c_{\theta\text{t}}$	c_{e2}
2.0	0.03	50

Table 2.3: Constants of the $\widetilde{Re}_{\theta\text{t}}$ transport equation, γ - Re_{θ} transition model [4]

The boundary conditions for $\widetilde{Re}_{\theta\text{t}}$ are:

$$\widetilde{Re}_{\theta\text{t}} = \begin{cases} \left(1173.51 - 589.428 Tu + \frac{0.2196}{Tu^2}\right) & \Big| \ Tu_{\infty} \leq 1.3\% \\ 331.50\left(Tu - 0.5658\right)^{-0.671} & \Big| \ Tu_{\infty} > 1.3\% \end{cases} \tag{2.62}$$

at inlets and zero normal flux $\frac{\partial \widetilde{Re}_{\theta\text{t}}}{\partial n} = 0$ at a wall.

2.6.3 Turbulent Kinetic Energy Transport Equation

The transitional γ - Re_{θ} turbulence model interacts with the k - ω SST turbulence model through the turbulent kinetic energy k transport equation as follows:

$$\frac{\partial(\rho k)}{\partial t} + \nabla \bullet (\rho \overline{\mathbf{u}} k) - \nabla \bullet \left[(\mu + \sigma_{\text{k}} \mu_{\text{t}}) \nabla k\right] = \hat{P}_k - \hat{D}_k \ , \tag{2.63}$$

$$\hat{P}_{\text{k}} = \gamma_{\text{eff}} P_{\text{k}} \ , \qquad \hat{D}_k = \min\left[\max\left(\gamma_{\text{eff}}\ , 0.1\right), 1.0\right] \beta^* \rho k \omega \tag{2.64}$$

where $\hat{P}_k$ and $\hat{D}_k$ are modified production and destruction terms from the turbulent kinetic energy equation of the k - ω SST model. Effective intermittency γ_{eff} is used to turn on the production term of the turbulent kinetic energy equation downstream of the transition point. Effective intermittency is defined by:

$$\gamma_{\text{eff}} = \max\left(\gamma, \gamma_{\text{sep}}\right) \ , \tag{2.65}$$

where γ_{sep} is the separation intermittency number, defined as follows:

$$\gamma_{\text{sep}} = \min\left\{ s_1 \max\left[0, \left(\frac{Re_{\text{v}}}{3.235 Re_{\theta c}}\right) - 1\right] F_{reattach}, 2\right\} F_{\theta t} \ , \tag{2.66}$$

$$s_1 = 2 \ , \qquad F_{reattach} = e^{-\left(\frac{k}{20\nu\omega}\right)^4} \ . \tag{2.67}$$

The separation induced transition occurs when γ_{sep} exceeds the value of 1 and causes a large production of k which in turn results in reattachment of the flow [4].

2.6.4 Turbulent Dissipation Rate Transport Equation

The turbulent dissipation rate ω transport equation (Eq. 2.21) remains largely the same. The only change is in the blending function responsible for switching between the k - ω and the k - ε model.

To prevent the switching in the laminar boundary layer F_1 is modified to always be equal to 1 in the laminar boundary layer [8].

$$F_1 = \max\left(F_{1\text{orig}}, F_3\right) \ , \tag{2.68}$$

$$F_3 = e^{-\left(\frac{R_y}{120}\right)^8}, \qquad R_y = \frac{y\sqrt{k}}{\nu} \ , \tag{2.69}$$

where $F_{1\text{orig}}$ is the original blending function from the turbulent dissipation rate transport equation (Eq. 2.21) of the k - ω SST turbulence model.

2.7 Closure

This chapter served as an overview of the implemented mathematical model. The General Scalar Transport Equation, governing equations of fluid flow and used turbulence models were defined as well as their connections. Following chapter shall introduce the numerical model, specifically the Finite Volume Method (FVM), and will serve as an overview of the theoretical background required to understand the implementation of the model.

3 | Numerical Model

3.1 Introduction

The previous chapter served as an an overview of the mathematical model, setting the foundation for the numerical model. The following chapter introduces the numerical model and serves as an overview of the theoretical background required to understand the implementation of the Finite Volume Method.

3.2 The Finite Volume Method

Numerical method used in this thesis for solving the governing equations of fluid flow is the Finite Volume Method (FVM). With the use of the FVM a set of partial differential equations (PDE) is tansformed into a system of linear algebraic equations. This is achieved by temporal and spatial discretisation. Time is discretised as a finite series of time-steps in which the values of observed variables are calculated, however, for the case of steady state simulations time is not discretised. Spatial domain is discretised as a numerical mesh consisting of a finite number of cells (control volumes, Figure 3.1) that fill the domain without overalp between the cells.

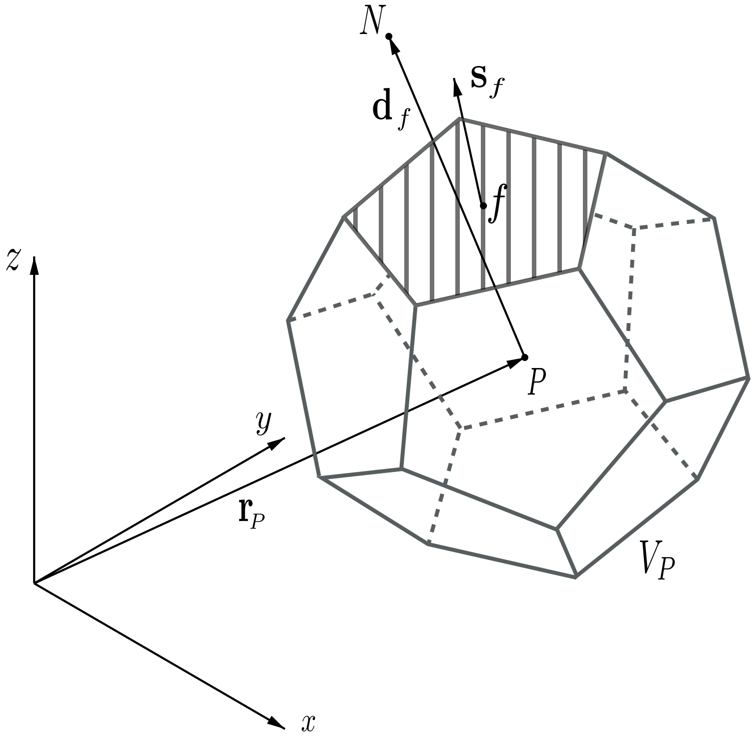

Figure 3.1: A representation of a cell, given by a convex polyhedron [3].

Every cell (Figure 3.1) is defined by the cell centroid P and the centroid position vector r_P in relation to the origin of the global coordinate system. For the observed cell (parent cell) there is one neighboring cell across each of its faces. Centroid N of any neighbouring cell is connected to the centroid P of the parent cell by a delta vector $\mathbf{d}_f = \overline{PN}$ [19]. Centroid of the cell is the main computational point in which solutions to the discretised equations are stored and its defined as:

$$\int_{V_P} (x - x_P)\mathrm{d}V = 0 \; . \tag{3.1}$$

For a selected cell face a surface normal vector $\mathbf{s}_f$, stemming from the face center f, is defined with a magnitude equal to the are of the selected face S_f. The face center f is defined in the same manner as the cell centroid:

$$\int_{S_f} (x - x_f)\mathrm{d}S = 0 \; . \tag{3.2}$$

Since the faces of polyhedral cells are usually not flat surfaces, the surface normal vector $\mathbf{s}_f$ must be calculated from the following integral:

$$\mathbf{s}_f = \int_{S_f} \mathbf{n}\mathrm{d}S \; . \tag{3.3}$$

There are two types of cell faces in the numerical mesh: internal face positioned between two cells and a boundary face belongs to only one cell and points out of the computational domain. The face center of the boundary face is used to store boundary data.

3.2.1 Boundary Conditions

Boundary conditions are used to classify the boundary of the computational domain and to prescribe the behaviour of the general property ϕ at the boundary.

Numerical Boundary Conditions

Numerical boundary conditions are used to prescribe the behaviour of the general property ϕ at the boundary. Most common are:

- *Dirichlet boundary condition* – prescribes a fixed value of ϕ at the boundary

$$\phi = constant \; , \tag{3.4}$$

- *Von Neumann boundary condition* – prescribes a fixed gradient (or flux) of ϕ at the boundary

$$\frac{\partial \phi}{\partial n} = q_b \,, \tag{3.5}$$

- *Robin boundary condition* – often called mixed boundary condition, prescribes the linear combination of the Dirichlet and von Neumann condition at the boundary.

Physical Boundary Conditions

Physical boundary conditions are used to classify the boundary and are often represented by a set of numerical boundary conditions for each unknown variable. Most common are:

- *Inlet boundary* – velocity is usually prescribed by the Dirichlet (Eq. 3.4), while pressure is usually prescribed by the von Neumann (Eq. 3.5) with the gradient set to a value of 0;
- *Outlet boundary* – velocity is usually prescribed by the von Neumann (Eq. 3.5) with the gradient set to a value of 0, while pressure is usually prescribed by the Dirichlet (Eq. 3.4);
- *Impermeable no-slip wall boundary* – velocity is usually prescribed by the Dirichlet (Eq. 3.4), while pressure is usually prescribed by the von Neumann (Eq. 3.5) with the gradient set to a value of 0;
- *Symmetry Plane* – implies that the component of the gradient normal to the boundary is equal to a value of 0, while components parallel to the boundary are projected to the boundary face from the interior of the computational domain [5].

3.2.2 Discretisation of the General Scalar Transport Equation

The first step in the discretisation of the General Scalar Transport Equation is obtaining its integral form.

$$\int_V \frac{\partial \phi}{\partial t} \mathrm{d}V + \oint_S \phi \,(\mathbf{n} \bullet \mathbf{u}) \,\mathrm{d}S - \oint_S \gamma (\mathbf{n} \bullet \nabla \phi) \,\mathrm{d}S = \int_V Q_v \mathrm{d}V \,. \tag{3.6}$$

Considering that in this thesis conducted simulations were steady-state temporal derivative term is omitted from Eq. 3.6 and won't be further discussed.

Full list of the discretisation can be found in the Appendix A.

Discretisation of the Convection Term

Surface integral of the convection term (from Eq. 3.6) can be expressed as a sum of face integrals:

$$\oint_S \phi\,(\mathbf{n}\bullet\mathbf{u}) = \sum_f \int_S \phi_f(\mathbf{s}_f\bullet\mathbf{u}_f) = \sum_{\mathrm{f}} F\phi_f \ , \tag{3.7}$$

where ϕ_f is the value of the general property ϕ at the face of the cell and F is the flux that can be expressed as:

$$F = \mathbf{s}_f\bullet\mathbf{u}_f \ . \tag{3.8}$$

The value of ϕ_f needs to be evaluated from values ϕ_P and ϕ_N located at the centroids of parent and neighbouring cells, this is achieved by using one of the various interpolation schemes (e.g. central differencing, upwind differencing).

Discretisation of the Diffusion Term

Discretisation of the diffusion term is conducted in the same manner as the discretisation of the convection term.

$$\oint_S \gamma(\mathbf{n}\bullet\nabla\phi)\,\mathrm{d}S = \sum_f \int_S \gamma(\mathbf{n}\bullet\nabla\phi)\,\mathrm{d}S = \sum_{\mathrm{f}} \gamma\,\mathbf{s}_f\bullet(\nabla\phi)_f \ , \tag{3.9}$$

where $\mathbf{s}_f\bullet(\nabla\phi)_f$ represents a face-normal gradient that can be expressed as the difference of ϕ across the face:

$$\mathbf{s}_f\bullet(\nabla\phi)_f = |\mathbf{s}_f|\frac{\phi_N-\phi_P}{|\mathbf{d}_f|} \ . \tag{3.10}$$

Eq. 3.10 is valid for orthogonal meshes whereas in case of large non-orthogonality correction terms must be applied. [24]

Discretisation of the Source/Sink Term

Sources and sinks describe local effects and can be a function of space and time, solution itself or any other variable. Discretisation of the source/sink term is conducted as follows:

$$\int_V Q_v dV = Q_v V_P \ . \tag{3.11}$$

To promote stability and boundedness, linearisation of Q_v with respect to ϕ is commonly performed [19].

3.2.3 Linear System of Equations

After the discretisation of the General Scalar Transport Equation a following linear equation is solved for each cell :

$$a_P \phi_P + \sum_N a_N \phi_N = b \ . \tag{3.12}$$

When observing the whole domain a system of linear equations is created containing Eq. 3.12 of each cell. The system of linear equations is generally written in the following matrix form:

$$\mathbf{Ax} = \mathbf{b} \ , \tag{3.13}$$

where $\mathbf{A}$ is a square $N \times N$ matrix, N being the number of cells in the domain. The matrix $\mathbf{A}$ contains diagonal coefficients a_P and off-diagonal coefficients a_N. Additionally, ϕ_P represents the value of the general property ϕ at the computational point of the parent cell (cell centroid P), while ϕ_N represents the value of ϕ at the computational point of the neighbouring cells (cell centroid N). Every time ϕ_P depends on itself a contribution is added into a_P and every time ϕ_N depends on itself a contribution is added into a_N. Vector $\mathbf{x}$ contains values of ϕ_P for all cells in the domain, while vector $\mathbf{b}$ contains contributions of sources/sinks and boundary conditions [19].

3.2.4 Implicitly Coupled Pressure-Velocity System

When observing the continuity (Eq. 2.10):

$$\nabla \bullet \mathbf{u} = 0 \ ,$$

and the linear momentum equation (Eq. 2.14):

$$\frac{\partial \mathbf{u}}{\partial t} + \nabla \bullet (\mathbf{uu}) - \nabla \bullet (\nu \nabla \mathbf{u}) = -\frac{\nabla p}{\rho} \ ,$$

the issue which arises is the mutual influence of velocity and pressure. The equation set consist of one scalar equation (continuity equation) and one vector equation (momentum equation). Considering that the pressure does not appear in the continuity equation (Eq. 2.10) and in the momentum equation (Eq. 2.14) it appears only as a gradient, the velocity is affected by the pressure differences instead of the absolute value of pressure. In order to solve the pressure-velocity system an equation for pressure is derived from the momentum equation. Finally, calculated values of pressure are used to enforce the continuity of the velocity field [5].

In this thesis the pressure-velocity system is solved using the implicitly coupled pressure-velocity algorithm **pUCoupledFoam** [16] in **foam-extend-4.1** [12–14] environment. It is worth noting that there was an attempt to use segregated SIMPLE (Semi-Implicit Method for Pressure Linked Equations) algorithm [25] for the simulations of the transitional flow. SIMPLE algorithm is an iterative procedure used for solving steady-state pressure-velocity systems, it was developed by Suhas Patankar and his professor Brian Spalding in 1972. By using the SIMPLE algorithm equations are firstly decoupled, after which they are solved sequentially until the convergence criterion is reached. However, attempts to simulate transitional flow using the SIMPLE algorithm proved to be unsuccessful, as the simulations were too slow and unstable because of the decoupling error of the SIMPLE algorithm. This in turn led to the use of the the implicitly coupled pressure-velocity algorithm **pUCoupledFoam**.

As the conducted simulation are steady-state, temporal derivative terms are omitted from the equations and won't be further discussed.

The continuity and the linear momentum equations can expressed in block form as follows:

$$\begin{bmatrix} \mathbf{A_u} & \nabla(.) \\ \nabla \bullet (.) & 0 \end{bmatrix} \begin{bmatrix} \mathbf{u} \\ p \end{bmatrix} = \begin{bmatrix} 0 \\ 0 \end{bmatrix} , \tag{3.14}$$

where $\mathbf{A_u}$ is the linear combination of diffusion and linearised convection. The system defined in Eq. 3.14 corresponds both to the differential and discretised form of equations but it is assumed that the system is discretised. The block system has got a zero block at location $[2,2]$ indicating a saddle point problem [26]. Regular saddle point solver techniques such as Elman preconditioning [26] have proven cumbersome and inefficient and an alternative matrix based preconditioned shall be described below. Let us first consider the assembly and solution of the block-matrix for the p-U systems.

Solution of the Block Matrix via Pressure-Based Preconditioning

If the general block matrix $\mathbf{M}$ is defined as:

$$\mathbf{M}_{(m+q)\times(m+q)} = \begin{bmatrix} \mathbf{A}_{m\times m} & \mathbf{B}_{m\times q} \\ \mathbf{C}_{q\times m} & \mathbf{C}_{q\times q} \end{bmatrix} , \tag{3.15}$$

following linear system defined by the block matrix $\mathbf{M}$ can be obtained:

$$\begin{bmatrix} \mathbf{A}_{m\times m} & \mathbf{B}_{m\times q} \\ \mathbf{C}_{q\times m} & \mathbf{C}_{q\times q} \end{bmatrix} \begin{bmatrix} \mathbf{x}_m \\ \mathbf{y}_q \end{bmatrix} = \begin{bmatrix} \mathbf{a}_m \\ \mathbf{b}_q \end{bmatrix} . \tag{3.16}$$

The linear system in its expanded form reads:

$$\mathbf{A}\mathbf{x} + \mathbf{B}\mathbf{y} = \mathbf{a} , \tag{3.17}$$

$$\mathbf{C}\mathbf{x} + \mathbf{D}\mathbf{y} = \mathbf{b} . \tag{3.18}$$

By assuming that **A** is invertible **x** can be expressed from Eq. 3.17 as:

$$\mathbf{x} = \mathbf{A}^{-1}\mathbf{a} - \mathbf{A}^{-1}\mathbf{B}\mathbf{y} , \tag{3.19}$$

and substituted into Eq. 3.18 to obtain:

$$\mathbf{C}\left(\mathbf{A}^{-1}\mathbf{a} - \mathbf{A}^{-1}\mathbf{B}\mathbf{y}\right) + \mathbf{D}\mathbf{y} = \mathbf{b} . \tag{3.20}$$

When rearranged, Eq. 3.20 can be expressed as:

$$\underbrace{\left(\mathbf{D} - \mathbf{C}\mathbf{A}^{-1}\mathbf{B}\right)}_{\text{Schur complement}} \mathbf{y} = \mathbf{b} - \mathbf{C}\mathbf{A}^{-1}\mathbf{a} . \tag{3.21}$$

By comparing block systems from Eq. 3.14 and 3.16 following relations can be identified:

$$\mathbf{A} = \mathbf{A_u} , \qquad \mathbf{B} = \nabla(.) , \qquad \mathbf{C} = \nabla \bullet (.) , \qquad \mathbf{D} = 0 ,$$
$$\mathbf{x} = \mathbf{u} , \qquad \mathbf{y} = p , \qquad \mathbf{a} = 0 .$$

By inserting the appropriate terms into Eq. 3.21 the pressure equation can be obtained:

$$\underbrace{\nabla \bullet \left(\mathbf{A_u}^{-1} \nabla p\right)}_{\text{Schur complement}} = 0 . \tag{3.22}$$

Pressure equation (Eq. 3.22) is a Laplacian with the inverse of the momentum matrix $\mathbf{A_u}^{-1}$ acting as a diffusion coefficient. Even though $\mathbf{A_u}$ is a sparse matrix, its inverse $\mathbf{A_u}^{-1}$ is likely to be dense, which makes it too expensive to in both memory and CPU requirements [19].

To remedy this issue matrix $\mathbf{A_u}$ from the block system Eq. 3.14 can be decomposed into the diagonal $\mathbf{D_u}$ and off-diagonal $\mathbf{E_u}$ matrices as follows:

$$\mathbf{A_u} = \mathbf{D_u} + \mathbf{E_u} \ , \tag{3.23}$$

$$\begin{bmatrix} \mathbf{D_u} & \nabla(.) \\ \nabla \bullet (.) & 0 \end{bmatrix} \begin{bmatrix} \mathbf{u} \\ p \end{bmatrix} = \begin{bmatrix} -(\mathbf{E_u})\mathbf{u} \\ 0 \end{bmatrix} . \tag{3.24}$$

The diagonal matrix $\mathbf{D_u}$ is easy to invert while preserving the sparseness of the matrix. Consequentially, the diagonal matrix $\mathbf{D_u}$ is treated implicitly, i.e. it remains in the coefficient matrix, while the off-diagonal matrix is treated explicitly, i.e. it is moved into the right hand side vector [5]. If the components of the block system Eq. 3.24 are inserted into Eq. 3.21 the pressure equation can be derived as follows:

$$\nabla \bullet \left(\mathbf{D_u}^{-1} \nabla p\right) = \nabla \bullet \left(\mathbf{D_u}^{-1} \mathbf{E_u} \mathbf{u}\right) . \tag{3.25}$$

The pressure equation (Eq. 3.25) is a Poisson equation with the inverse of the diagonal matrix $\mathbf{D_u}^{-1}$ acting as a diffusivity on the left hand side and the divergence of the velocity field on the right hand side. To derive an implicitly coupled system, firstly, the momentum equation needs to be obtained from Eq. 3.24:

$$\mathbf{E_u u} = -\mathbf{D_u u} - \nabla p \ . \tag{3.26}$$

Then, substituting Eq. 3.26 into the pressure equation (Eq. 3.25) yields:

$$\nabla \bullet \mathbf{u} - \nabla \bullet \left(\mathbf{D_u}^{-1} \nabla p\right) = -\nabla \bullet \left(\mathbf{D_u}^{-1} \nabla p\right) \ . \tag{3.27}$$

As shown, Eq. 3.27 contains two identical Laplacians of the pressure field which cancel out each other. This is corrected by the implementation of the Rhie-Chow correction, so that the pressure equation reads:

$$\nabla \bullet \mathbf{u} - \nabla \bullet \left(\mathbf{D_u}^{-1} \nabla p\right) = -\nabla \bullet \left(\overline{\mathbf{D_u}^{-1} \nabla p}\right) \ , \tag{3.28}$$

where the explicit term $-\nabla \bullet \left(\overline{\mathbf{D_u}^{-1} \nabla p}\right)$ indicates interpolation from cell centroids to faces in accordance with the Rhie-Chow correction [27].

Preconditioning of the p-U Saddle-Point System

If the the momentum equation (Eq. 3.26) and the pressure equation (Eq. 3.28) are combined, the implicitly coupled system reads:

$$\begin{bmatrix} \mathbf{D_u} + \mathbf{E_u} & \nabla(.) \\ \nabla \bullet (.) & -\nabla \bullet \left(\mathbf{D_u}^{-1} \nabla\right) \end{bmatrix} \begin{bmatrix} \mathbf{u} \\ p \end{bmatrix} = \begin{bmatrix} 0 \\ -\nabla \bullet \left(\overline{\mathbf{D_u}^{-1} \nabla p}\right) \end{bmatrix} . \tag{3.29}$$

The above operation effectively preconditions the block system (Eq. 3.14) and allows us to use conventional iterative linear equation solvers, albeit in the block format.

Rhie-Chow Correction and Pressure Preconditioning

When calculating the pressure gradients for cell i in the momentum equation, values of pressure p_i cancel out due to the discretisation procedure, i.e. linear interpolation from cell centroids. Considering that the pressure equation (Eq. 3.25) is derived by expressing the velocity from the momentum equation and inserting it into the continuity equation, connection between pressure values in the neighbouring cells is lost in it as well. As a result, oscillations appear in the solution of the pressure field.

Rhie-Chow interpolation provides a link between the values of pressure in the neighbouring cells and smooths out the pressure field. The correction is applied when calculating the velocity at the face:

$$\mathbf{u}_f = \overline{\mathbf{u}_f} - \frac{1}{a_p}(\nabla p_f - \overline{\nabla p_f}) , \tag{3.30}$$

where overline indicates interpolaton from cell centroids onto faces [5]. This can be seen on the example of the pressure equation discretisation where the value of velocity at the face is expressed according to Eq. 3.30 to account for the influence of the pressure field:

$$\nabla \bullet \mathbf{u} = \sum_f \mathbf{s}_f \bullet \mathbf{u}_f = \sum_f \mathbf{s}_f \bullet \left[\overline{\mathbf{u}_f} - \frac{1}{a_p}(\nabla p_f - \overline{\nabla p_f})\right] = 0 . \tag{3.31}$$

This discretised form of the pressure equation (Eq. 3.31) is equivalent to the form presented in Eq. 3.28.

Solution Procedure for the Implicitly Coupled Pressure-Velocity Systems

The solution procedure of the implicitly coupled pressure-velocity systems consist of the following steps:

1. In a non-linear iteration k the block system containing the linearised momentum equation and the continuity equation including the Rhie-Chow correction is assembled as follows:

$$\begin{bmatrix} \mathbf{A_u} & \nabla(.) \\ \nabla \bullet (.) & -\nabla \bullet \left(\mathbf{D_u}^{-1}\nabla\right) \end{bmatrix} \begin{bmatrix} \mathbf{u} \\ p \end{bmatrix} = \begin{bmatrix} 0 \\ -\nabla \bullet \left(\overline{\mathbf{D_u}^{-1}\nabla p^{(k-1)}}\right) \end{bmatrix} \tag{3.32}$$

   As denoted by the superscript $(k-1)$, the explicit Rhie-Chow correction term contains the values of the pressure field from the previous iteration. The momentum equation may be implicitly under-relaxed for stability, however, the pressure equation (Eq. 3.31) requires no under-relaxation since it is linear and the effects of the pressure gradient are implicitly included in the momentum equation. The system is then solved to obtain the values of pressure $p^{(k)}$ and velocity $\mathbf{u}^{(k)}$. [5]

2. After the solution of the block system (Eq. 3.32) has been obtained, flux through the face $F^{(k)}$ can be reconstructed as:

$$F^{(k)} = \sum_f \mathbf{s}_f \bullet \left[\overline{\mathbf{u}_f}^{(k)} - \frac{1}{\overline{a_p}}\left(\nabla p_f^{(k)} - \overline{\nabla p_f}^{(k-1)}\right)\right] = 0 \tag{3.33}$$

   The flux $F^{(k)}$ is used in the convection-diffusion matrix $\mathbf{A_u}$ of the next non-linear iteration.

The non-linear iterative procedure is repeated until the assigned convergence criterion is reached.

3.2.5 Selective Algebraic Multigrid Solver for Block-Matrices

Algebraic Multigrid Solver (AMG) is a linear solver which does not operate on the computational mesh and uses only the information in the coefficient matrix **A** (Eq. 3.13) of the linear system. Even though AMG uses only the information in the coefficient matrix, it is easier to think about multigrid in terms of the computational mesh and for that reason the analogy between mesh and matrix will often be used. In order to explain Block AMG methods a Primary Matrix is introduced (Eq. 3.34). A Primary Matrix is a matrix with scalar elements which represent the block-matrix in some form. It is important that the strength of connection in the block-matrix is well represented by the Primary Matrix and that the signs of matrix elements are taken into consideration. Primary Matrix can be constructed in a several ways and whilst only one of these will be described in this Thesis, more can found in the listed literature [5].

Defining the Primary Matrix

A single unknown variable can be chosen and its connectivity pattern (pattern of matrix elements representing cell-to-cell communication) can be used to define the Primary Matrix. It is appropriate to choose the pressure equation and exclude cross couplings to velocity, as the pressure equation is Laplacian in nature and the discretisation of the Laplacian produces a symmetric positive definite matrix, which is required by AMG.

$$A_{ij}^{\text{block}} = \begin{bmatrix} a_{u_{xi},u_{xj}} & a_{u_{xi},u_{yj}} & a_{u_{xi},u_{zj}} & a_{u_{xi},p_j} \\ a_{u_{yi},u_{xj}} & a_{u_{yi},u_{yj}} & a_{u_{yi},u_{zj}} & a_{u_{yi},p_j} \\ a_{u_{zi},u_{xj}} & a_{u_{zi},u_{yj}} & a_{u_{zi},u_{zj}} & a_{u_{zi},p_j} \\ a_{p_i,u_{xj}} & a_{p_i,u_{yj}} & a_{p_i,u_{zj}} & \color{red}{a_{p_i,p_j}} \end{bmatrix} \rightarrow a_{ij}^{\text{primary}} = a_{p_i,p_j} \ , \tag{3.34}$$

where subscript i indicates parent cell and subscript j indicates neighbouring cells. By choosing the pressure equation and excluding the cross-couplings to velocity, sparsity pattern of the primary matrix becomes the same as the block-matrix, since the pressure equation is defined for each cell. [5]

Coarsening Procedure for the Selective Algebraic Multigrid Solver for

Subsequently to the construction of the Primary Matrix (Eq. 3.34) the coarsening procedure is applied to it. In this thesis only a broad overview of the Selection Algebraic Multigrid (SAMG) coarsening strategy will be given, however, in-depth study of the coarsening strategies (including SAMG) is further explored by Uroić [5]. SAMG achieves coarsening by selecting the representative equations from the fine level matrix, i.e. choosing the representative cells from the fine mesh. For the case of block-matrices, the split into coarse and fine equations is based on the Primary Matrix (Eq. 3.34). The selection of the equations, i.e. cells, depends on the strength of connectivity in the Primary Matrix (Eq. 3.34), i.e. the magnitude of the off-diagonal elements. [5]

After the equations are separated into coarse and fine sets it is necessary to define how the correction on the coarse level will be applied to the fine level. This is done through weighted interpolation so that every fine equation receives a coarse level correction from its coarse influences (neighbours). Interpolation weights are only calculated for the fine level equations not chosen into the coarse subset and they are assembled into the prolongation matrix **P** with dimensions equal to (*number of fine level equations*) × (*number of equations in the coarse subset*). Subsequently, the restriction matrix **R** is constructed. Restriction matrix **R** is used to transfer the residual from fine to coarse level and is equal to the transpose of the prolongation matrix $\mathbf{P}^{\mathrm{T}}$. [5]

Lastly, the coarse level matrix can be calculated as a matrix product of the restriction matrix **R**, fine level matrix $\mathbf{A}^\mathrm{F}$ and prolongation matrix **P**:

$$\mathbf{A}^\mathrm{C} = \mathbf{R}\mathbf{A}^\mathrm{F}\mathbf{P}\ . \tag{3.35}$$

Solution Procedure Selective Algebraic Multigrid Solver

The solution procedure for a single two-level V-cycle of the Selective Algebraic Multigrid solver consists of the following steps:

1. Calculate the approximate solution of the system on the fine level:

   $$\mathbf{A}^\mathrm{F}\mathbf{x}^\mathrm{F} = \mathbf{b}\ , \tag{3.36}$$

   where $\mathbf{A}^\mathrm{F}$ is the coefficient matrix on the fine level, $\mathbf{x}^\mathrm{F}$ is the approximate solution on the fine level and **b** is the right hand side vector.

2. Calculate the fine level residual $\mathbf{r}^\mathrm{F}$ using the obtained approximate solution $\mathbf{x}^\mathrm{F}$:

   $$\mathbf{r}^\mathrm{F} = \mathbf{b} - \mathbf{A}^\mathrm{F}\mathbf{x}^\mathrm{F}\ . \tag{3.37}$$

3. Create a coarse matrix $\mathbf{A}^\mathrm{C}$ (Eq. 3.35):

   $$\mathbf{A}^\mathrm{C} = \mathbf{R}\mathbf{A}^\mathrm{F}\mathbf{P}\ ,$$

   where **R** is the the restriction matrix, $\mathbf{A}^\mathrm{F}$ is the fine matrix and**P** is the prolongation matrix.

4. Transform the residual from the fine level $\mathbf{r}^\mathrm{F}$ to the coarse level $\mathbf{r}^\mathrm{C}$ using the restriction matrix **R**:

   $$\mathbf{r}^\mathrm{C} = \mathbf{R}\mathbf{r}^\mathrm{F}\ . \tag{3.38}$$

5. Solve the correction equation on the coarse level:

   $$\mathbf{A}^\mathrm{C}\mathbf{e}^\mathrm{C} = \mathbf{r}^\mathrm{C}\ , \tag{3.39}$$

   where $\mathbf{e}^\mathrm{C}$ is the coarse level error.

6. Transform the error from the coarse level $\mathbf{e}^{\mathrm{C}}$ to the fine level $\mathbf{e}^{\mathrm{F}}$, using the prolongation matrix $\mathbf{P}$:

$$\mathbf{e}^{\mathrm{F}} = \mathbf{P}\mathbf{e}^{\mathrm{C}} . \tag{3.40}$$

7. Use the fine level error $\mathbf{e}^{\mathrm{F}}$ to correct the solution on the fine level:

$$\mathbf{x}^{\mathrm{F}} = \mathbf{x}^{\mathrm{F}}\mathbf{e}^{\mathrm{F}} . \tag{3.41}$$

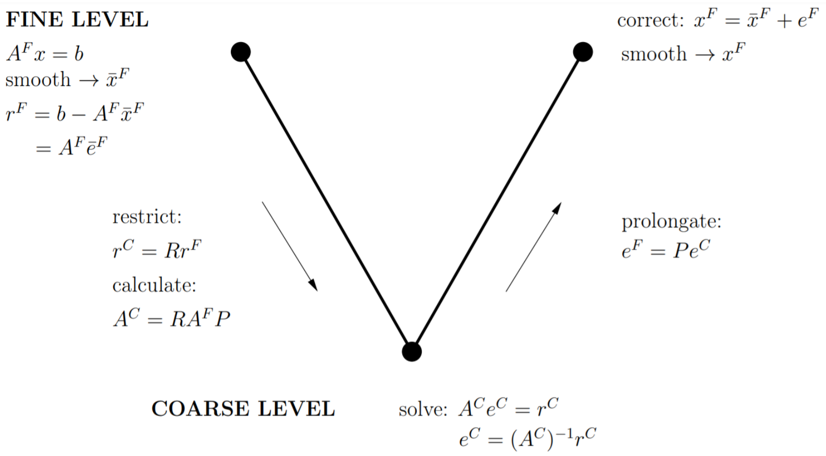

Figure 3.2: Single two-level V-cycle of the SAMG solver [5].

This was a broad example of the solution procedure for a single two-level V-cycle of the SAMG solver, in-depth study of the solution procedures and multigrid cycles is further explored by Uroić [5].

3.3 Near-Wall Treatment

When observing wall bounded turbulent flows, turbulent boundary layer can be divided into the inner and outer layer. In this thesis only the nature of the inner layer will be investigated, as all the important phenomena in relation to the modelling of near-wall flows in CFD occurs within the inner layer. The inner layer can be further divided into three regions: viscous sublayer, buffer layer and inertial sublayer. An example of a turbulent boundary layer is presented in Figure 3.3, where u^+ represents dimensionless velocity, located on the ordinate, and y^+ represents dimensionless distance from the wall, located on the logarithmically scaled abscissa. A value of y^+ can be calculated as follows:

$$y^+ = \frac{u_\tau y}{\nu}, \qquad u_\tau = \sqrt{\frac{\tau_{\mathrm{w}}}{\rho}} \tag{3.42}$$

where u_τ is the friction velocity, y is the wall distance, ν is the kinematic viscosity, τ_w is the wall shear stress and ρ is the fluid density.

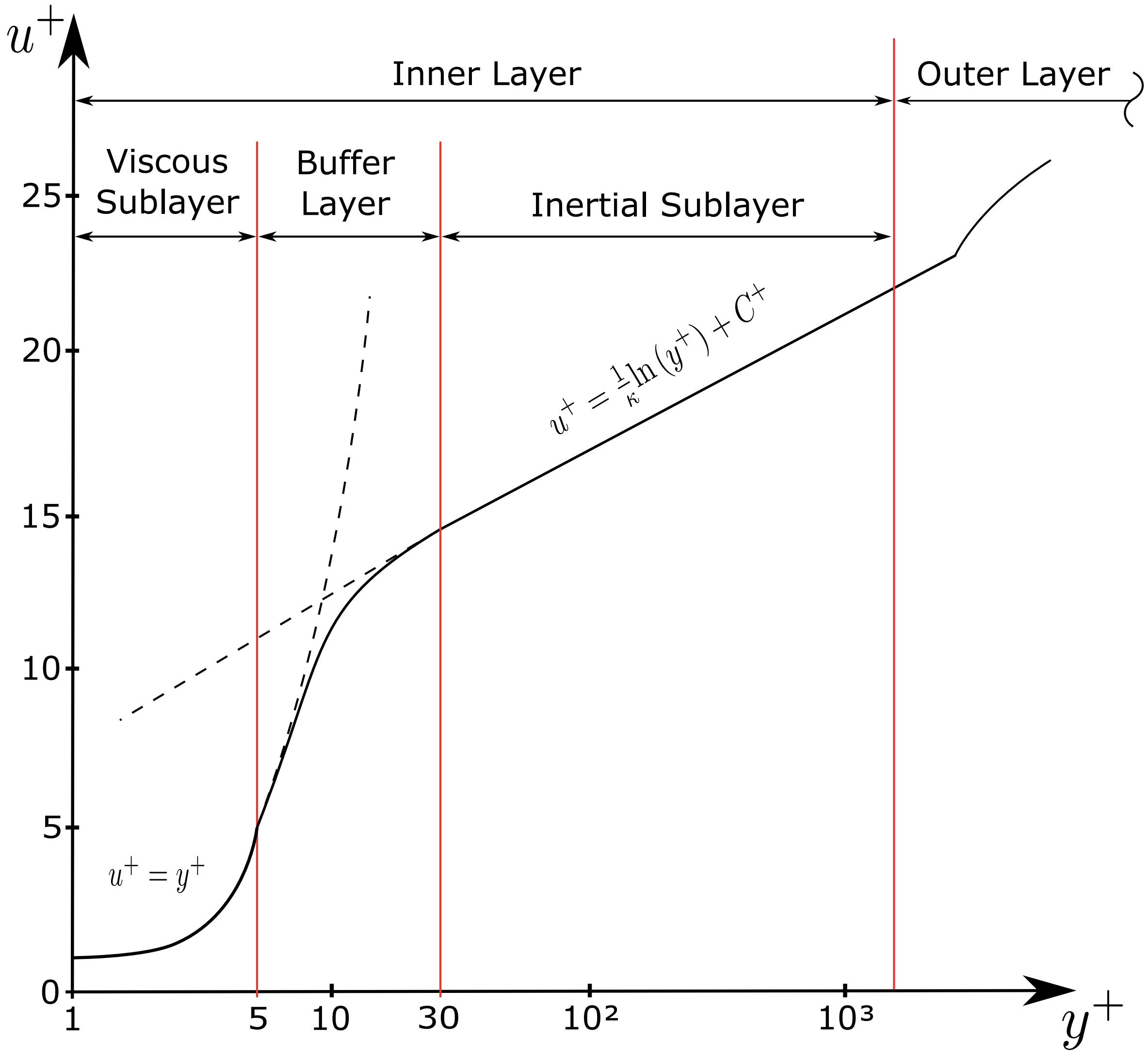

Figure 3.3: A turbulent boundary layer.

Nature of the flow in the inner layer is drastically different near the wall and away from it. The viscous sublayer is located in the immediate proximity of the wall ($y^+ < 5$), where turbulent pulsations are dampened by the wall itself and the effects of molecular viscosity are predominant, while the effects of turbulent viscosity are negligible. In the inertial sublayer influence of the wall fades, turbulent pulsation grow stronger and the effects of turbulent viscosity become predominant, while effects of molecular viscosity become negligible. Buffer layer serves as a transition region between the viscous and inertial sublayers, as both molecular and turbulent viscosity are equally important in it. The inner layer, depending on the value of the Reynolds number, can span up to anywhere from $y^+ = 200$ to the point where the value of y^+ is equal to a couple of thousand. [28]

Applying the assumption of a fully developed equilibrium boundary layer, when modelling near-wall flows using CFD, one of the following two approaches can be chosen (Figure 3.4). High-Re approach requires the centroid of the first cell of the numerical mesh to be placed in the inertial sublayer. This way the inner tubulent layer is modelled using wall functions. On the other hand, Low-Re approach requires the centroid of the first cell to be placed in the viscous sublayer. In other words, the Low-Re approach requires that a value of y^+ doesn't exceed the value of 1 ($y^+ < 1$), however, for complicated geometries it is acceptable that a value y^+ doesn't exceed the value of 5 ($y^+ < 5$). used.

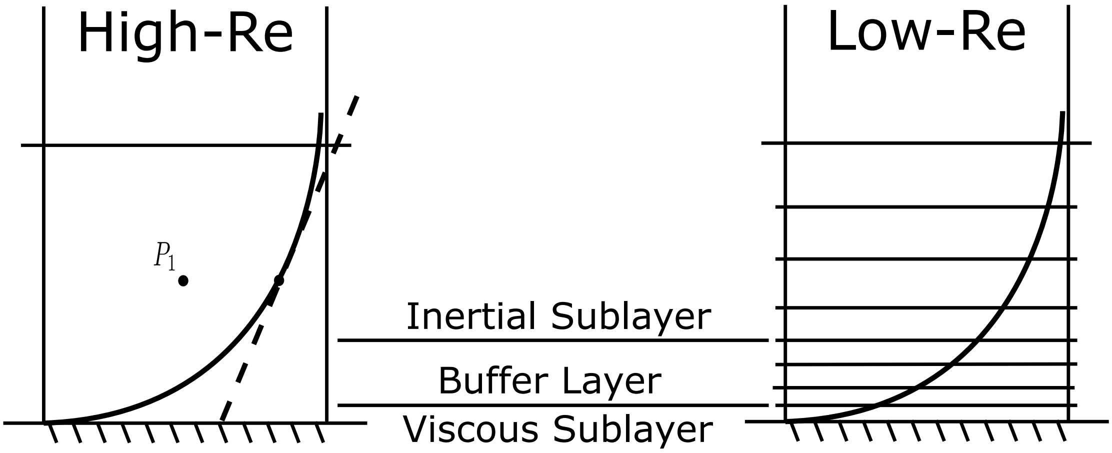

Figure 3.4: Wall treatment [6].

When simulating the transitional laminar-to-turbulent flow, Low-Re approach is generally recommended and that is why it is used in this thesis to validate $\gamma - Re_\theta$ transitional turbulence model.

3.4 Closure

This chapter served as an overview of the implemented numerical model, describing The Finite Volume Method. Moreover, short description of the boundary conditions, general equation discretisation and Implicitly Coupled Pressure-Velocity systems was given. Next chapter introduces geometries used for the CFD simulations, the resulting computational domains as well as applied boundary conditions.

4 | Geometry and Computational Domain

4.1 Introduction

The previous chapter served as an overview of the implemented numerical model, describing The Finite Volume Method. This chapter presents the details of geometries used for the CFD simulations and describes the resulting computational domains as well as applied boundary conditions.

Considering that this Thesis was written as a part of the NATO Applied Vehicle Technology (AVT) project, used meshes were acquired from the project's workshop [17].

4.2 Flat Plate

The dimension of the geometry in the direction of the z axis is 1m, however, since this is a 2D case only 1 cell spans in that direction. The bottom boundary of the computational domain is placed on top of the Flat Plate geometry, so the only other dimension needed to define the geometry is its length, which is $L = 1$m. The Cartesian coordinate system has the origin at the leading edge of the Flat Plate, with the abscissa aligned with the Flat Plate. The computational domain is in the shape of a rectangle with the length of $1.5L$ and the height of $0.25L$. The inlet of the computational domain is located $0.25L$ upstream of the leading edge of the Flat Plate, i.e. at $x = -0.25L$. The outlet is located $0.25L$ downstream of the trailing edge of the Flat Plate, i.e. at $x = 1.25L$. Lastly, the top boundary of the computational domain is located $0.25L$ from the surface of the Flat Plate, i.e. at $y = 0.25L$.

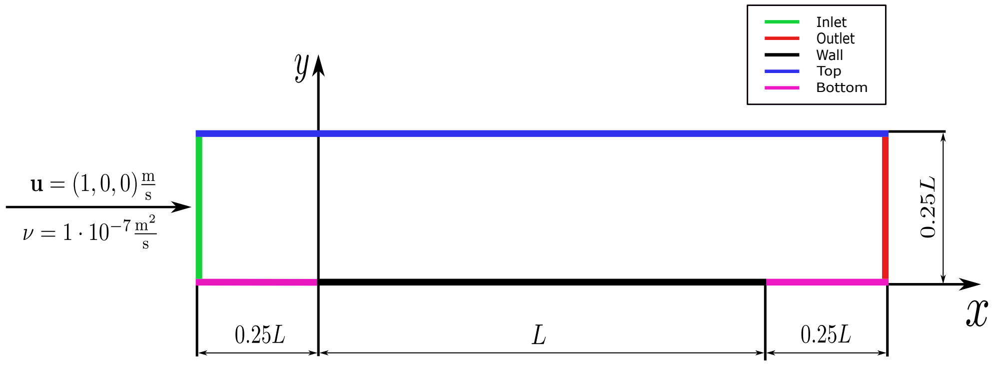

Figure 4.1: Flat Plate Computational Domain.

4.2.1 Boundary Conditions

For each turbulence model two sets of boundary conditions are applied on the computational domain, one representing low-turbulence case (T3AM) and the other representing high-turbulence case (T3A).

Boundary conditions of a type **fixedValue** are equivalent to the *Dirichlet* boundary condition (Eq. 3.4), while those of a type **zeroGradient** are equivalent to the *Von Neumann* boundary condition (Eq. 3.5). The value of $\mathbf{u}$ at the outlet is defined using the **inletOutlet** boundary condition, while the value of p, at the same place is defined using the **outletInlet** boundary conditions (Table 4.1 - 4.4). Both of them are derived from a combination of the *Dirichlet* and *Von Neumann* boundary conditions, depending on the incoming and outgoing flow direction.

At the wall, for the k - ω SST turbulence model, values of k, ω and ν_T are defined using the appropriate wall functions, i.e. **kqRWallFunction**, **omegaWallFunction** and **nutkWallFunction**, respectively. For the γ - Re_θ turbulence model, value of k at the wall is defined by the *Dirichlet* boundary condition, while values of ω and ν_T are defined by the appropriate wall functions, i.e. **omegaSwitchWallFunction** and **nutLowReWallFunction**, respectively (Table 4.1 - 4.4).

Lastly, the **blockSymmPlane** boundary condition, which defines the value of $\mathbf{u}$ at the bottom boundary, is used with the implicitly coupled pressure-velocity systems and is equivalent to the *Symmetry Plane* boundary condition (Table 4.1 - 4.4).

T3AM	Inlet	Outlet	Wall	Top	Bottom
U	type: fixedValue value: (1 0 0)	type: inletOutlet inletValue: (0 0 0) value: (1 0 0)	type: fixedValue value: (0 0 0)	type: zeroGradient	type: blockSymmPlane
p	type: zeroGradient	type: outletInlet outletValue: (0 0 0) value: (0 0 0)	type: zeroGradient	type: zeroGradient	type: zeroGradient
k	type: fixedValue value: 0.0001504	type: zeroGradient	type: kqRWallFunction value: 0	type: zeroGradient	type: zeroGradient
ω	type: fixedValue value: 60.1261	type: zeroGradient	type: omegaWallFunction value: 60.1261	type: zeroGradient	type: zeroGradient
ν_T	type: zeroGradient	type: zeroGradient	type: nutkWallFunction value: 0	type: zeroGradient	type: zeroGradient

Table 4.1: Boundary conditions for the low-turbulence Flat Plate case (T3AM), k - ω SST turbulence model.

T3AM	Inlet	Outlet	Wall	Top	Bottom
U	type: fixedValue value: (1 0 0)	type: inletOutlet inletValue: (0 0 0) value: (1 0 0)	type: fixedValue value: (0 0 0)	type: zeroGradient	type: blockSymmPlane
p	type: zeroGradient	type: outletInlet outletValue: (0 0 0) value: (0 0 0)	type: zeroGradient	type: zeroGradient	type: zeroGradient
k	type: fixedValue value: 0.004319	type: zeroGradient	type: kqRWallFunction value: 0	type: zeroGradient	type: zeroGradient
ω	type: fixedValue value: 154.25	type: zeroGradient	type: omegaWallFunction value: 154.25	type: zeroGradient	type: zeroGradient
ν_T	type: zeroGradient	type: zeroGradient	type: nutkWallFunction value: 0	type: zeroGradient	type: zeroGradient

Table 4.2: Boundary conditions for the high-turbulence Flat Plate case (T3A), k - ω SST turbulence model.

T3AM	Inlet	Outlet	Wall	Top	Bottom
U	type: fixedValue value: (1 0 0)	type: inletOutlet inletValue: (0 0 0) value: (1 0 0)	type: fixedValue value: (0 0 0)	type: zeroGradient	type: blockSymmPlane
p	type: zeroGradient	type: outletInlet outletValue: (0 0 0) value: (0 0 0)	type: zeroGradient	type: zeroGradient	type: zeroGradient
k	type: fixedValue value: 0.0001504	type: zeroGradient	type: fixedValue value: 0	type: zeroGradient	type: zeroGradient
ω	type: fixedValue value: 60.1261	type: zeroGradient	type: omegaSwitchWallFunction value: 60.1261	type: zeroGradient	type: zeroGradient
γ	type: fixedValue value: 1	type: zeroGradient	type: zeroGradient	type: zeroGradient	type: zeroGradient
$\widetilde{Re}_{\theta\mathrm{t}}$	type: fixedValue value: 583.5052805	type: zeroGradient	type:zeroGradient	type: zeroGradient	type: zeroGradient
ν_T	type: zeroGradient	type: zeroGradient	type: nutLowReWallFunction value: 0	type: zeroGradient	type: zeroGradient

Table 4.3: Boundary conditions for the low-turbulence Flat Plate case (T3AM), transitional turbulence models.

T3A	Inlet	Outlet	Wall	Top	Bottom
U	type: fixedValue value: (1 0 0)	type: inletOutlet inletValue: (0 0 0) value: (1 0 0)	type: fixedValue value: (0 0 0)	type: zeroGradient	type: blockSymmPlane
p	type: zeroGradient	type: outletInlet outletValue: (0 0 0) value: (0 0 0)	type: zeroGradient	type: zeroGradient	type: zeroGradient
k	type: fixedValue value: 0.004319	type: zeroGradient	type: fixedValue value: 0	type: zeroGradient	type: zeroGradient
ω	type: fixedValue value: 308.5	type: zeroGradient	type: omegaSwitchWallFunction value: 308.5	type: zeroGradient	type: zeroGradient
γ	type: fixedValue value: 1	type: zeroGradient	type: zeroGradient	type: zeroGradient	type: zeroGradient
$\widetilde{Re}_{\theta \mathrm{t}}$	type: fixedValue value: 115.7052	type: zeroGradient	type:zeroGradient	type: zeroGradient	type: zeroGradient
ν_{T}	type: zeroGradient	type: zeroGradient	type: nutLowReWallFunction value: 0	type: zeroGradient	type: zeroGradient

Table 4.4: Boundary conditions for the low-turbulence Flat Plate case (T3A), transitional turbulence models.

4.2.2 Computational Mesh

Following 9 meshes were used for the 2D Flat Plate case :

MESH	N_{cells}	N_{plate}	r	$AR_{\max}$	$(\textit{non-ortho})_{\max}$
No. 1	$2.048 \cdot 10^6$	2560	1	$10,799,485.41$	72.56
No. 2	$1.310720 \cdot 10^6$	2048	1.25	$8,632,059.04$	75.84
No. 3	$1.003520 \cdot 10^6$	1792	1.42857	$7,547,458.56$	77.37
No. 4	$0.8 \cdot 10^6$	1600	1.6	$6,733,390.11$	78.77
No. 5	$0.512 \cdot 10^6$	1280	2	$5,374,739.52$	80.93
No. 6	$0.327680 \cdot 10^6$	1024	2.5	$4,284,910.85$	82.73
No. 7	$0.250880 \cdot 10^6$	896	2.85714	$3,738,407.39$	83.62
No. 8	$0.2 \cdot 10^6$	800	3.2	$3,327,833.58$	84.32
No. 9	$0.128 \cdot 10^6$	640	4	$2,642,629.22$	85.42

Table 4.5: Meshes used for the 2D Flat Plate case.

Here N_{cells} is a total number of cells in the mesh, N_{plate} a total number of faces on the plate (wall), r is the grid refinement ratio, $AR_{\max}$ is the maximum cell aspect ratio and $(\textit{non-ortho})_{\max}$ is the maximum cell non-orthogonality. Grid refinement ratio r is calculated as follows:

$$r = \left(\frac{N_{\text{cells,1}}}{N_{\text{cells,i}}} \right)^{\frac{1}{D}}, \tag{4.1}$$

where $N_{\text{cells,1}}$ is a total number of cells in the finest mesh, $N_{\text{cells,i}}$ is a total number of cells in the other less fine meshes and D is a number the mesh dimensions (in this case $D = 2$).

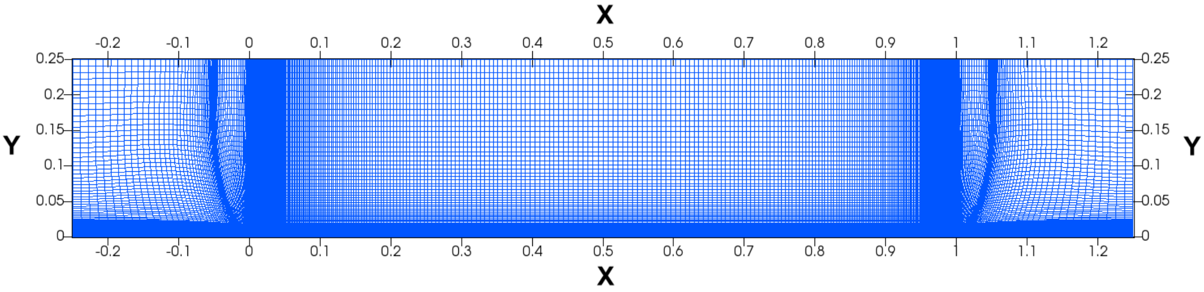

Figure 4.2: Example of the coarsest mesh of the 2D Flat Plate case.

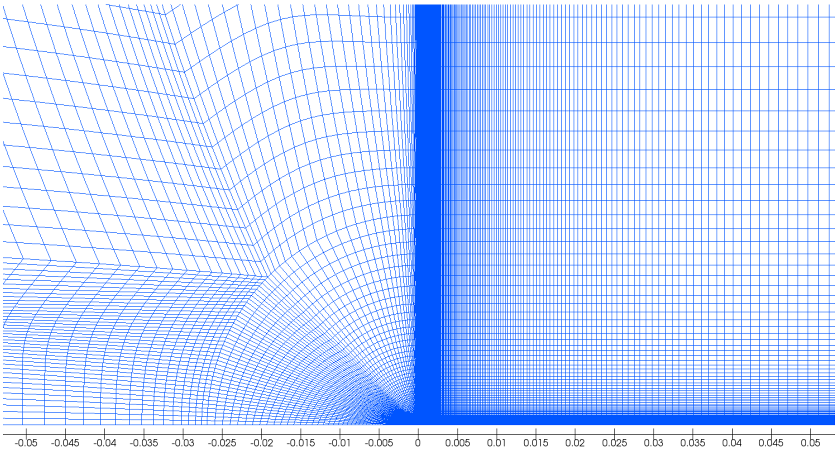

Figure 4.3: Enlarged section of the coarsest mesh of the 2D Flat Plate case.

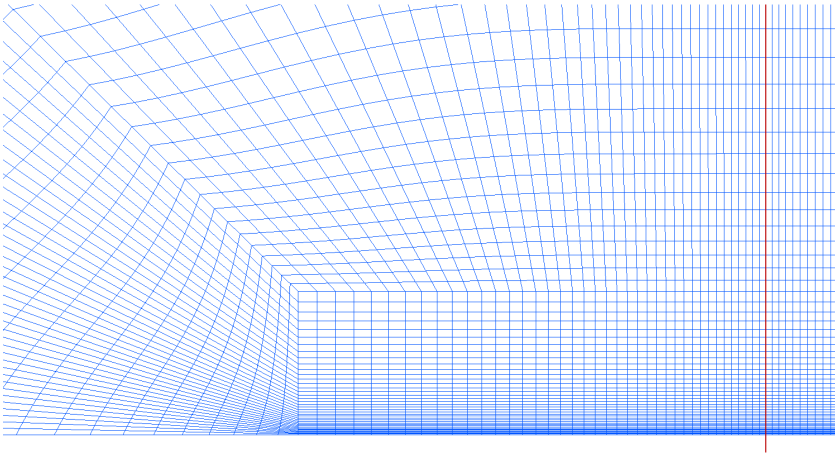

Figure 4.4: Leading edge of the coarsest mesh of the 2D Flat Plate case (location marked with a red line).

4.3 Eppler 387 Airfoil

For the Eppler 387 airfoil geometry of the chord length $c = 1$m, two rectangular domains are created. The dimension of the geometry in the spanwise direction is 1m, however, since this is a 2D case only 1 cell spans in that direction. The two domains are created following the same set of rules and are used to calculate the flow around the Eppler 387 airfoil at the angles of attack of $\alpha = 1^\circ$ and $\alpha = 7^\circ$. The length of the rectangular computational domain is $36c$ and the height is $24c$. The origin of the Cartesian coordinate system is placed at the leading edge of the airfoil and the abscissa is aligned with the incoming flow. The inlet of the computational domain is located $12c$ downstream of the leading edge of the airfoil, i.e. at $x = -12c$. On the other hand, the outlet is located $24c$ upstream of the leading edge of the airfoil, i.e. at $x = 24c$. Lastly, the top and bottom boundaries of the computational domain are located $12c$ from the abscissa in the positive and negative direction, i.e. at $y = 12c$ and $y = -12c$, respectively.

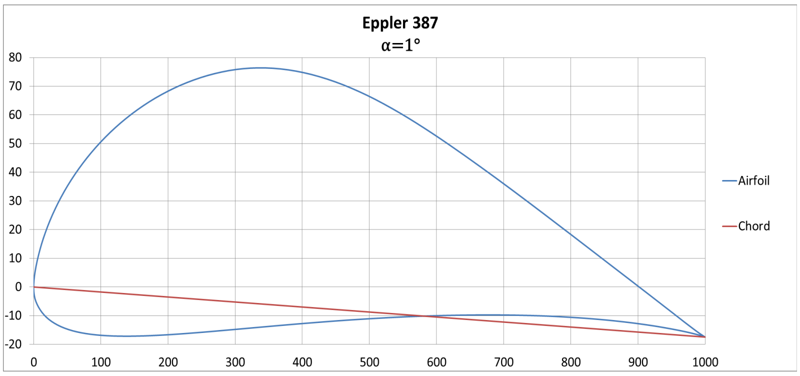

Figure 4.5: Eppler 387 geometry at the angle of attack of $\alpha = 1°$.

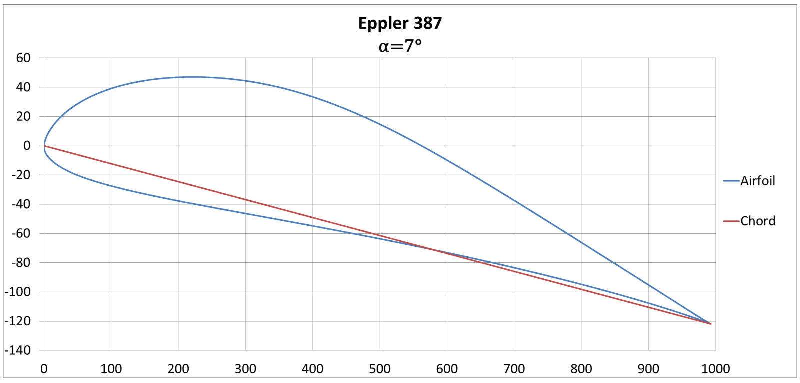

Figure 4.6: Eppler 387 geometry at the angle of attack of $\alpha = 7°$.

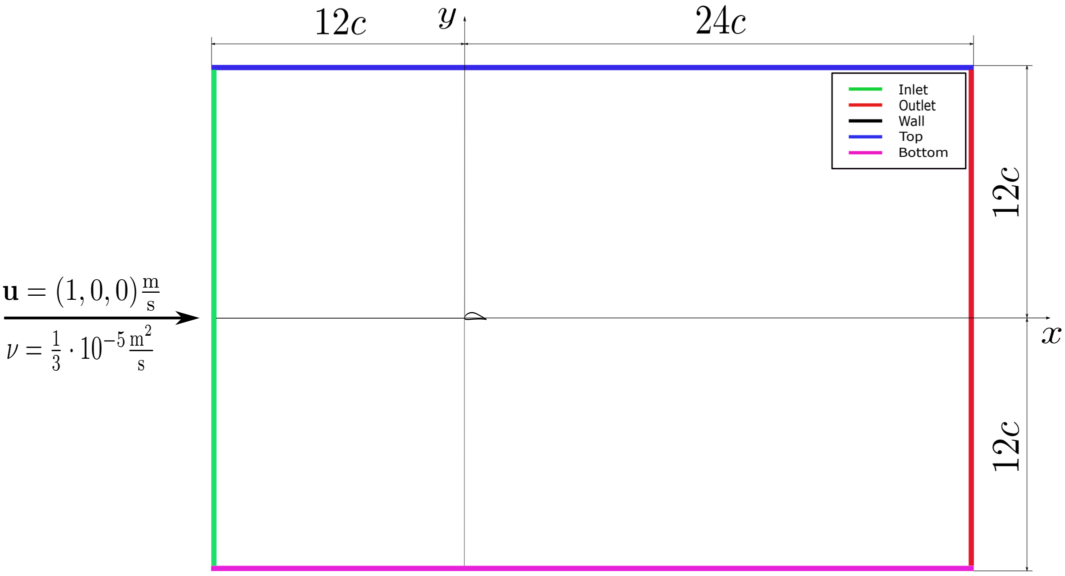

Figure 4.7: 2D Eppler 387 Computational Domain.

4.3.1 Boundary Conditions

For each turbulence model one set of boundary conditions is applied, however, on two different computational domains. All boundary conditions used in this case are previously explained in the section **4.2**.

1° | 7°	Inlet	Outlet	Wall	Top	Bottom
U	type: fixedValue value: (1 0 0)	type: inletOutlet inletValue: (0 0 0) value: (1 0 0)	type: fixedValue value: (0 0 0)	type: blockSymmPlane	type: blockSymmPlane
p	type: zeroGradient	type: outletInlet outletValue: (0 0 0) value: (0 0 0)	type: zeroGradient	type: zeroGradient	type: zeroGradient
k	type: fixedValue value: 0.00015	type: zeroGradient	type: kqRWallFunction value: 0	type: zeroGradient	type: zeroGradient
ω	type: fixedValue value: 15000	type: zeroGradient	type: omegaWallFunction value: 15000	type: zeroGradient	type: zeroGradient
ν_T	type: zeroGradient	type: zeroGradient	type: nutkWallFunction value: 0	type: zeroGradient	type: zeroGradient

Table 4.6: Boundary conditions for the Eppler 387 case, k - ω SST turbulence model.

1°|7°	Inlet	Outlet	Wall	Top	Bottom
U	type: fixedValue value: (1 0 0)	type: inletOutlet inletValue: (0 0 0) value: (1 0 0)	type: fixedValue value: (0 0 0)	type: blockSymmPlane	type: blockSymmPlane
p	type: zeroGradient	type: outletInlet outletValue: (0 0 0) value: (0 0 0)	type: zeroGradient	type: zeroGradient	type: zeroGradient
k	type: fixedValue value: 0.00015	type: zeroGradient	type: fixedValue value: 0	type: zeroGradient	type: zeroGradient
ω	type: fixedValue value: 15000	type: zeroGradient	type: omegaSwitchWallFunction value: 15000	type: zeroGradient	type: zeroGradient
γ	type: fixedValue value: 1	type: zeroGradient	type: zeroGradient	type: zeroGradient	type: zeroGradient
$\widetilde{Re}_{\theta t}$	type: fixedValue value: 584.3016	type: zeroGradient	type:zeroGradient	type: zeroGradient	type: zeroGradient
ν_T	type: zeroGradient	type: zeroGradient	type: nutLowReWallFunction value: 0	type: zeroGradient	type: zeroGradient

Table 4.7: Boundary conditions for the Eppler 387 case, transitional turbulence models.

4.3.2 Computational Mesh

Following 9 meshes were used for the 2D Eppler 387 case :

MESH	N_{cells}	N_{foil}	r
No. 1	$3.520512 \cdot 10^6$	3072	1
No. 2	$2.444800 \cdot 10^6$	2560	1.2
No. 3	$1.564672 \cdot 10^6$	2048	1.5
No. 4	$1.194592 \cdot 10^6$	1792	1.71429
No. 5	$0.88012 \cdot 10^6$	1536	2
No. 6	$0.611200 \cdot 10^6$	1280	2.4
No. 7	$0.391168 \cdot 10^6$	1024	2.35714
No. 8	$0.299488 \cdot 10^6$	896	3.42857
No. 9	$0.220032 \cdot 10^6$	768	4

Table 4.8: Meshes used for the 2D Eppler 387 Case,

MESH	$AR_{\text{max}, \, \alpha = 1^\circ}$	$(non\text{-}ortho)_{\text{max}, \, \alpha = 1^\circ}$	$AR_{\text{max}, \, \alpha = 7^\circ}$	$(non\text{-}ortho)_{\text{max}, \, \alpha = 7^\circ}$
No. 1	$523,743.72$	45.98	$529,713.35$	45.39
No. 2	$422,928.01$	51.06	$427,930.09$	50.5
No. 3	$320,164$	56.92	$324,347.27$	56.43
No. 4	$267,953.11$	60.17	$271,773.5$	59.71
No. 5	$215,302$	63.64	$218,782.16$	63.24
No. 6	$162,667.34$	67.27	$165,797.3$	66.91
No. 7	$111,258.57$	70.93	$114,019.86$	70.64
No. 8	$96,428.18$	72.89	$96,214.9$	72.63
No. 9	$82,538.9$	74.72	$82,324.85$	74.51

Table 4.9: Maximum cell aspect ratio and non-orthogonality.

Here N_{cells} is a total number of cells in the mesh, N_{foil} a total number of faces on the airfoil (wall), r is the grid refinement ratio (E.q. 4.1), AR_{max} is the maximum cell aspect ratio and $(non\text{-}ortho)_{\text{max}}$ is the maximum cell non-orthogonality.

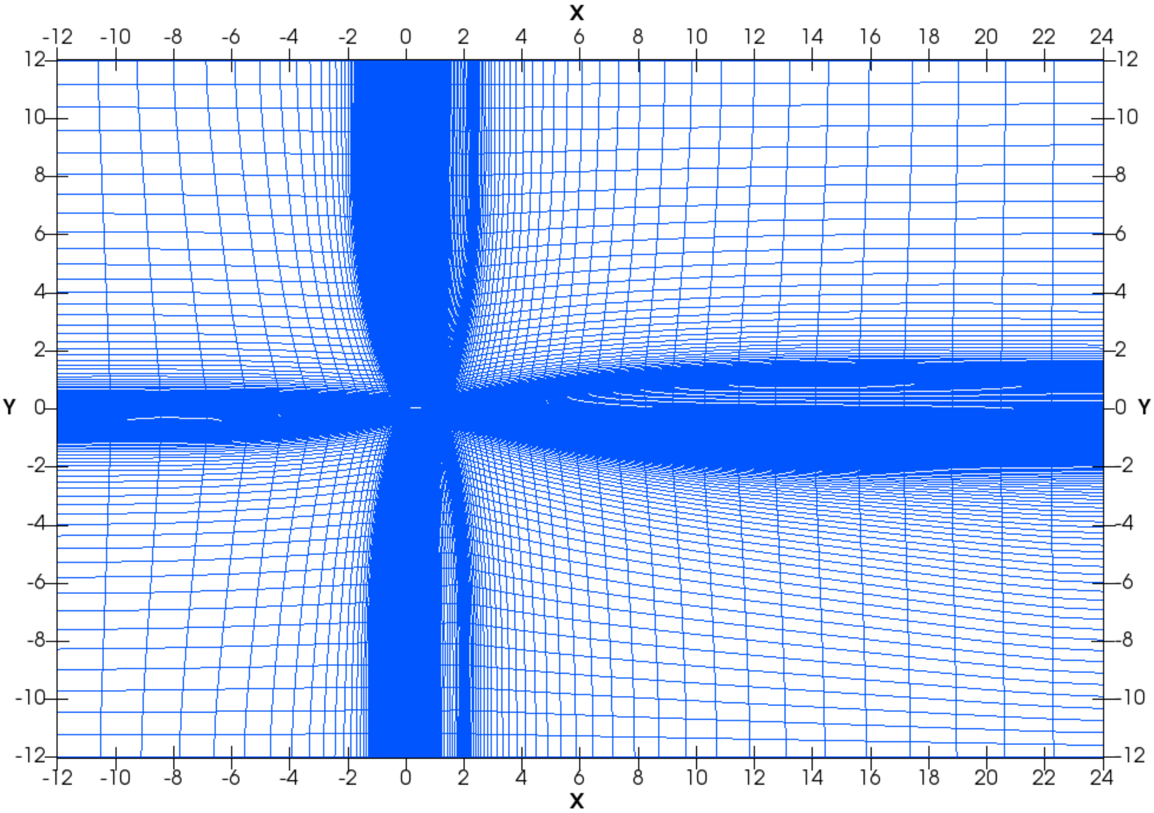

Figure 4.8: Example of the coarsest 2D Eppler 387 airfoil mesh at the angle $\alpha = 1°$.

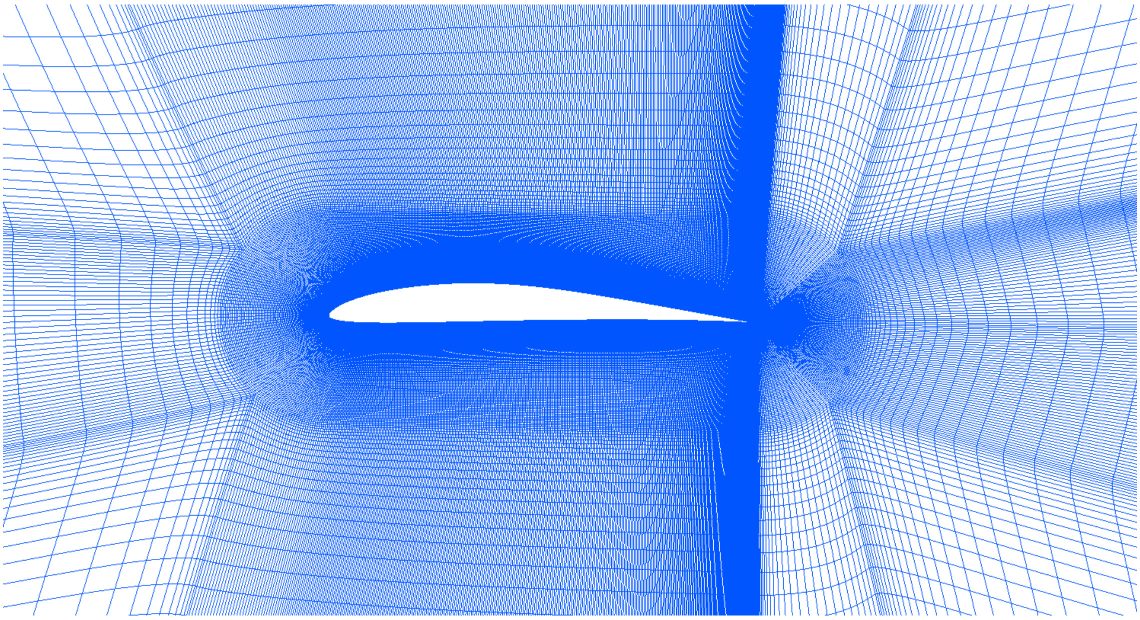

Figure 4.9: Enlarged section of the coarsest 2D Eppler 387 airfoil mesh at the angle $\alpha = 1°$.

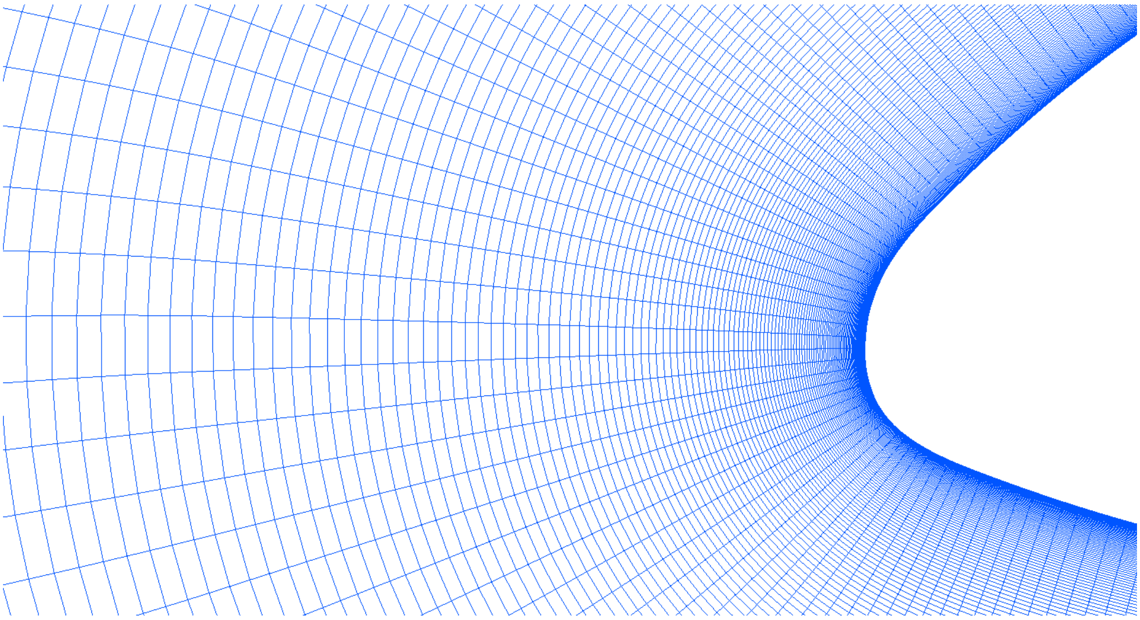

Figure 4.10: Leading edge of the coarsest 2D Eppler 387 airfoil mesh at the angle $\alpha = 1°$.

4.4 Closure

This chapter introduced Flat Plate and Eppler 387 geometries used in numerical simulations. Furthermore computational domains and boundary conditions applied on them were also described. Lastly, short overview of used meshes was given. Following chapter presents the results of numerical simulations made in the **foam-extend** environment. Simulation results are compared with the available experimental data and flow fields of quantities of interest are presented.

5 | Analysis and Validation of Results

5.1 Introduction

In the previous chapter the geometries and resulting computational domains of the 2D Flat Plate and 2D Eppler 387 cases were described. Furthermore, an overview of the boundary conditions applied on the computational domains was given, as well as an overview of the meshes used in the cases.

This chapter presents the data obtained from a series of numerical simulations. All simulations were firstly initialized using the **potentialFoam** solver, which solves the potential flow over the geometry. The results were then obtained using the implicitly coupled pressure-velocity solver **pUCoupledFoam** in addition with the k - ω SST turbulence model and γ - Re_θ transitional turbulence model.

The results of both turbulence models are plotted in graphs where they are compared with each other and experimental data. In the presented graphs error bars depicting the numerical uncertainty of the results, with regard to the density of the used meshes, can be seen. Numerical uncertainty of the results was estimated in accordance with Eca et al. [10]. Lastly, fields of quantities of interest are also presented in their respective figures.

5.2 Uncertainty Estimation

In this section a brief overview of the uncertainty estimation procedure by Eca et al. [10] will be given. It is assumed that the contribution of the round-off and iterative errors to the numerical error is negligible compared to the discretization error. Furthermore, it is assumed that the lowest-order schemes used in the discretization are second or first-order accurate.

The numerical uncertainty U_ϕ is determined from an error estimate ε_ϕ. The error estimate ε_ϕ is calculated as follows:

$$\varepsilon_\phi \simeq \delta_{\mathrm{RE}} = \phi_{\mathrm{i}} - \phi_{\mathrm{o}} = \alpha h_{\mathrm{i}}^{p} \ , \tag{5.1}$$

where ϕ_{i} is the numerical solution of any local or integral scalar quantity on a given grid, ϕ_{o} is the estimate of the exact solution, α is a constant, h_{i} is the typical cell size and p is the observed order of grid convergence. The conditions for the reliable use of Eq. 5.1 are that the observed grids must be in the "asymptotic range" and geometrically similar. However, for practical CFD problems that consist of complex geometries and complex equations (e.g. turbulent flow) it is nigh impossible to meet these conditions. Therefore meeting said conditions, when dealing with practical CFD problems, becomes an exception rather than the rule. [10]

In order to deal with the shortcomings of practical CFD problems following 3 equations are added:

$$\varepsilon_\phi \simeq \delta_1 = \phi_\mathrm{i} - \phi_\mathrm{o} = \alpha h_\mathrm{i} \,, \tag{5.2}$$

$$\varepsilon_\phi \simeq \delta_2 = \phi_\mathrm{i} - \phi_\mathrm{o} = \alpha h_\mathrm{i}^2 \,, \tag{5.3}$$

$$\varepsilon_\phi \simeq \delta_{12} = \phi_\mathrm{i} - \phi_\mathrm{o} = \alpha_1 h_\mathrm{i} + \alpha_2 h_\mathrm{i}^2 \,. \tag{5.4}$$

The procedure for the estimation of the numerical uncertainty U_ϕ, by Eca et al. [10], consist of following steps:

1. Determine the error estimate ε_ϕ:
   - Solve Eq. 5.1 in the least-squares sense, with and without weights, to obtain δ_RE, p and the standard deviations σ of the two fits. If any of the fits exhibits $0.5 \le p \le 2$, then the error estimate is $\varepsilon_\phi = \delta_\mathrm{Re}$. However, if both fits exhibit $0.5 \le p \le 2$, then the fit with the smallest standard deviation is selected and the error estimate ε_ϕ is equal to the value of δ_Re of that fit.
   - If the order of grid convergence p is $p > 2$, solve Eq. 5.2 and Eq. 5.3 in the least-squares sense, with and without weights, and determine the standard deviations σ of the four fits. The fit with the smallest standard deviation σ is chosen and the error estimate ε_ϕ is equal to the value of δ_Re of that fit.
   - If the order of grid convergence p is $p < 0.5$, solve Eq. 5.2, Eq. 5.3 and Eq. 5.4 in the least-squares sense, with and without weights, and determine the standard deviations σ of the six fits. The fit with the smallest standard deviation σ is chosen and the error estimate ε_ϕ is equal to the value of δ_Re of that fit.
2. Determine a data range parameter Δ_ϕ to assess the quality of the fit used to obtain the error estimate ε_ϕ:

   $$\Delta_\phi = \frac{(\phi_\mathrm{i})_\mathrm{max} - (\phi_\mathrm{i})_\mathrm{min}}{n_\mathrm{g} - 1} \,, \tag{5.5}$$

   where n_g is the number of used meshes, which should be at least 4.
3. Determine the safety factor F_S from the following conditions:

  - If the order of grid convergence p is $0.5 \leq p < 2.1$ and if $\sigma < \Delta_\phi$, then the saftey factor equals to $F_\mathrm{S} = 1.25$.
  - Otherwise, safety factor equals to $F_\mathrm{S} = 3$.

4. Calculate the numerical uncertainty U_ϕ as follows:
   - For $\sigma < \Delta_\phi$:
$$U_\phi(\phi_\mathrm{i}) = F_\mathrm{S}\varepsilon_\phi(\phi_\mathrm{i}) + \sigma + |\phi_\mathrm{i} - \phi_\mathrm{fit}| \ . \tag{5.6}$$
   - For $\sigma \geq \Delta_\phi$:
$$U_\phi(\phi_\mathrm{i}) = 3\frac{\sigma}{\Delta_\phi}\left(\varepsilon_\phi(\phi_\mathrm{i}) + \sigma + |\phi_\mathrm{i} - \phi_\mathrm{fit}|\right) \ . \tag{5.7}$$

5.3 2D Flat Plate

In this section, results of the 2D numerical simulations performed on the Flat Plate geometry and corresponding computational domain (Figure 4.1) are presented. Two sets of boundary conditions are applied on the computational domain, one for the low-turbulence T3AM case (Table 4.1 and 4.3) and the other for the high-turbulence T3A case (Table 4.2 and 4.4). Experimental data was obtained from the European Research Community On Flow, Turbulence and Combustion (ERCOFTAC) "Classic Collection Database" [29].

5.3.1 Low-Turbulence T3AM Case

The value of the turbulence intensity Tu (Eq. 2.54) for the low-turbulence T3AM case is $Tu = 1.00135\%$. In this subsection the experimental data is compared with the skin friction coefficient C_f and mean horizontal velocity U_x/U_∞ results, with C_f calculated as follows:

$$C_\mathrm{f} = \frac{\tau_\mathrm{w}}{\frac{1}{2}\rho U_\infty^2} \ , \tag{5.8}$$

where τ_w is wall shear stress, ρ fluid density and U_∞ free-stream velocity. Furthermore, the intermittency field γ is presented in order to depict the transition region and demonstrate high mesh resolution requirements which the transitional turbulence model imposes on the user. Lastly, the residual convergence history is presented.

Skin Friction Coefficient

By comparing the skin friction coefficient results of both turbulence models with the experimental data it is clear that the transitional turbulence model γ - Re_θ produces more accurate results.

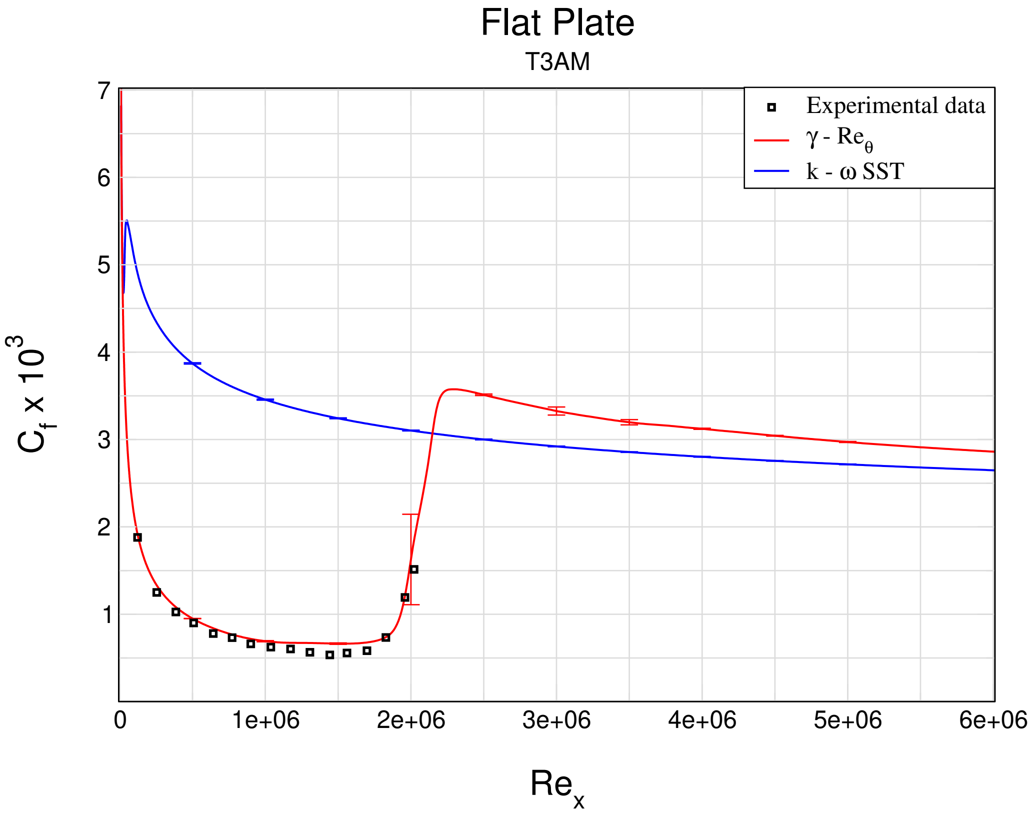

Figure 5.1: Flat Plate T3AM - Comparison of the skin friction coefficient C_f.

According to Figure 5.1 simulation results for the γ - Re_θ model show high degree of correspondence with the experimental data in the laminar region. Furthermore, the γ - Re_θ model accurately predicts the transition onset and results also show high degree of correspondence with the experimental data early in the transition region. Even though numerical uncertainty is low throughout most of the graph, high numerical uncertainty can be observed in the transition region. Lastly, it can be observed that both turbulence models show a converging trend towards the same value of C_f in the turbulent region.

Mean Horizontal Velocity

Three locations along the Flat Plate geometry were selected to present mean horizontal velocity profiles. The locations are at the coordinates $x/L = 0.10381$, $x/L = 0.18281$ and $x/L = 0.20216$.

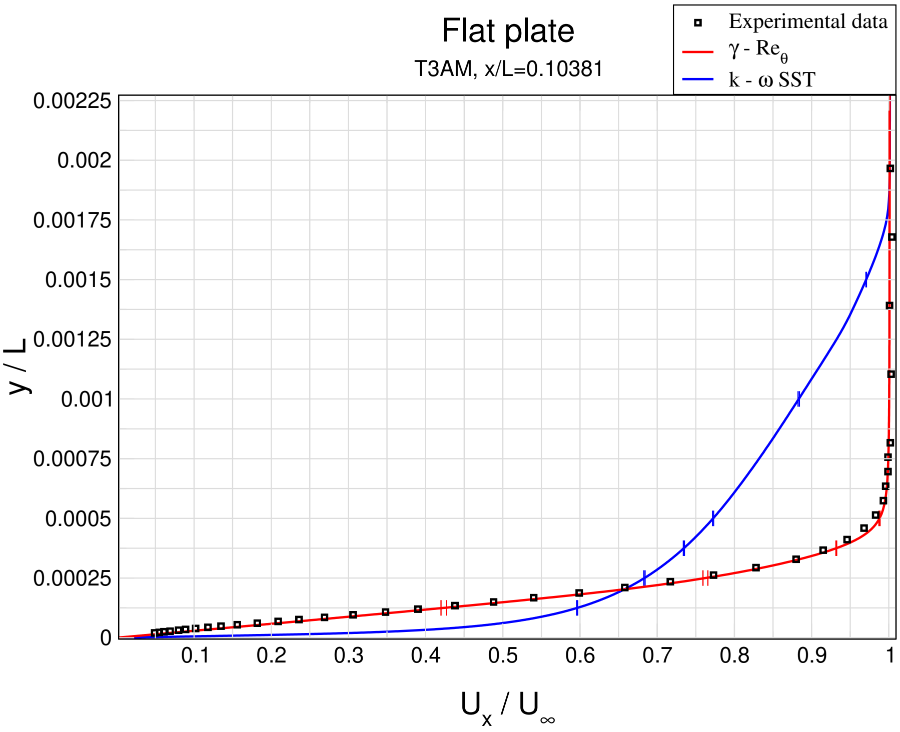

Figure 5.2: Flat Plate T3AM - Mean horizontal velocity profile at the location $x/L = 0.10381$.

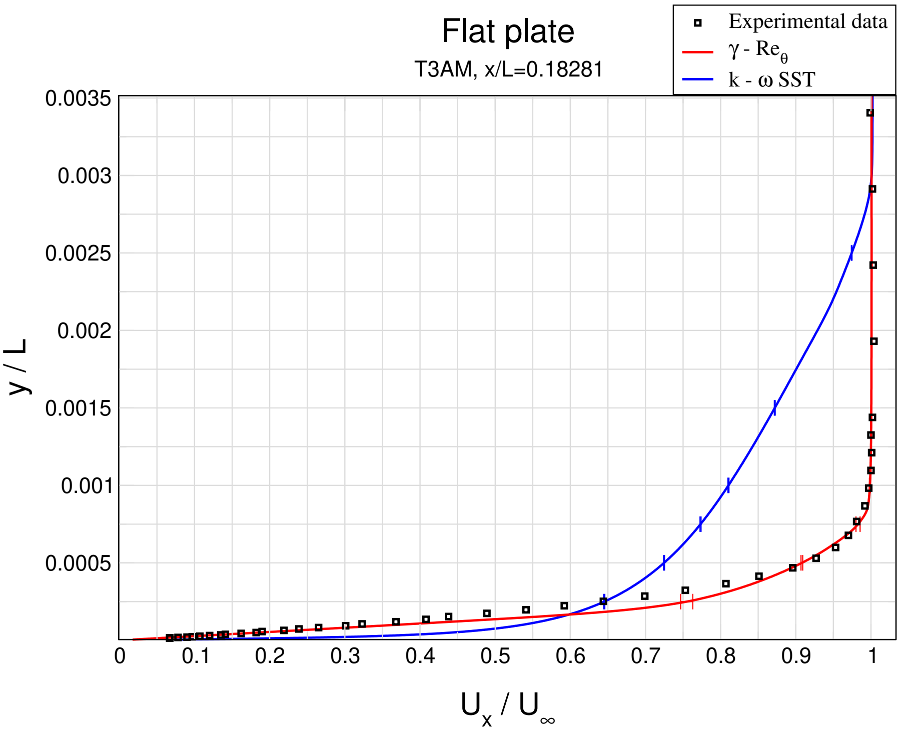

Figure 5.3: Flat Plate T3AM - Mean horizontal velocity profile at the location $x/L = 0.18281$.

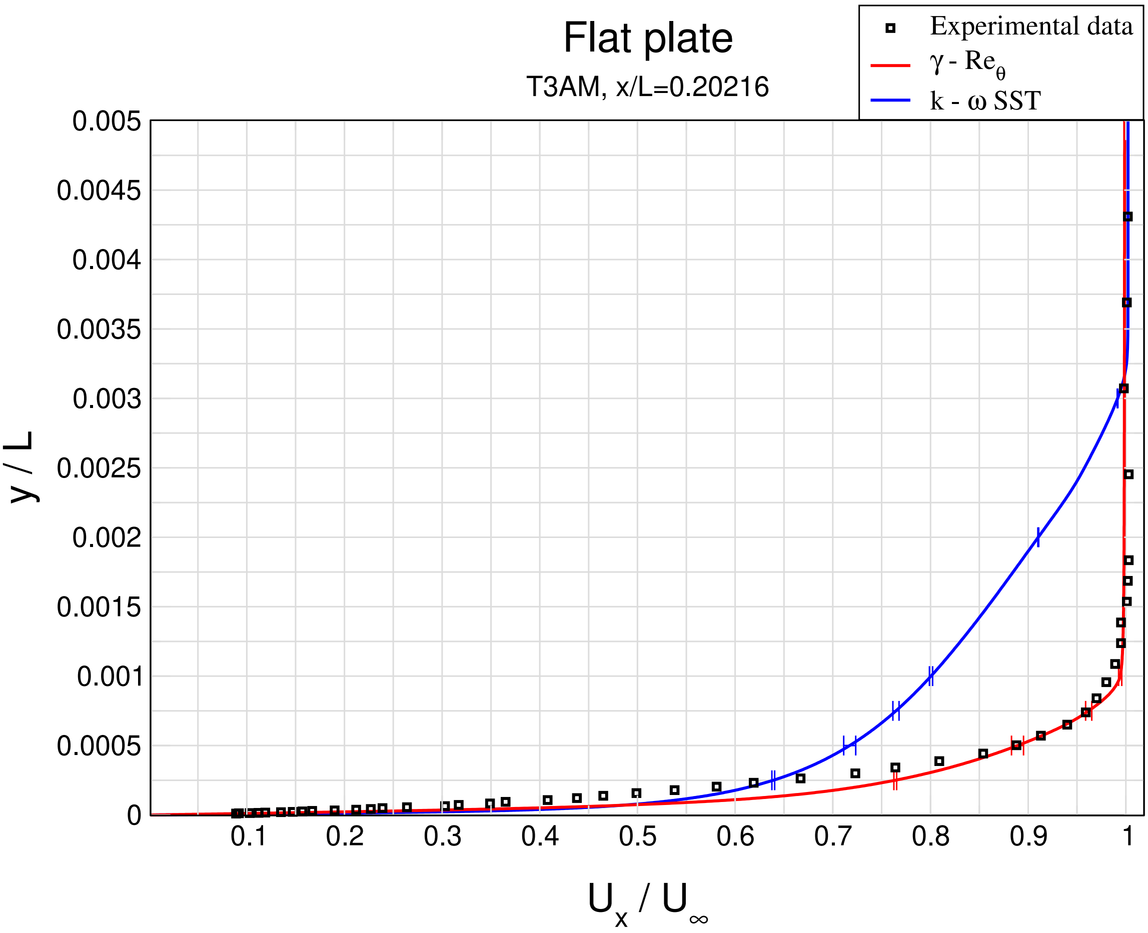

Figure 5.4: Flat Plate T3AM - Mean horizontal velocity profile at the location $x/L = 0.20216$.

By comparing the horizontal velocity profiles of both turbulence models it can be seen that the transitional turbulence model γ - Re_θ produces more accurate results at all 3 locations. If Figure 5.1 is compared with Figure 5.2 - Figure 5.4 it can be seen that Figure 5.2 represents mean horizontal velocity profile at the point located in the laminar region, while Figure 5.3 and Figure 5.4 represent mean horizontal velocity profiles at the points located in the transition region. Mean horizontal velocity profile of the γ - Re_θ model in the laminar region (Figure 5.2) shows good agreement with the experimental data. Furthermore, those in the transition region (Figure 5.3 and Figure 5.4), even though less accurate, still show high degree of correspondence with the experimental data. On the other hand, mean horizontal velocity profiles of the k - ω SST turbulence model show unsatisfying levels of accuracy, which is due to the use of wall functions to solve near-wall flow.

Intermittency Field

Intermittency field is presented in Figure 5.5, which consists of 3 segments. The main segment of the figure represents the γ field from the leading edge of the Flat Plate to the location where transition ends and the flow becomes fully turbulent. The first detail represents the transition region, while the second represents early section of the transition region.

By comparing the main segment and 2 details high mesh resolution near the wall can be observed. In order to capture the effects of the viscous sublayer when using transitional turbulence models, wall functions are avoided and the value of y^+ is required to be less than the value of 1 ($y^+ < 1$), or 5 for complicated geometries ($y^+ < 5$). This is done by positioning the first cell of the mesh in the viscous sublayer, i.e. using very low wall-spacing when constructing the mesh.

For the finest mesh (Figure 5.5), maximum value of the y^+ of the cell by the wall is $y^+ = 0.452$. The area of the same cell in the xy-plane is $S_{\text{cell}} = 8.8 \cdot 10^{-14}$ m^2. Furthermore, maximum boundary layer resolution of the finest mesh is approximately 106 cells.

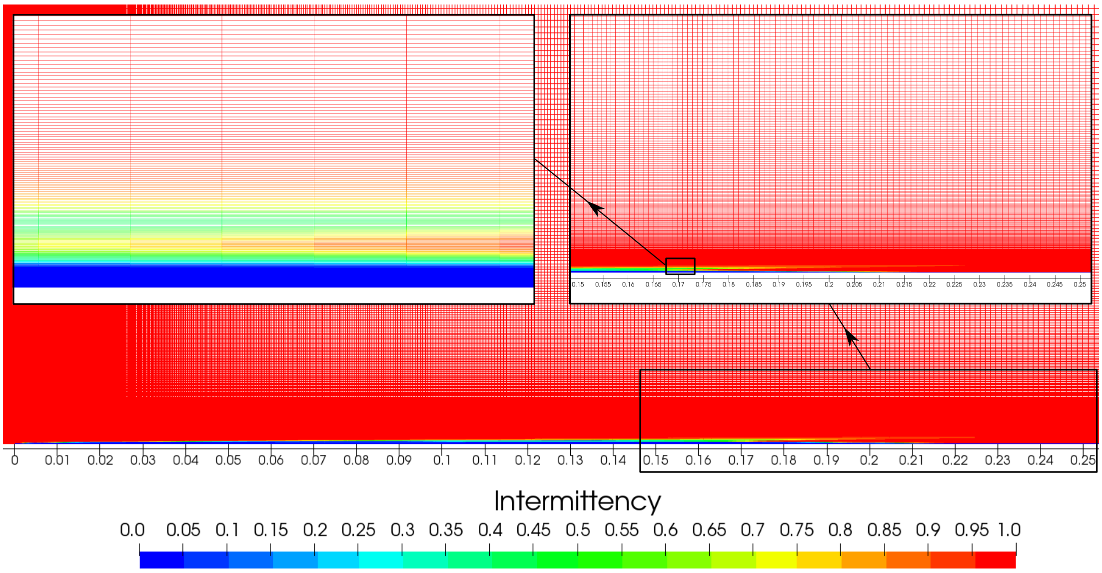

Figure 5.5: Flat Plate T3AM - Intermittency flow field.

Convergence of the Residuals

Convergence of the residuals of both turbulence models for Mesh 6 (Table 4.5) and low-turbulence T3AM case can be observed in Figure 5.6 and Figure 5.7. The residuals of the k-ω SST model for Mesh 6 converge after a total of $14,000$ iterations, while those of the γ-Re_θ model converge after a total of $20,000$ iterations (Figure 5.6 and Figure 5.7). For the finest mesh, the residuals of the k-ω SST model converge after a total of $55,000$ iterations, while those of the γ-Re_θ model converge after a total of $79,000$ iterations.

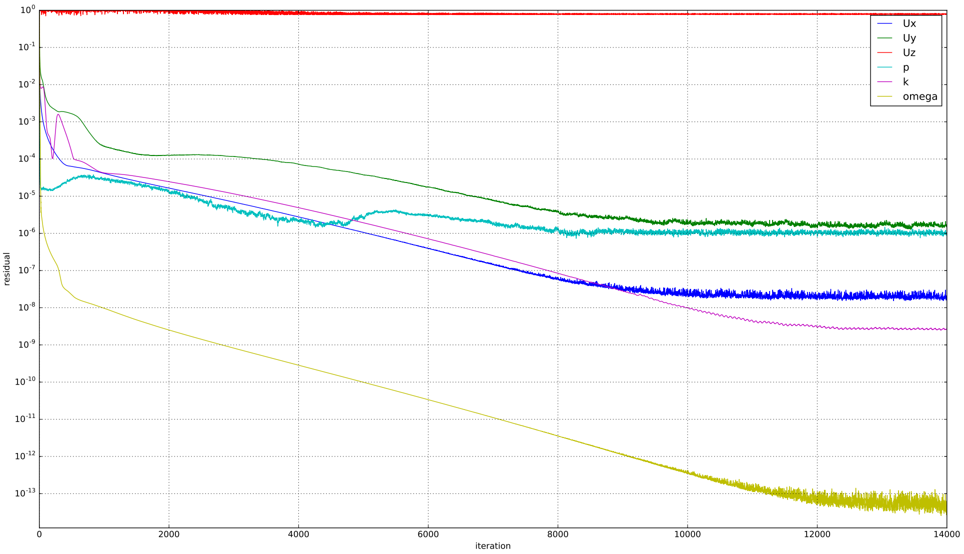

Figure 5.6: Flat Plate T3AM - Convergence of the residuals of the k-ω SST model for Mesh 6.

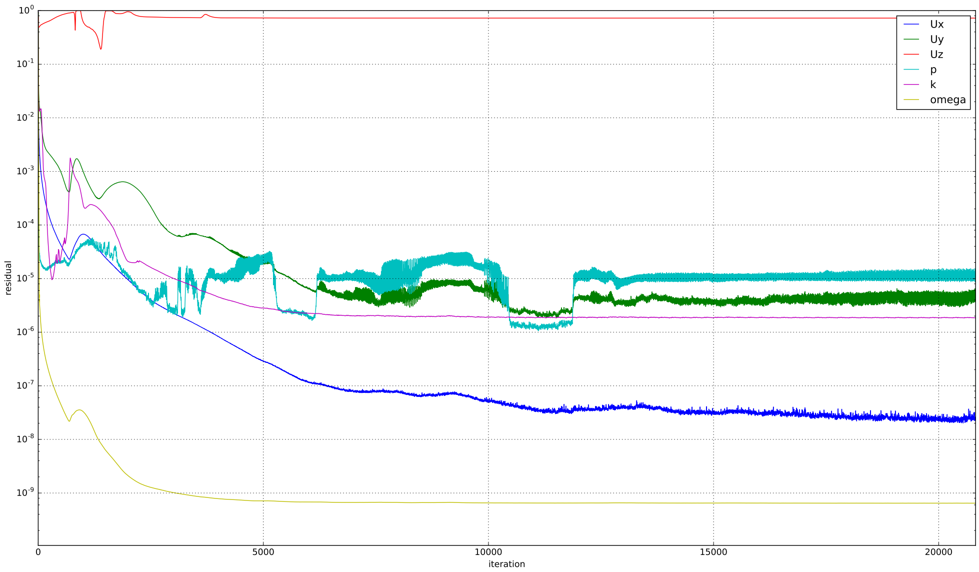

Figure 5.7: Flat Plate T3AM - Convergence of the residuals of the γ-Re_θ model for Mesh 6.

While it may seem that both turbulence models converge approximately after the same number of iterations, the values of γ and Re_θ continue to change, resulting in in the greater total number of iterations for the γ-Re_θ model. Furthermore, simulations with the k-ω SST model exhibited higher degree of stability than those with the γ-Re_θ model. Moreover, the k-ω SST model converged in a significantly shorter amount of time in comparison to the γ-Re_θ model.

5.3.2 High-Turbulence T3A Case

In order to check if the high turbulence affects the accuracy of the γ-Re_θ model a second flat plate case was selected for comparison. The value of the turbulence intensity Tu (Eq. 2.54) for the high-turbulence T3A case is $Tu = 5.36609\%$. In this subsection the experimental data is compared with the skin friction coefficient C_f (Eq. 5.8) and mean horizontal velocity U_x/U_∞ results. Furthermore, the intermittency field γ is presented in order to depict the transition region. Lastly, the residual convergence history is presented.

Skin Friction Coefficient

By comparing the skin friction coefficient results of both turbulence models with the experimental data it is clear that the transitional turbulence model γ - Re_θ produces significantly accurate results.

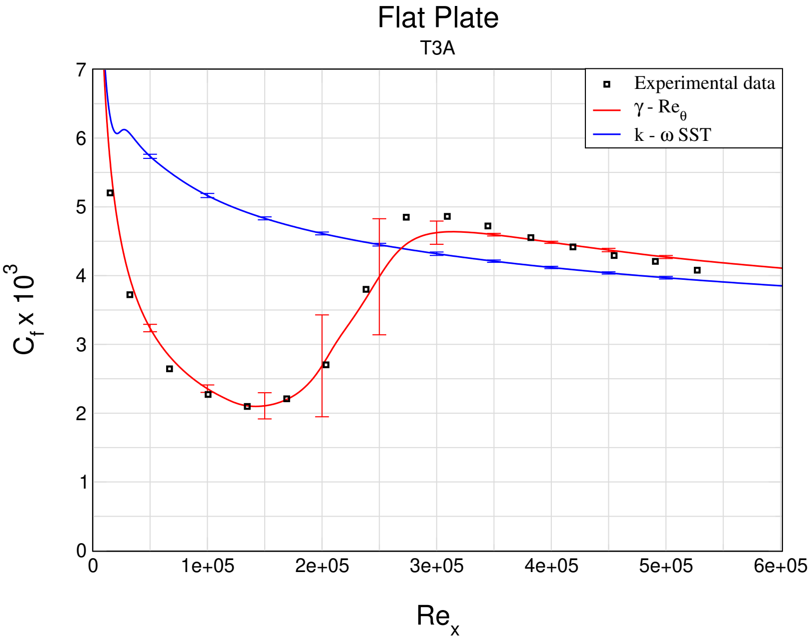

Figure 5.8: Flat plate T3A - Comparison of the skin friction coefficient C_f.

According to Figure 5.8 simulation results of the γ - Re_θ model show high degree of correspondence with the experimental data in the laminar region. Furthermore, γ - Re_θ model accurately predicts the transition onset and results also show high degree of correspondence with the experimental data early in the transition region. However, late in the transition region and early in the turbulent region the results show lower degree of correspondence, but still significantly higher than those of the k - ω SST model. Once again high numerical uncertainty can be observed in the transition region. Lastly, it can be observed that both turbulence models show a converging trend towards the same value of C_f in the fully turbulent region.

Mean Horizontal Velocity

Three locations along the Flat Plate geometry were selected to present mean horizontal velocity profiles. The locations are at the coordinates $x/L = 0.01006$, $x/L = 0.02035$ and $x/L = 0.05273$.

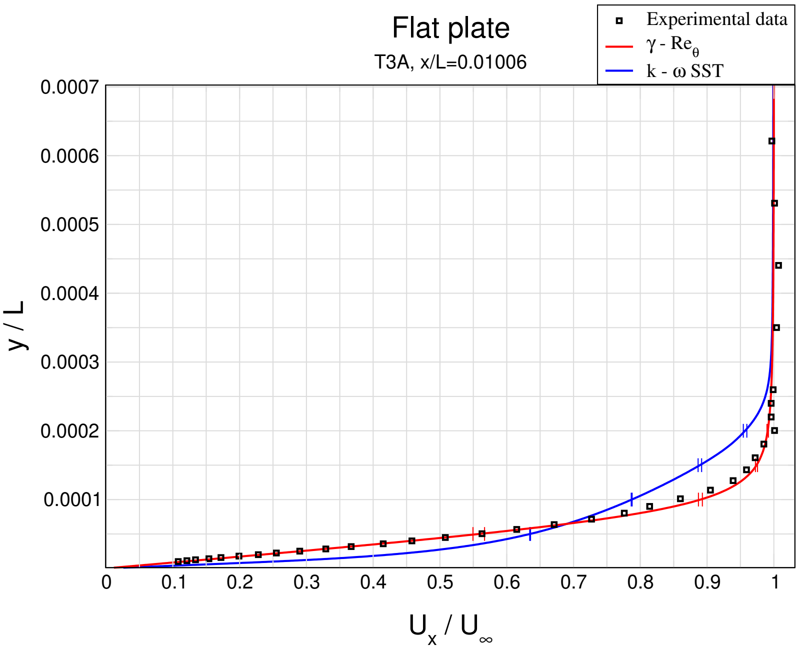

Figure 5.9: Flat Plate T3A - Mean horizontal velocity profile at the location $x/L = 0.01006$.

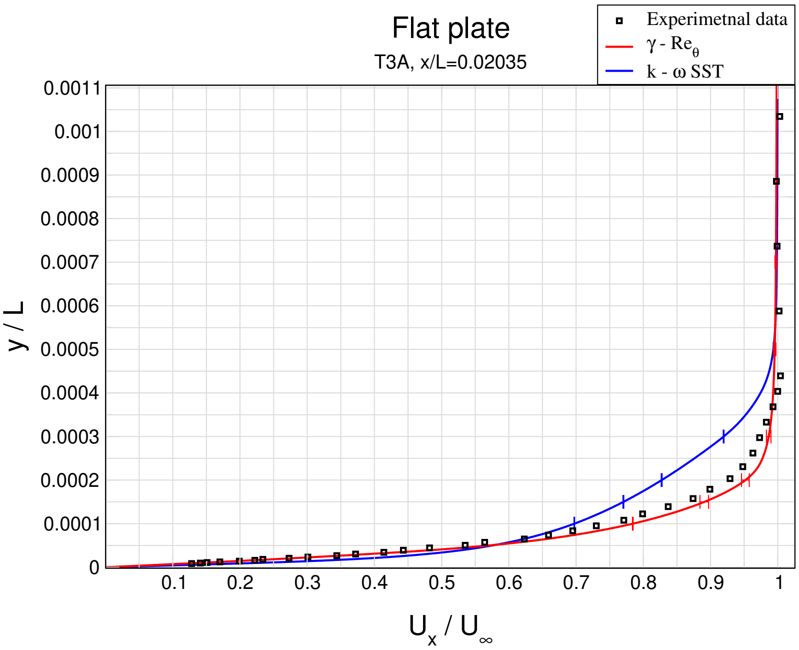

Figure 5.10: Flat Plate T3A - Mean horizontal velocity profile at the location $x/L = 0.02035$.

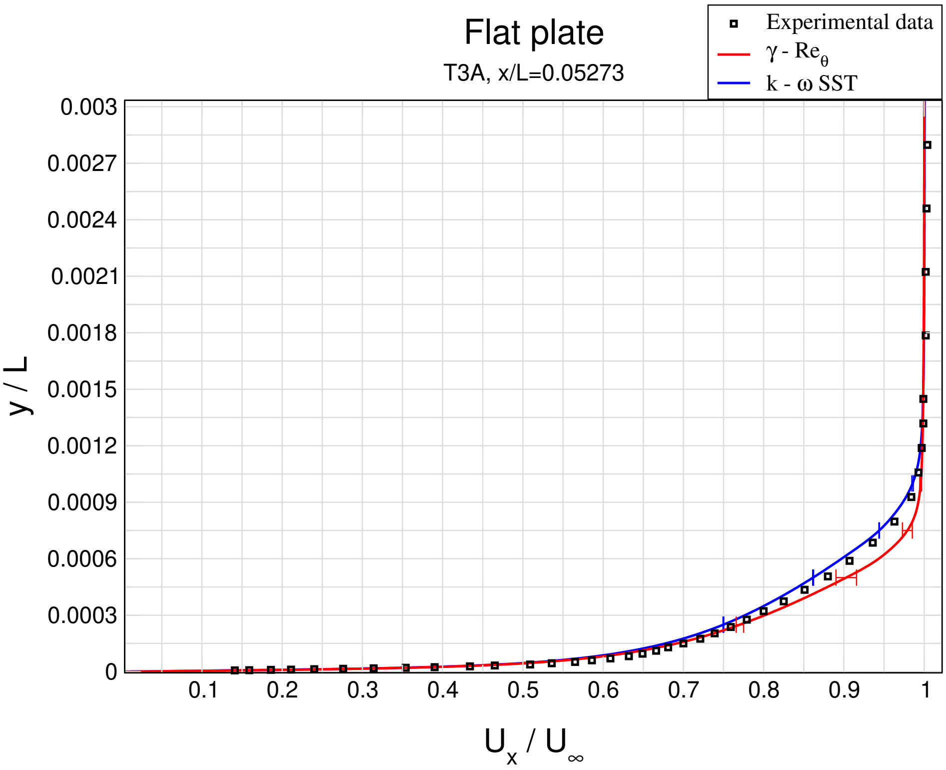

Figure 5.11: Flat Plate T3A - Mean horizontal velocity profile at the location $x/L = 0.05273$.

By comparing horizontal velocity profiles of both turbulence models it can be seen that the transitional turbulence model γ - Re_θ produces more accurate results at 2 out of 3 locations. If Figure 5.8 is compared with Figure 5.9 - Figure 5.11 it can be seen that Figure 5.9 represents mean horizontal velocity profile at the point located in the laminar region, Figure 5.10 at the point located in the transition region and Figure 5.11 at the point located in the fully turbulent region. Mean horizontal velocity profile of the γ - Re_θ model in the laminar region (Figure 5.9) show good agreement with the experimental data. Furthermore, the one in the transition region (Figure 5.10) even though less accurate, still shows high degree of correspondence with the experimental data. On the other hand, mean horizontal velocity profiles of the k - ω SST turbulence model show unsatisfying levels of accuracy at those 2 locations. However, at the location in the turbulent region (Figure 5.11) results of the k - ω SST model show slightly higher degree of correspondence with the experimental data than those of the γ - Re_θ model. This is possibly due to the fact that k - ω SST is a fully turbulent turbulence model and with the use of appropriate wall functions it warrants high enough accuracy in the fully turbulent region of the boundary layer. Finally, for the k - ω SST model it can be noticed that all 3 mean horizontal velocity profiles of the high-turbulence T3A case showed higher degree of correspondence with the experimental data than those of the low-turbulence T3AM case.

Intermittency Field

Intermittency field is presented in Figure 5.12, which consists of 3 segments. The main segment of the figure represents the γ flow field from the leading edge of the Flat Plate to the location where transition ends and the flow becomes fully turbulent. The First detail represents the transition region, while the second represents early section of the transition region.

For the finest mesh (Figure 5.12), maximum value of the y^+ of the cell by the wall is $y^+ = 0.452$. The area of the same cell in the xy-plane is $S_{\text{cell}} = 8.8 \cdot 10^{-14}$ m^2. Furthermore, maximum boundary layer resolution of the finest mesh is approximately 109 cells.

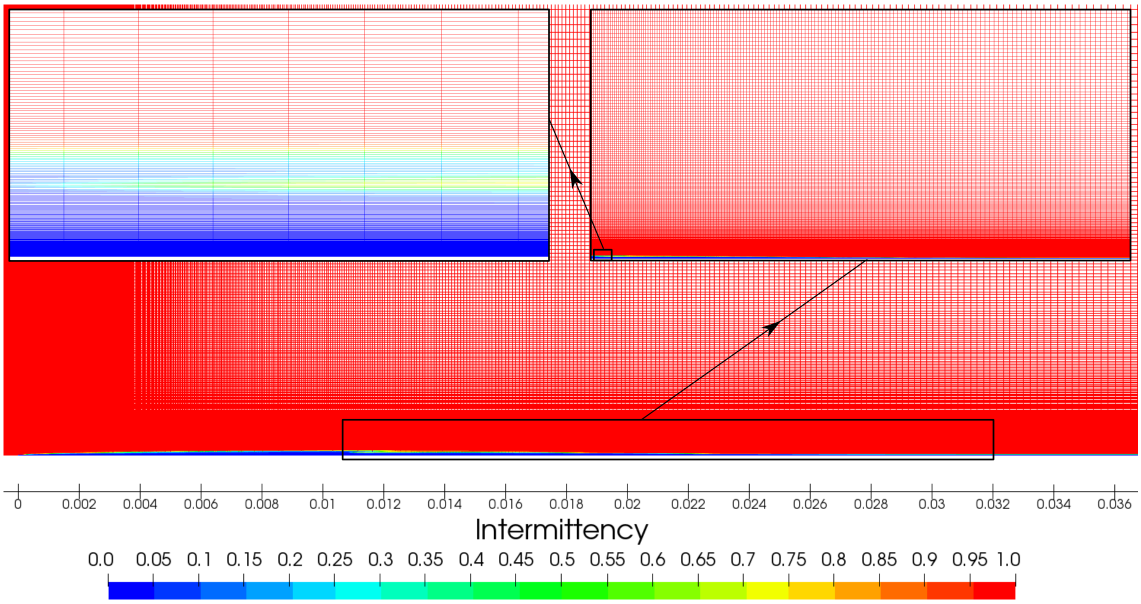

Figure 5.12: Flat Plate T3A - Intermittency flow field.

Convergence of the Residuals

Convergence of the residuals of both turbulence models for Mesh 6 (Table 4.5) and high-turbulence T3A case can be observed in Figure 5.13 and Figure 5.14. The residuals of the k-ω SST model for Mesh 6 converge after a total of $13,800$ iterations, while those of the γ-Re_θ model converge after a total of $20,000$ iterations (Figure 5.13 and Figure 5.14). For the finest mesh, the residuals of the k-ω SST model converge after a total of $60,000$ iterations, while those of the γ-Re_θ model converge after a total of $75,800$ iterations.

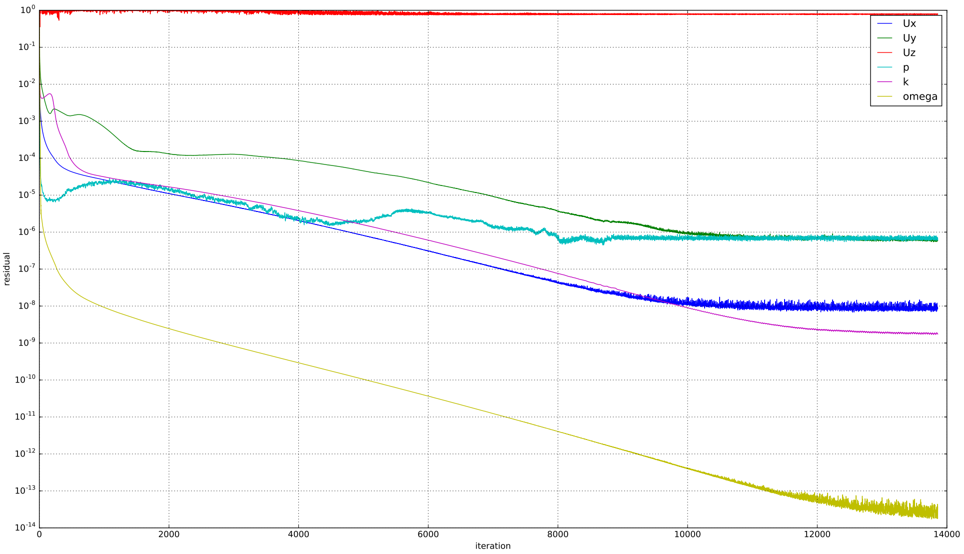

Figure 5.13: Flat Plate T3A - Convergence of the residuals of the k-ω SST model for Mesh 6.

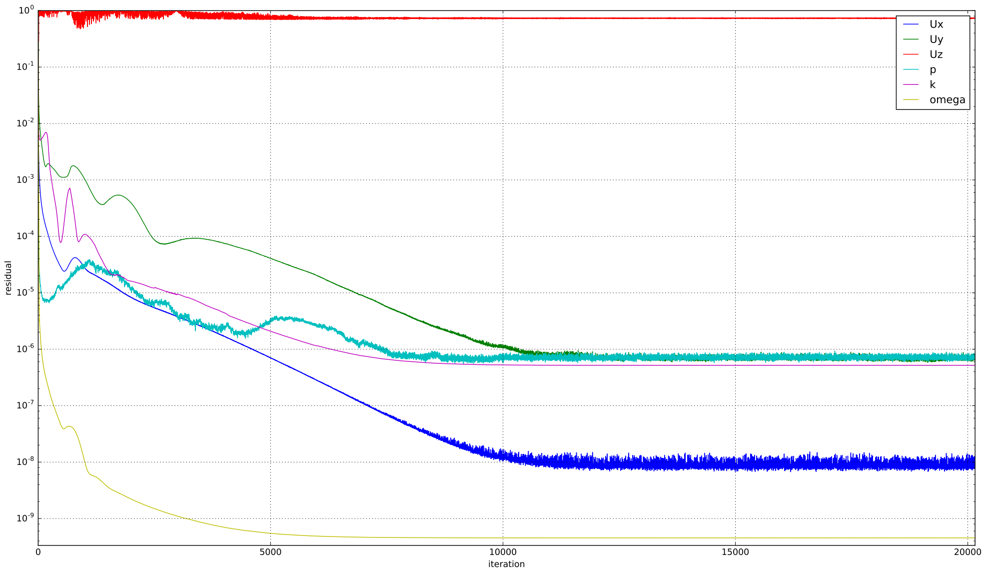

Figure 5.14: Flat Plate T3A - Convergence of the residuals of the γ-Re_θ model for Mesh 6.

While it may seem that both turbulence models converge approximately after the same number of iterations, the values of γ and Re_θ continue to change, resulting in in the greater total number of iterations for the γ-Re_θ model. Furthermore, simulations with the k-ω SST model exhibited higher degree of stability than those with the γ-Re_θ model. Moreover, the k-ω SST model converged in a significantly shorter amount of time in comparison to the γ-Re_θ model.

5.4 2D Eppler 387

In this section, results of the numerical simulations performed on the 2D Eppler 387 geometry and corresponding computational domains (Figure 4.4) are presented. Two computational domains were constructed for this case, one for the Eppler 387 geometry at the angle of attack of $\alpha = 1^\circ$ and the other for the geometry at the angle of attack of $\alpha = 7^\circ$. Experimental data was obtained by McGhee et al. [30].

5.4.1 Eppler 387 at the Angle of Attack of $\alpha = 1^\circ$

In this subsection experimental data is compared with the results of the pressure coefficient C_p, the lift coefficient C_L and the drag coefficient C_D. The coefficients are calculated as follows:

$$C_p = \frac{p - p_{\mathrm{max,inlet}}}{\frac{1}{2}\rho U_\infty^2} , \tag{5.9}$$

$$C_L = \frac{F_L}{\frac{1}{2}\rho U_\infty^2 A_{\mathrm{airfoil}}} , \tag{5.10}$$

$$C_{Dp} = \frac{F_{Dp}}{\frac{1}{2}\rho U_\infty^2 A_{\mathrm{airfoil}}} , \tag{5.11}$$

$$C_{D\mathrm{f}} = \frac{\tau_w}{\frac{1}{2}\rho U_\infty^2} , \tag{5.12}$$

$$C_D = C_{Dp} + C_{D\mathrm{f}} , \tag{5.13}$$

where p is the pressure, $p_{\mathrm{max,inlet}}$ is the maximum value of pressure at the inlet, ρ is the fluid density, U_∞ is the free-stream velocity, C_{Dp} is the pressure drag coefficient, F_{Dp} is the pressure drag force, $C_{D\mathrm{f}}$ is the friction drag force and τ_w is the wall shear stress.

Moreover, flow fields of the pressure coefficient C_p and mean velocity U fields are presented to further compare the γ - Re_θ and k - ω SST turbulence models . Furthermore, the intermittency field γ is presented in order to depict the transition region. Lastly, the residual convergence history is presented.

Pressure Coefficient

For Figure 5.15 x^* represents x axis of the computational domain aligned with the chord c of the airfoil geometry. By comparing the pressure coefficient results of both turbulence models with the experimental data it can be seen that the transitional turbulence model γ - Re_θ produces more accurate results and captures the transition with reasonable accuracy.

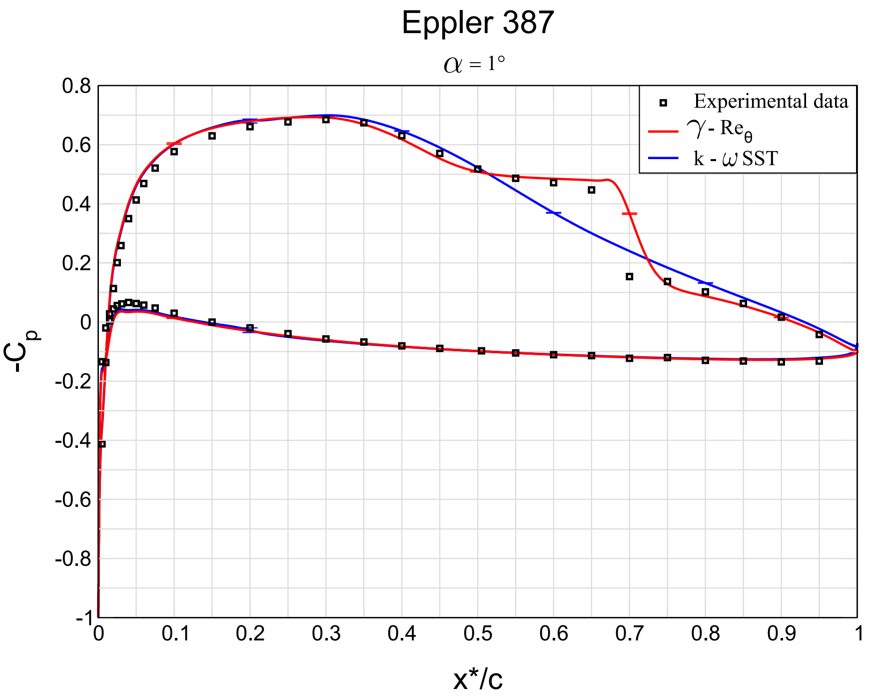

Figure 5.15: Eppler 387 at the angle $\alpha = 1^\circ$ - Pressure coefficient comparison.

On the suction side of the airfoil, simulation results of the γ - Re_θ model mostly show high degree of correspondence with the experimental data. It can be noticed that the accuracy drops in the transition region, $0.5 < x^*/c \leq 0.7$, but it is still at the satisfying level and higher than that of the k - ω SST model. Simulation results for the k - ω SST model mostly show high degree of correspondence with the experimental data, except in the transition region, $0.5 < x^*/c \leq 0.7$ where the accuracy drops significantly due to the inability of the k - ω SST model to simulate the effects of separated flows by using standard wall functions. This can partly be remedied with the use of Low-Re configuration of the k - ω SST model. Even though this configuration allows k - ω SST to simulate the effects of separated flows, it was previously observed by Menter et al. [7] that the separation point occurs downstream relative to the experimental data. On the pressure side of the airfoil both turbulence models show satisfying results and high degree of correspondence with the experimental data.

Pressure coefficient fields of both turbulence models are presented in Figure 5.16 and Figure 5.17, which consist of 3 segments. Main segment of both figures represents the pressure coefficient distribution over the entirety of the airfoil, while 2 details represent the pressure coefficient distribution at the leading edge. Once again it can be noticed, when comparing results of both turbulence models, that the C_p distribution at the leading edge is similar for both cases. On the other hand, the C_p distribution in the transition region, towards the trailing edge, differs significantly (Figure 5.16 and Figure 5.17).

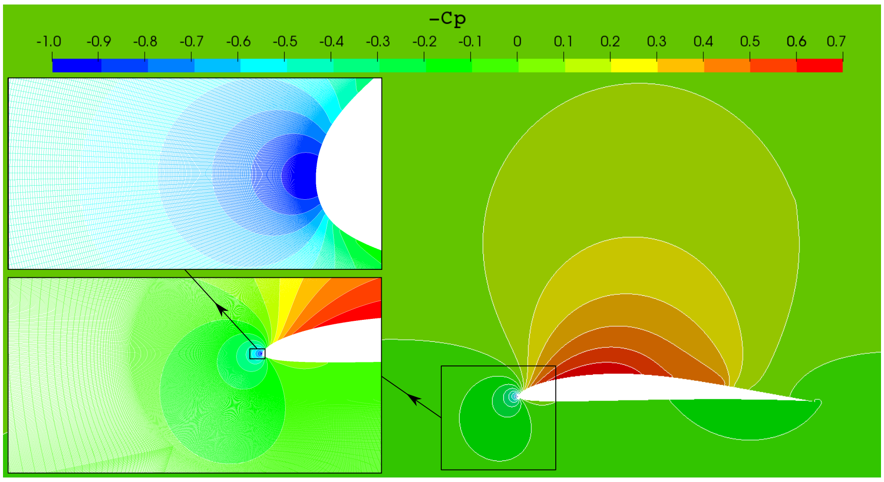

Figure 5.16: Eppler 387 at the angle $\alpha = 1^\circ$ - Pressure coefficient field for γ - Re_θ.

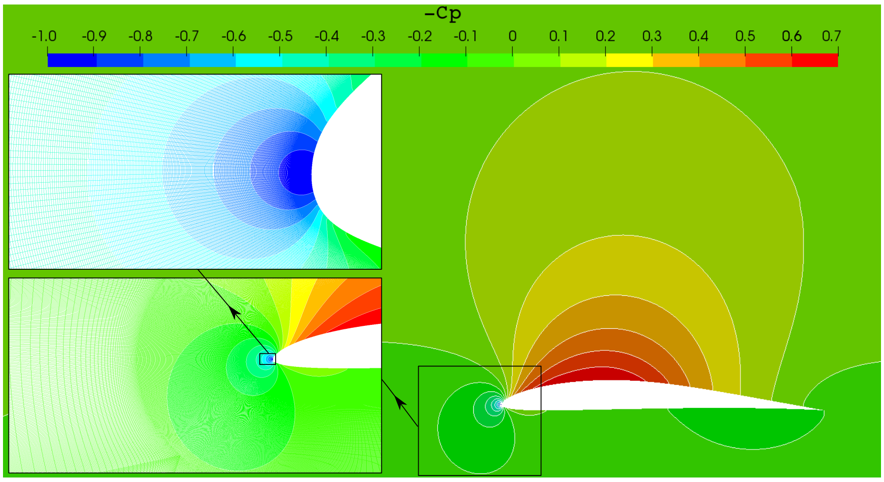

Figure 5.17: Eppler 387 at the angle $\alpha = 1^\circ$ - Pressure coefficient field for k - ω SST.

Lift and Drag Coefficients

Comparison of the lift and drag coefficient results with the experimental data is presented in Table 5.1 for both turbulence models. It is shown that the k-ω SST model produces slightly more accurate results for the lift coefficient than the γ-Re_θ model. However, the k-ω SST model greatly overestimates the drag coefficient value. Overall, the γ-Re_θ model produced results with a satisfying degree of accuracy.

	C_L	C_D	C_{Dp}	C_{Df}
Experimental data	0.465	$9.3 \cdot 10^{-3}$	–	–
k-ω SST	0.475	$13.223 \cdot 10^{-3}$	$2.475 \cdot 10^{-3}$	$10.748 \cdot 10^{-3}$
γ-Re_θ	0.487	$9.576 \cdot 10^{-3}$	$4.421 \cdot 10^{-3}$	$5.155 \cdot 10^{-3}$

Table 5.1: Eppler 387 at the angle $\alpha = 1^\circ$ - Comparison of the lift and drag coefficients .

Mean Velocity Field

Mean velocity fields of both turbulence models are presented in Figure 5.18 and Figure 5.19, which consist of 3 segments. Main segments of both figures represent the velocity distribution over the entirety of the airfoil, while 2 details represent the velocity distribution over the section of the transition region. Once again, formation of the separation bubble can be observed for the case of the γ - Re_θ, while this doesn't happen for the case of the k - ω SST.

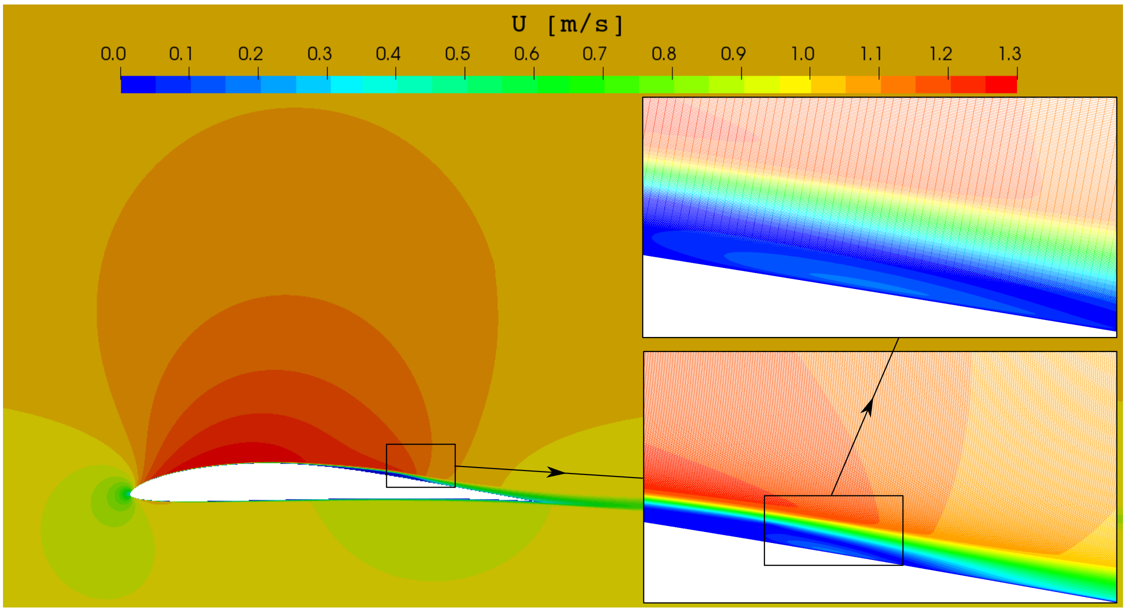

Figure 5.18: Eppler 387 at the $\alpha = 1°$ - Mean velocity field for γ - Re_θ

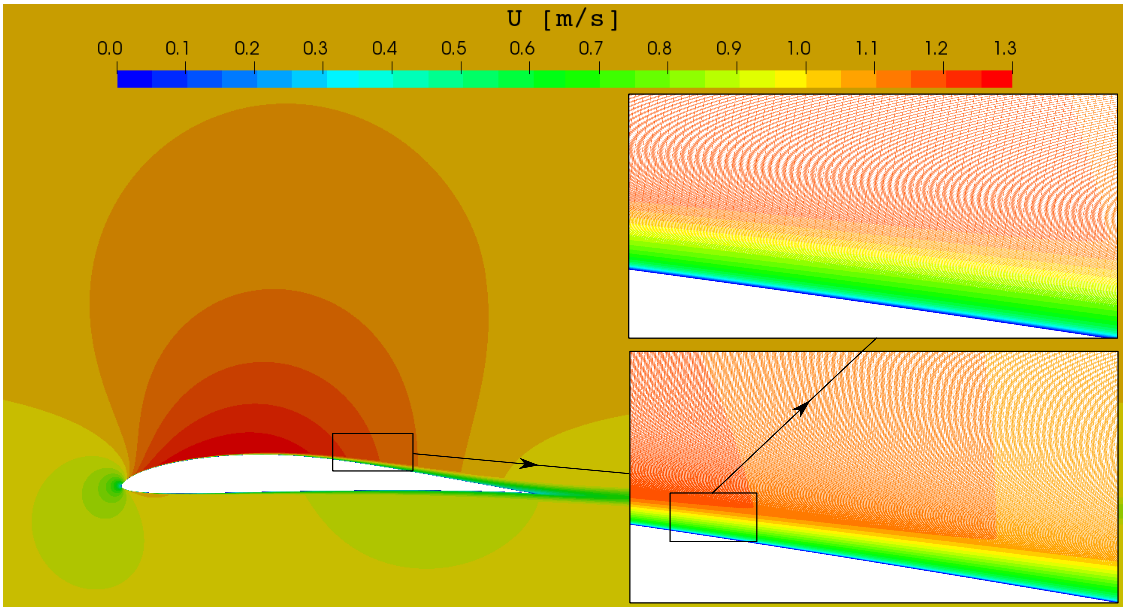

Figure 5.19: Eppler 387 at the angle $\alpha = 1°$ - Mean velocity field for k - ω SST

Intermittency Field

Intermittency field is presented in Figure 5.20, which consists of 3 segments. The main segment represents the intermittency distribution over the entirety of the airfoil, while 2 details represent the intermittency distribution over the section of the transition region. The position of details was chosen so that the effects of recirculation due to the flow separation, seen in Figure 5.18, could be observed in the intermittency distribution.

For the finest mesh (Figure 5.20), maximum value of the y^+ of the cell by the wall is approximately $y^+ = 0.27$. The area of the same cell in the xy-plane is $S_{\text{cell}} = 8.04 \cdot 10^{-10}$ m^2.

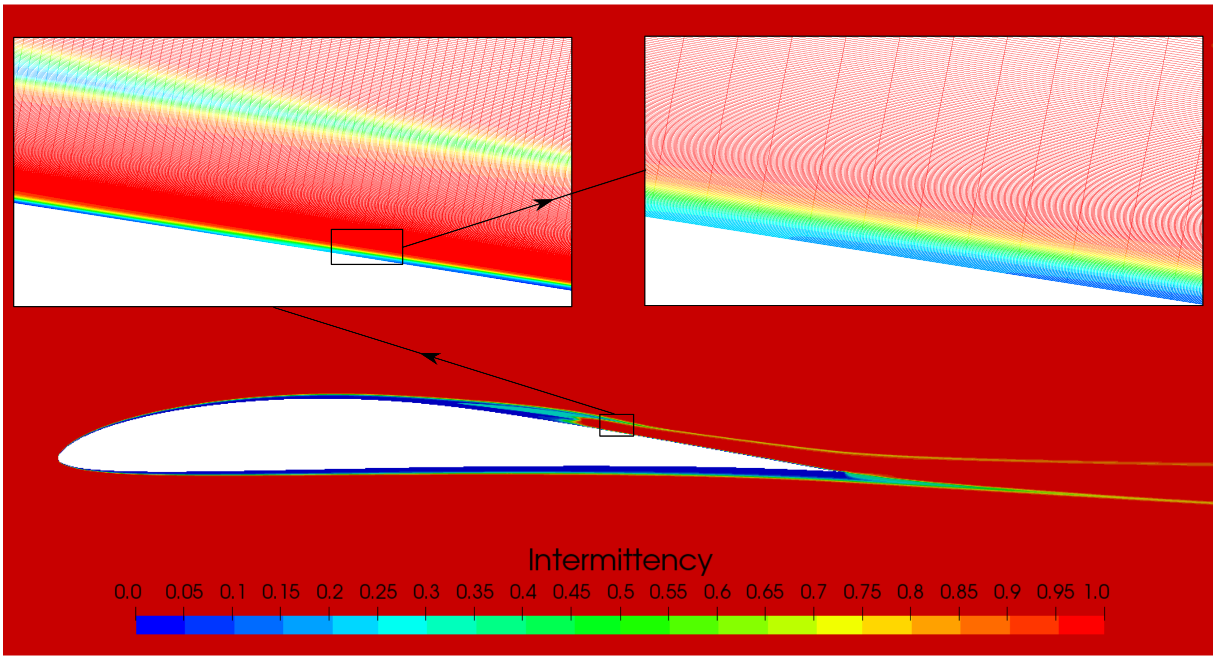

Figure 5.20: Eppler 387 at the angle $\alpha = 1°$ - Intermittency field.

Convergence of the Residuals

Convergence of the residuals of both turbulence models for Mesh 7 (Table 4.8) and airfoil at the attack angle of $\alpha = 1°$ can be observed in Figure 5.21 and Figure 5.22. The residuals of the k-ω SST model for Mesh 7 converge after a total of $4,000$ iterations, while those of the γ-Re_θ model converge after a total of $8,000$ iterations (Figure 5.21 and Figure 5.22). For the finest mesh, the residuals of the k-ω SST model converge after a total of $37,500$ iterations, while those of the γ-Re_θ model converge after a total of $44,800$ iterations.

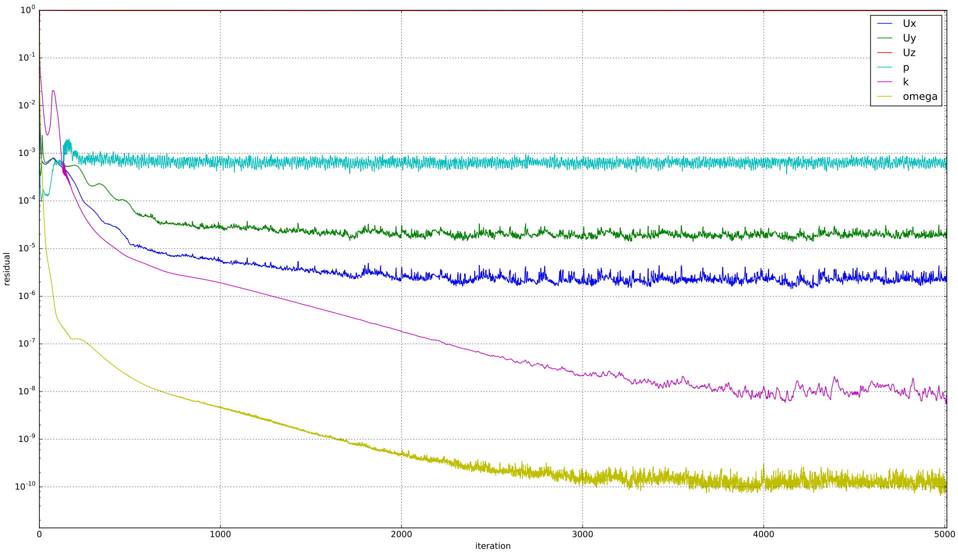

Figure 5.21: Eppler 387 at $\alpha = 1^{\circ}$ - Convergence of the residuals of the k-ω SST for Mesh 7.

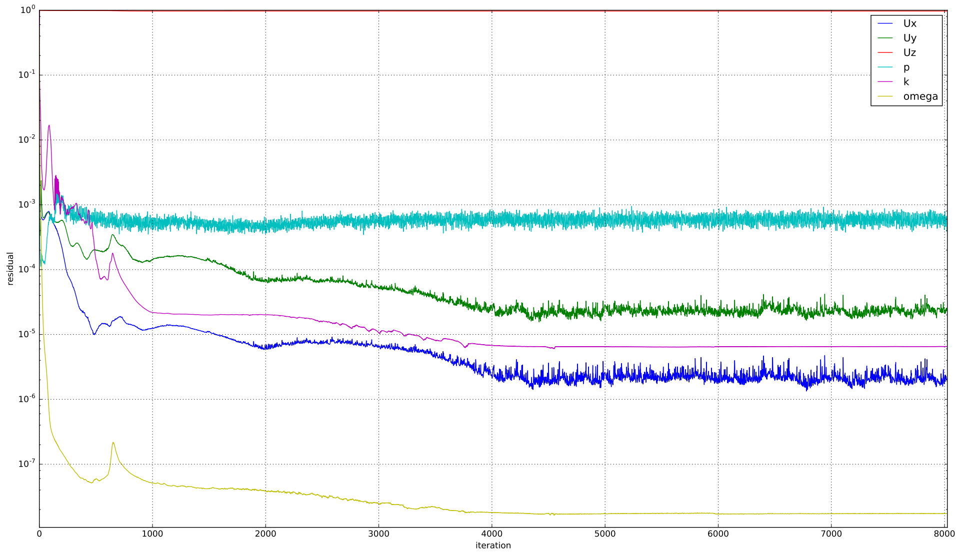

Figure 5.22: Eppler 387 at $\alpha = 1^{\circ}$ - Convergence of the residuals of the γ-Re_{θ} for Mesh 7.

While it may seem that both turbulence models converge approximately after the same number of iterations, the values of γ and Re_{θ} continue to change, resulting in in the greater total number of iterations for the γ-Re_{θ} model. Furthermore, simulations with the k-ω SST model exhibited higher degree of stability than those with the γ-Re_{θ} model. Moreover, the k-ω SST model converged in a significantly shorter amount of time in comparison to the γ-Re_{θ} model.

5.4.2 Eppler 387 at the Angle of Attack of $\alpha = 7°$

In this subsection experimental data is compared with the results of the pressure coefficient C_p (Eq. 5.9), the lift coefficient C_L (Eq. 5.13) and the drag coefficient C_D (Eq. 5.11). Moreover, fields of the pressure coefficient C_p and mean velocity U are presented to further compare the γ - Re_θ and k - ω SST turbulence models. Furthermore, the intermittency field γ is presented in order to depict the transition region. Lastly, the residual convergence history is presented.

Pressure Coefficient

For Figure 5.23 x^* represents the x axis of the computational domain aligned with the chord c of the airfoil geometry. By comparing pressure coefficient results of both turbulence models with the experimental data it can be seen that the turbulence model k - ω SST produces more accurate results, unlike the previous case. The laminar-to-turbulent transition predicted by the γ-Re_θ model does not actually occur in the experiment

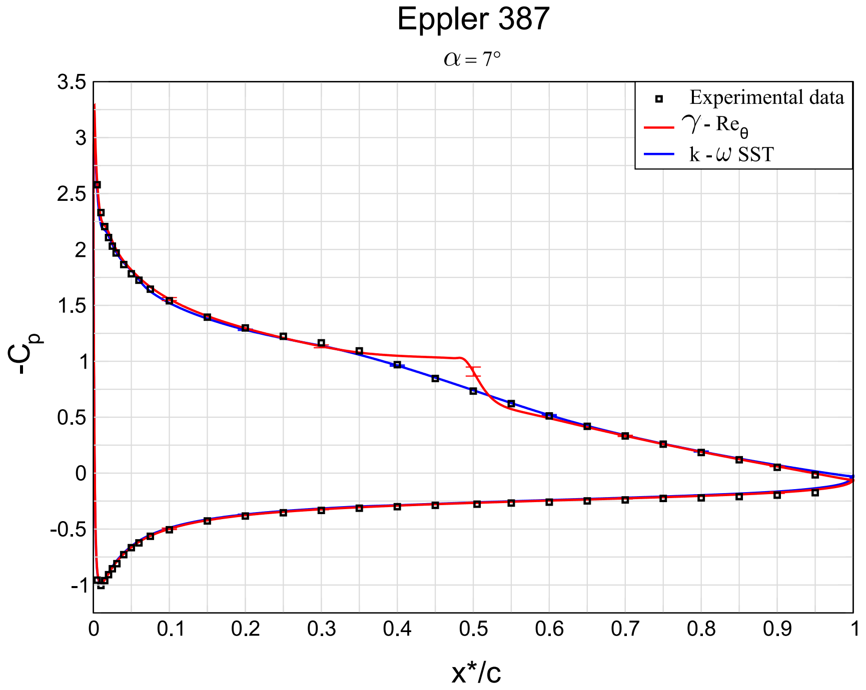

Figure 5.23: Eppler 387 at the angle $\alpha = 7°$ - Pressure coefficient comparison.

On the suction side of the airfoil simulation results for the γ - Re_θ model mostly show high degree of correspondence with the experimental data. It can be noticed that the accuracy drops in the transition region, $0.3 < x^*/c \leq 0.6$, where the drop in pressure is overestimated by the transitional turbulence model. According to McGhee et al. [30], for the case of flow around the Eppler 387 airfoil at the angle of attack of $\alpha = 7°$ and Reynolds number $Re = 300\ 000$

only natural transition occurs. It is unclear why the γ - Re_θ model predicts a separation bubble here, so further numerical simulations should be conducted to reach a conclusive answer. On the other hand, results of the k - ω SST model show good agreement with the experimental data. On the pressure side of the airfoil both turbulence models show satisfying results and high degree of correspondence with the experimental data.

Pressure coefficient fields of both turbulence models are presented in Figure 5.24 and Figure 5.25, which consist of 3 segments. Main segment of both figures represents pressure coefficient distribution over the entirety of the airfoil, while 2 details represent pressure coefficient distribution at the leading edge. When comparing the results of both turbulence models, that C_p distribution at the leading edge is similar for both cases. On the other hand, pressure distribution in the transition region, towards the trailing edge, differs between the turbulence models (5.24 - 5.25).

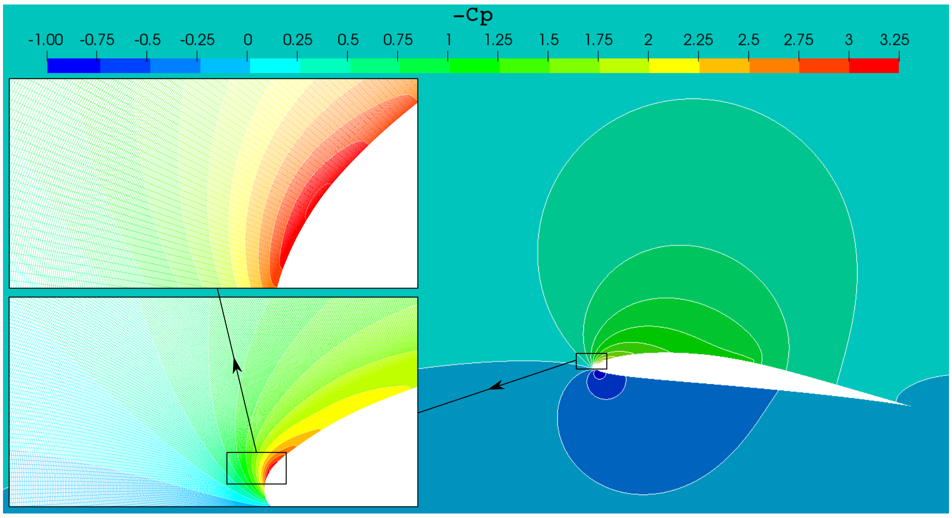

Figure 5.24: Eppler 387 at the angle $\alpha = 7°$ - Pressure coefficient field for γ - Re_θ.

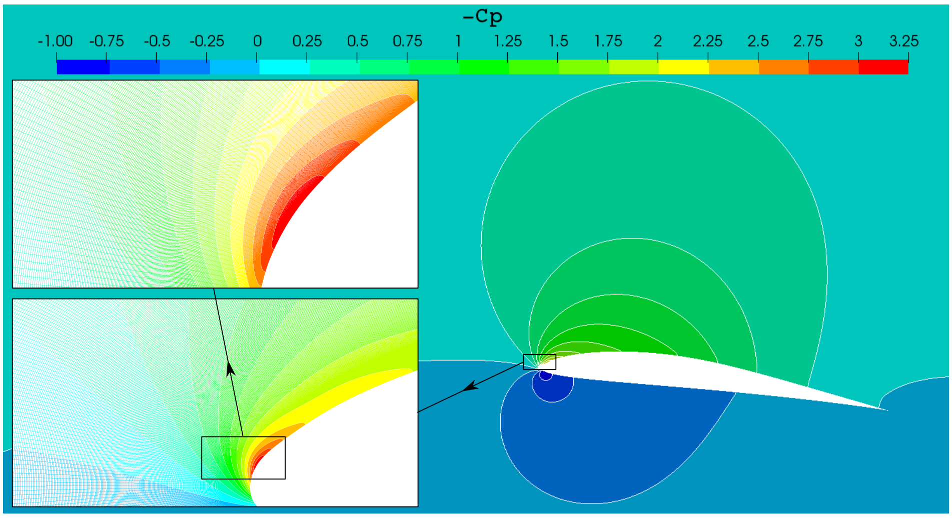

Figure 5.25: Eppler 387 at the angle $\alpha = 7°$ - Pressure coefficient field for k - ω SST.

Lift and Drag Coefficients

Comparison of the lift and drag coefficient results with the experimental data is presented in Table 5.2 for both turbulence models. It shown that the γ-Re_θ model produces slightly more accurate results for the lift coefficient than the k-ω SST model. Both turbulence models overestimate the drag coefficient value, however, the overestimation is significantly higher for the k-ω SST model. Overall, the γ-Re_θ model produced results with a more satisfying degree of accuracy.

	C_L	C_D	C_{Dp}	C_{Df}
Experimental data	1.106	$12.9 \cdot 10^{-3}$	–	–
k-ω SST	1.09	$18.396 \cdot 10^{-3}$	$9.316 \cdot 10^{-3}$	$9.08 \cdot 10^{-3}$
γ-Re_θ	1.117	$14.029 \cdot 10^{-3}$	$9.62 \cdot 10^{-3}$	$4.409 \cdot 10^{-3}$

Table 5.2: Eppler 387 at the angle $\alpha = 7°$ - Comparison of the lift and drag coefficients .

Mean Velocity Field

Mean velocity fields of both turbulence models are presented in Figure 5.26 and Figure 5.27, which consist of 3 segments. Main segments of both figures represent the velocity distribution over the entirety of the airfoil, while 2 details represent the velocity distribution over the section of the transition region. Once again, formation of the separation bubble can be observed for the case of γ - Re_θ, while this doesn't happen for the case of k - ω SST. However, as previously stated, the separation bubble shouldn't occur according to McGhee et al. [30].

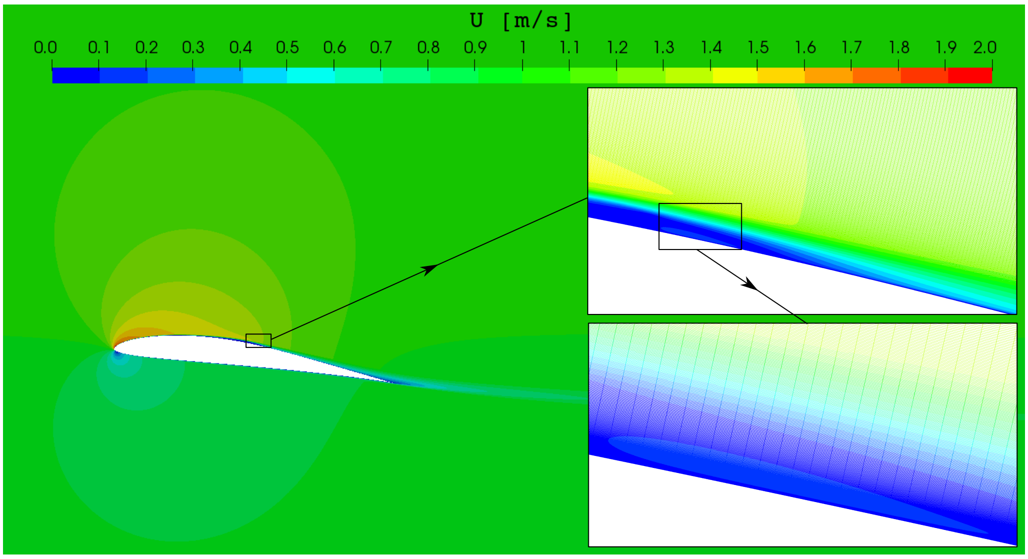

Figure 5.26: Eppler 387 at the angle $\alpha = 7°$ - Mean velocity field for γ - Re_θ

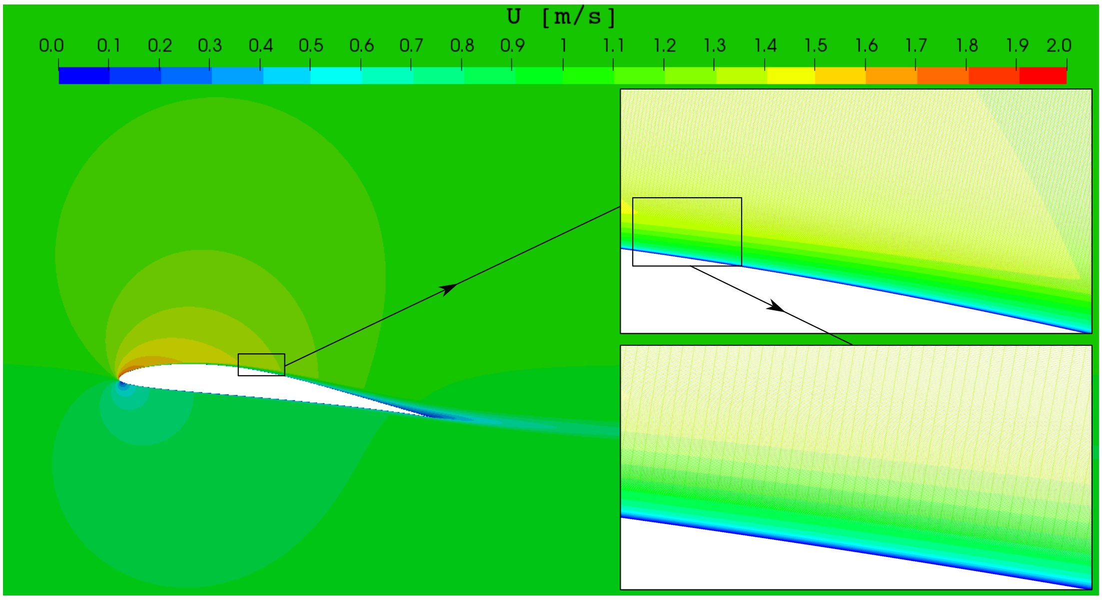

Figure 5.27: Eppler 387 at the angle $\alpha = 7^\circ$ - Mean velocity field for k - ω SST

Intermittency Field

Intermittency field is presented in Figure 5.28, which consists of 3 segments. The main segment represents the intermittency distribution over the entirety of the airfoil, while 2 details represent the intermittency distribution over the section of the transition region. The position of details was chosen so that flow separation, seen in Figure 5.28, could be observed in the intermittency distribution.

For the finest mesh (Figure 5.22), maximum value of the y^+ of the cell by the wall is approximately $y^+ = 0.431$. The area of the same cell in the xy-plane is $S_{\text{cell}} = 8.04 \cdot 10^{-10}$ m^2.

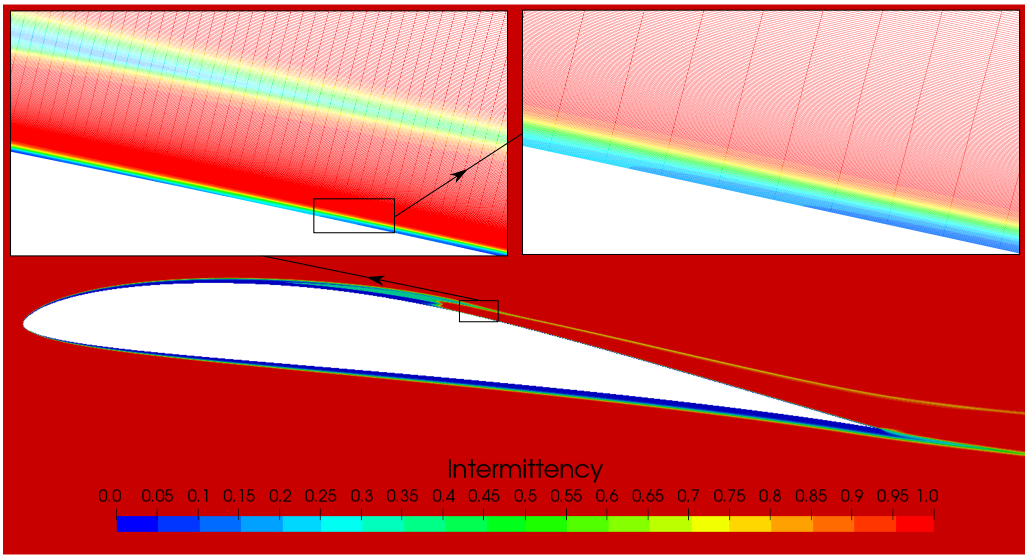

Figure 5.28: Eppler 387 at the $\alpha = 7^\circ$ - Intermittency field

Convergence of the Residuals

Convergence of the residuals of both turbulence models for Mesh 7 (Table 4.8) and airfoil at the attack angle of $\alpha = 7^\circ$ can be observed in Figure 5.29 and Figure 5.30. The residuals of the k-ω SST model for Mesh 7 converge after a total of $4,000$ iterations, while those of the γ-Re_θ model converge after a total of $8,000$ iterations (Figure 5.29 and Figure 5.30). For the finest mesh, the residuals of the k-ω SST model converge after a total of $40,800$ iterations, while those of the γ-Re_θ model converge after a total of $46,200$ iterations.

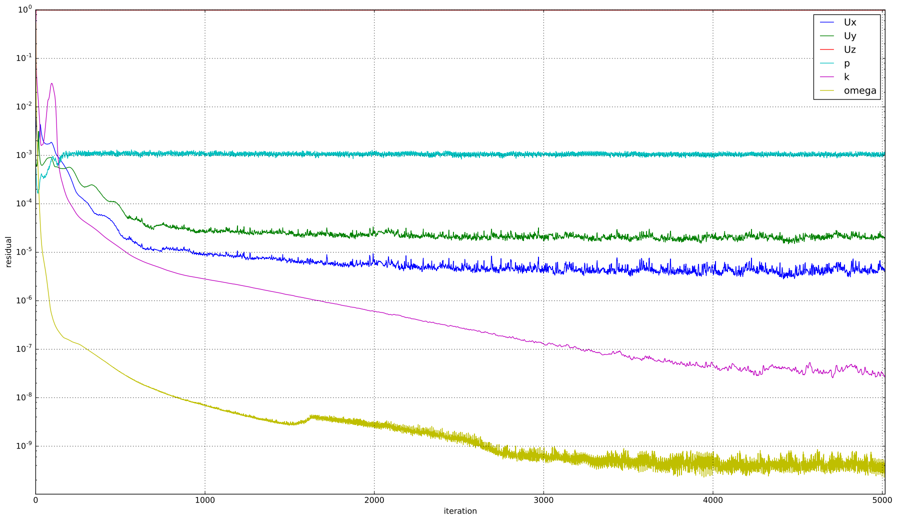

Figure 5.29: Eppler 387 at $\alpha = 7^\circ$ - Convergence of the residuals of the k-ω SST for Mesh 7.

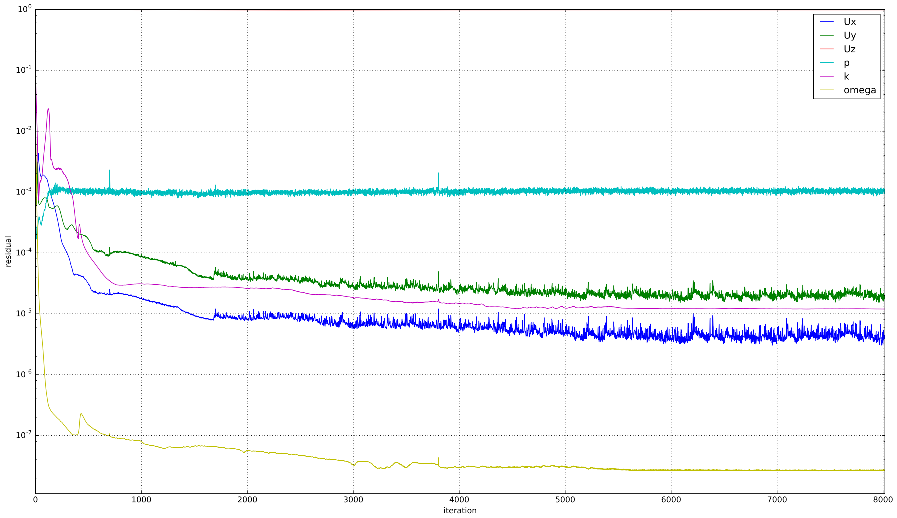

Figure 5.30: Eppler 387 at $\alpha = 7^\circ$ - Convergence of the residuals of the γ-Re_θ for Mesh 7.

While it may seem that both turbulence models converge approximately after the same number of iterations, the values of γ and Re_θ continue to change, resulting in in the greater total number of iterations for the γ-Re_θ model. Furthermore, simulations with the k-ω SST model exhibited higher degree of stability than those with the γ-Re_θ model. Moreover, the k-ω SST model converged in a significantly shorter amount of time in comparison to the γ-Re_θ model.

5.5 Closure

In this chapter results of numerical simulations were presented with the aim of validating the $\gamma - Re_\theta$ transitional turbulence model. Firstly, the results of 2D Flat Plate cases were presented. The results showed that $\gamma - Re_\theta$ exhibits higher degree of correspondence with the experimental data than the fully turbulent k - ω SST turbulence model. The results of 2D Eppler 387 cases were also presented. The results of Eppler 387 airfoil at the angle of attack of $\alpha = 1^\circ$ again showed that the $\gamma - Re_\theta$ exhibits higher degree of correspondence with the experimental data than the k - ω SST. However, the results of Eppler 387 airfoil at the angle of attack of $\alpha = 7^\circ$ showed that the k - ω SST exhibits higher degree of correspondence with the experimental data in terms of the pressure coefficient, as the $\gamma - Re_\theta$ predicted separation induced transition instead of the natural transition that occurs according to experimental data. In spite of this, lift and drag coefficient results of the $\gamma - Re_\theta$ model exhibited higher degree of correspondence with the experimental data than those of the k-ω SST model.

Following chapter serves as a conclusion of the thesis, offering an overview and discussion of completed tasks and resulting discoveries.

6 | Conclusion

The aim of this thesis was to validate the transitional γ-Re_θ turbulence model on flows containing laminar-to-turbulent transition in the non-equilibrium boundary layer. Firstly, an introduction was given describing the types of fluid flow with regard to turbulence and effects of different transition processes. Secondly, a mathematical model was presented, describing the governing equations of fluid flow and turbulence models used in the thesis. Turbulence models used in the thesis were the fully turbulent k-ω SST model and the transitional γ-Re_θ model. Thirdly, a numerical model was presented describing the Finite Volume Method, boundary conditions and implicitly coupled pressure-velocity systems. Finally, before the presentation of simulation results, short overview of used geometries, computational domains, meshes and applied boundary conditions was given.

Numerical simulations were performed in **foam-extend 4.1** environment using the implicitly coupled pressure-velocity solver **pUCoupledFoam**. The results were obtained for two validation cases, a 2D Flat Plate case and a 2D Eppler 387 airfoil case. Two sets of boundary conditions were applied on the Flat Plate case, a low-turbulence T3AM set and a high-turbulence T3A set. Overall, simulation results of both Flat Plate cases showed that γ-Re_θ exhibits higher degree of correspondence with the experimental data than k-ω SST. However, it is important to notice that the numerical uncertainty of the γ-Re_θ results, while mostly low along the Flat Plate, greatly increases in the transition region.

For the Eppler 387 case two computational domains were constructed, one for the airfoil at the angle of attack of $\alpha = 1^\circ$ and the other for the airfoil at the angle of attack of $\alpha = 7^\circ$. Simulation results of Eppler 387 case at the angle $\alpha = 1^\circ$ and γ-Re_θ turbulence model showed greater agreement with the experimental data than those of k-ω SST turbulence model. Transitional model γ-Re_θ correctly predicted separation induced transition and overall showed high degree of correspondence with the experimental data. However, simulation results of Eppler 387 case at the angle $\alpha = 7^\circ$ and k-ω SST turbulence model showed greater agreement with the experimental data than those of γ-Re_θ turbulence model. In this case γ-Re_θ incorrectly predicts separation induced transition whereas, natural transition occurs according to the experimental data. While γ-Re_θ generally exhibited good agreement with the experimental data, incorrect prediction of separation induced transition lead to an overestimated pressure drop in the transition region. It is unclear why this occurs and further research should be conducted to conclude if this is a one off case or there is a general error in the empirical correlations of the γ-Re_θ model. In spite of this, lift and drag coefficient results of the γ-Re_θ model exhibited higher degree of correspondence with the experimental data than those of the k-ω SST model.

To further conclude, the transitional turbulence model γ-Re_θ overall showed better agreement with the experimental data than the fully turbulent turbulence model k - ω SST. However, further research should be conducted to conclude if incorrectly predicted separation induced transition is a one off case or a general error in the empirical correlations of the γ-Re_θ model. Furthermore, it is expected that the industrial implementation of transitional turbulence models in the near future will still be hampered by high resolution mesh requirements and long execution times, however, it is hoped that with further advancements in technology this will become less of an issue.

Appendices

A Discretisation Settings

Appendix A serves as an overview of the discretisation settings used in this Thesis.

A.1 Flat Plate

A.1.1 γ-Re_θ Transitional Turbulence model

```
ddtSchemes
{
    default   steadyState ;
}

gradSchemes
{
    default    cellLimited   leastSquares   1;
}

divSchemes
{
    default                          none;
    div(phi,U)                       Gauss linearUpwind grad(U);
    div(phi,k)                       Gauss vanLeerDC;
    div(phi,omega)                   Gauss vanLeerDC;
    div(phi,ReThetat)                Gauss vanLeerDC;
    div(phi,gammaInt)                Gauss vanLeerDC;
    div((nuEff*dev(T(grad(U)))))     Gauss  linear ;

    div(U)                           Gauss  linear ;
}

laplacianSchemes
{
    default                               Gauss  linear   corrected ;
     laplacian (DkEff,k)                  Gauss  linear   limited   0.5;
     laplacian (DomegaEff,omega)          Gauss  linear   limited   0.5;
     laplacian (DReThetatEff,ReThetat)    Gauss  linear   limited   0.5;
     laplacian (DgammaIntEff,gammaInt)  Gauss linear  limited   0.5;
}

 interpolationSchemes
```

```
{
    default           linear ;
}

snGradSchemes
{
    default           corrected ;
}
```

A.1.2 k-ω SST Turbulence model

```
ddtSchemes
{
    default   steadyState ;
}

gradSchemes
{
    default    cellLimited   leastSquares   1;
}

divSchemes
{
    default                             none;
    div(phi,U)                          Gauss linearUpwind grad(U);
    div(phi,k)                          Gauss upwind;
    div(phi,omega)                      Gauss upwind;
    div((nuEff*dev(T(grad(U)))))        Gauss  linear ;

    div(U)                              Gauss  linear ;
}

laplacianSchemes
{
    default                           Gauss  linear   corrected ;
     laplacian (DkEff,k)              Gauss  linear   limited   0.5;
     laplacian (DomegaEff,omega)  Gauss linear   limited   0.5;
}

 interpolationSchemes
{
    default           linear ;
}
```

```
snGradSchemes
{
    default          corrected ;
}
```

A.2 Eppler 387

A.2.1 γ-Re_θ Transitional Turbulence model

```
ddtSchemes
{
    default   steadyState ;
}

gradSchemes
{
    default    cellLimited   leastSquares   1;
}

divSchemes
{
    default                          none;
    div(phi,U)                       Gauss linearUpwind grad(U);
    div(phi,k)                       Gauss vanLeerDC;
    div(phi,omega)                   Gauss vanLeerDC;
    div(phi,ReThetat)                Gauss vanLeerDC;
    div(phi,gammaInt)                Gauss vanLeer01DC;
    div((nuEff*dev(T(grad(U)))))     Gauss  linear ;

    div(U)                           Gauss  linear ;
}

laplacianSchemes
{
    default                              Gauss  linear   corrected ;
     laplacian (DkEff,k)                 Gauss  linear   limited   0.5;
     laplacian (DomegaEff,omega)         Gauss  linear   limited   0.5;
     laplacian (DReThetatEff,ReThetat)   Gauss  linear   limited   0.5;
     laplacian (DgammaIntEff,gammaInt)  Gauss linear   limited   0.5;
}
```

```
interpolationSchemes
{
    default             linear ;
}

snGradSchemes
{
    default             corrected ;
}
```

A.2.2 k-ω SST Turbulence model

```
ddtSchemes
{
    default   steadyState ;
}

gradSchemes
{
    default    cellLimited   leastSquares   1;
}

divSchemes
{
    default                          none;
    div(phi,U)                       Gauss linearUpwind grad(U);
    div(phi,k)                       Gauss upwind;
    div(phi,omega)                   Gauss upwind;
    div((nuEff*dev(T(grad(U)))))     Gauss  linear ;

    div(U)                           Gauss  linear ;
}

laplacianSchemes
{
    default                          Gauss  linear   corrected ;
     laplacian (DkEff,k)             Gauss  linear   limited   0.5;
     laplacian (DomegaEff,omega)  Gauss linear   limited   0.5;
}

interpolationSchemes
{
    default             linear ;
```

```
}

snGradSchemes
{
    default             corrected ;
}
```

B | Solver Settings

Appendix B gives an overview of the solver settings used in this Thesis.

B.1 Flat Plate

```
solvers
{
    Up
    {
        solver           AMG;
        cycle            V−cycle;
        coarseningType   SAMG;
        norm             componentNorm;
        normComponent    3;
        nPreSweeps       1;
        nPostSweeps      3;
        groupSize        4;
        minCoarseEqns    50;
        nMaxLevels       100;
        scale            on;
        smoother         ILUC0;

        minIter          0;
        maxIter          10;
        tolerance        1e−7;
        relTol           0.0;
    }
    k
    {
        solver            BiCGStab;
        preconditioner    DILU;
        tolerance         1e−12;
        relTol            0;
        minIter           1;
    }
    omega
    {
        solver            BiCGStab;
        preconditioner    DILU;
        tolerance         1e−12;
```

```
        relTol          0;
        minIter         1;
    }
    ReThetat
    {
        solver          BiCGStab;
        preconditioner  DILU;
        tolerance       1e−12;
        relTol          0;
        minIter         1;
    }
    gammaInt
    {
        solver          BiCGStab;
        preconditioner  DILU;
        tolerance       1e−12;
        relTol          0;
        minIter         1;
    }
}

blockSolver
{
    convergence         1e−8;
    pRefPoint           (−4 −0.6 −0);
    pRefValue           0;
}

fieldBounds
{
    U       300;
    p       −1e7 1e7; //  Do not  limit  p
}

pUCoupledFoam
{
    nNonOrthogonalCorrectors 1;
}

 relaxationFactors
{
    equations
    {
        U               0.8;
        ReThetat        0.9;
```

```
        gammaInt        0.9;
        k               0.9;
        omega           0.9;
    }
    fields
    {
    }
}
```

B.2 Eppler 387

```
solvers
{
    Up
    {
        solver          AMG;
        cycle           V−cycle;
        coarseningType  SAMG;
        norm            componentNorm;
        normComponent   3;
        nPreSweeps      1;
        nPostSweeps     3;
        groupSize       4;
        minCoarseEqns   50;
        nMaxLevels      100;
        scale           on;
        smoother        ILUC0;

        minIter         0;
        maxIter         10;
        tolerance       1e−7;
        relTol          0.0;
    }
    k
    {
        solver           BiCGStab;
        preconditioner   DILU;
        tolerance        1e−12;
        relTol           0;
        minIter          1;
    }
    omega
    {
```

```
        solver           BiCGStab;
        preconditioner   DILU;
        tolerance        1e−12;
        relTol           0;
        minIter          1;
    }
    ReThetat
    {
        solver           BiCGStab;
        preconditioner   DILU;
        tolerance        1e−12;
        relTol           0;
        minIter          1;
    }
    gammaInt
    {
        solver           BiCGStab;
        preconditioner   DILU;
        tolerance        1e−12;
        relTol           0;
        minIter          1;
    }
}

blockSolver
{
    convergence        1e−8;
    pRefPoint          (−4 −0.6 −0);
    pRefValue          0;
}

fieldBounds
{
    U       300;
    p       −1e7 1e7; // Do not limit p
}

pUCoupledFoam
{
    nNonOrthogonalCorrectors 1;
}

 relaxationFactors
{
    equations
```

```
    {
        U               0.8;
        ReThetat        0.9;
        gammaInt        0.9;
        k               0.8;
        omega           0.8;
    }
    fields
    {
    }
}
```

Bibliography

[1] O. Reynolds, "An experimental investigation of the circumstances which determine whether the motion of water shall be direct or sinuous, and of the law of resistance in parallel channels," *Philosophical Transactions of the Royal Society of London*, vol. 174, 1996.

[2] R. Langtry, *A correlation-based transition model using local variables for unstructured parallelized CFD codes*. PhD thesis, University of Stuttgart, 2006.

[3] L. Balatinec, "An overview of rotor-stator interfaces for computational fluid dynamics simulations in turbomachinery," Master's thesis, University of Zagreb, 2019.

[4] R. B. Langtry and F. R. Menter, "Correlation-based transition modeling for unstructured parallelized computational fluid dynamics codes," *AIAA Journal*, vol. 47, no. 12, pp. 2894–2906, 2009.

[5] T. Uroić, *Implicitly Coupled Finite Volume Algorithms*. PhD thesis, University of Zagreb, 2019.

[6] CFDOnline, "Two equation turbulence models." `https://www.cfd-online.com/Wiki/Two_equation_turbulence_models`. Accessed on: 21.01.2020.

[7] F. R. Menter, M. Kuntz, and R. B. Langtry, "Ten years of industrial experience with the sst turbulence model," *Heat and Mass Transfer*, vol. 4, 01 2003.

[8] F. R. Menter, R. Langtry, and S. Völker, "Transition modelling for general purpose cfd codes," *Flow, Turbulence and Combustion*, vol. 77, pp. 277–303, Nov 2006.

[9] F. R. Menter, *Zonal Two Equation k-w Turbulence Models For Aerodynamic Flows*. The American Institute of Aeronautics and Astronautics, 1993.

[10] L. Eça and M. Hoekstra, "procedure for the estimation of the numerical uncertainty of cfd calculations based on grid refinement studies," *Journal of Computational Physics*, vol. 262, pp. 104 – 130, 2014.

[11] O. Ltd, "Openfoam the open source cfd toolbox." `https://www.openfoam.com/`.

[12] H. G. Weller, G. Tabor, H. Jasak, and C. Fureby, "A tensorial approach to computational continuum mechanics using object-oriented techniques," *Computers in Physics*, vol. 12, no. 6, pp. 620–631, 1998.

[13] H. Jasak, "The openfoam extend project (community-driven releases of openfoam)." `https://foam-extend.fsb.hr/`.

[14] H. Jasak, A. Jemcov, and Z. Tukovic, "Openfoam: A c++ library for complex physics simulations," 11 2013.

[15] H. K. Versteeg and W. Malalasekera, *An Introduction to Computational Fluid Dynamics*. Pearson Education Limited, 2007.

[16] T. Uroić, H. Jasak, and H. Rusche, *Implicitly Coupled Pressure–Velocity Solver: Selected Papers of the 11th Workshop*, pp. 249–267. 01 2019.

[17] N. AVT-313, "Incompressible laminar-to-turbulent flow transition study comparison workshop." `http://web.tecnico.ulisboa.pt/ist12278/Workshop_AVT_313_October_2019/Workshop_AVT313_October_2019.htm`.

[18] S. B. Pope, *Turbulent Flows*. Cambridge University Press, 2000.

[19] H. Jasak, "Course materials for practical finite volume method," 2019.

[20] W. Jones and B. Launder, "The prediction of laminarization with a two-equation model of turbulence," *International Journal of Heat and Mass Transfer*, vol. 15, no. 2, pp. 301 – 314, 1972.

[21] D. C. Wilcox, *Turbulence modelling for CFD*. DCW Industries Incorporated, La Cañada, 1994.

[22] NASA, "Turbulence modeling resource." `https://turbmodels.larc.nasa.gov/sst.html`. Accessed on: 21.01.2020.

[23] A. Hellsten, *Some improvements in Menter's k-omega SST turbulence model*. The American Institute of Aeronautics and Astronautics, 1998.

[24] H. Jasak, *Error Analysis and Estimation for the Finite Volume Method with Applications to Fluid Flows*. PhD thesis, Imperial College.

[25] S. Patankar and D. Spalding, "A calculation procedure for heat, mass and momentum transfer in three-dimensional parabolic flows," *International Journal of Heat and Mass Transfer*, vol. 15, no. 10, pp. 1787 – 1806, 1972.

[26] Y. Saad, *Iterative methods for sparse linear systems*. SIAM, 2000.

[27] C. M. Rhie and W. L. Chow, "Numerical study of the turbulent flow past an airfoil with trailing edge separation," *AIAA Journal*, vol. 21, no. 11, pp. 1525–1532, 1983.

[28] I. D. Z. Virag, M. Šavar, *Mehanika Fluida II - Predavanja*. Sveučilište u Zagrebu, Fakultet strojarstva i brodogradnje, 2017.

[29] ERCOFTAC, "Classic collection database." `http://cfd.mace.manchester.ac.uk/ercoftac/index.html`. Accessed on: 21.01.2020.

[30] R. J. McGhee, B. S. Walker, and B. F. Millard, "Experimental results for the eppler 387 airfoil at low reynolds numbers in the langley low-turbulence pressure tunnel," in *NASA Technical Memorandum 4062*, 1988.